BULGARIAN CHEMICAL COMMUNICATIONS

BULGARIAN CHEMICAL COMMUNICATIONS

PREFACE

The Fourth International Scientific Conference "Alternative Energy Sources, Materials & Technologies AESMT'21" was held between 14th and 15th June 2021 in Ruse, Bulgaria. Representatives of 34 countries (Australia, Austria, Bulgaria, Chile, China, Cyprus, Egypt, France, Germany, Greece, Hungary, India, Iran, Iraq, Israel, Italy, Kazakhstan, Kosovo, Kuwait, Latvia, Lebanon, Lithuania, Macedonia, Nigeria, Norway, Portugal, Romania, Russia, Serbia, Spain, Tajikistan, Turkey, United Kingdom, Yemen) sent their works to the conference. Some of the reports (9 works) have been selected and are published after international peer-review in the present Special Issue of the journal "Bulgarian Chemical Communications".

It is our pleasure to be guest editors of the presented articles, which focus on new international scientific results in the field of Alternative Energy Sources, Materials and Technologies (Energy Materials Science, Storages with Phase Change Materials, Shallow Geothermal Energy Applications, Energy Efficiency, Solar Photovoltaic Systems, Low-Carbon Technologies, Mechanical Engineering and Technologies, and Electrical Engineering).

Prof. Aleksandar Georgiev, DSc (Institute of Chemical Engineering, Bulgarian Academy of Sciences, Sofia, Bulgaria)

Assoc. Prof. Daniela Dzhonova-Atanasova (Institute of Chemical Engineering, Bulgarian Academy of Sciences, Sofia, Bulgaria)

Guest editors of the present Special Issue

Dual-phase steels with low manganese content. Structures and mechanical properties

C. Dulucheanu[1], T.L. Severin[1, *], D.A. Cerlinca[1], L. Irimescu[1], J. Javorova[2]

[1]*Faculty of Mechanical Engineering, Mechatronics and Management & Research Center MANSiD, University "Stefan cel Mare" of Suceava, Romania*
[2]*University of Chemical Technology and Metallurgy, Bulevard Sveti Kliment Ohridski 8, 1756 Studentski Kompleks, Sofia, Bulgaria*

This article are presented the results of studies conducted to determine the influence of the intercritical heating temperature on the structure and mechanical properties of the dual-phase steels with low manganese content (0,511% Mn, respectively 0,529% Mn). The ferrite-martensitic structures, specific for dual-phase steels, were obtained by intercritical quenching, which consisted of heating the samples to temperatures located between critical points Ac_1 and Ac_3 (760, 780, 800, and 820 $^\circ$C), followed by cooling in water. With the help of metallographic analyses, the volume fraction of martensite and ferrite microhardness from the structures were determined, and by tensile testing, the ultimate tensile strength and the total elongation were established. The results obtained for the two dual-phase steels with low manganese content were compared with those determined in previous research, performed on a dual-phase steel with 1.90% Mn.

Keywords: dual-phase steel, intercritical quenching, ferrite-martensite structure, mechanical properties

INTRODUCTION

"Advanced High-Strength Steels" (AHSS) developed for the automotive industry uniquely satisfy safety, efficiency, emissions, manufacturability, durability, and cost requirements; these alloys are characterized by structures and metallurgical properties that allow automakers to meet the diverse functional requirements of today's vehicles. The AHSS family includes, in addition to Complex-Phase (CP), Ferritic-Bainitic (FB), Martensitic (MS), Transformation-Induced Plasticity (TRIP), Hot-Formed (HF), Twinning-Induced Plasticity (TWIP), and the dual-phase steels (DP), alloys extensively used to manufacture crumple zone to the body structure of a vehicle, closures, hood, doors, front and rear rails, beams and cross members, cowl inner and outer, crush cans, shock towers, fasteners, and wheel; it is estimated that in the coming years (until 2030), a percentage of 30 to 32% of the body of a car will be made of dual-phase steels. These materials, in general, a percentage of carbon less than 0.12 %, a content of manganese between 1.0 % and 3.5 %, and elements such as V, Cr, Mo, Si, Nb, Ti are to be found in chemical composition in proportions situated below 1%; in the last years, to reduce cars costs, there have been studied steels in which the content of manganese was less than 1 % (0.5 to 1 % Mn). One of the technologies applied to produce these steels is intercritical quenching, the structure resulting from the application of this technology being influenced by both the chemical composition of the steel and the technological parameters of the heat treatment, especially the heating (quenching) temperature. At the same time, the mechanical properties depend in a decisive way on the quantitative ratio and the morphology of the structural components that are formed as a result of the thermal processing process, [1-14]. Therefore, the influence of the heat treatment technological parameters on the structure and properties of a dual-phase steel must be established.

The dual-phase steels have been studied at the Faculty of Mechanical Engineering, Mechatronics and Management from University "Stefan cel Mare" of Suceava since 1992, and over the years researches has been conducted on several categories of alloys, [14, 15]; in recent years, research has been carried out on dual-phase steels with low content of manganese, [12, 13, 16, 17], in this article being presented results obtained for two such alloys.

EXPERIMENTAL DETAILS

The chemical compositions of the two studied alloys (denoted DPS-A and DPS-B) were determined with a FOUNDRY-MASTER Xpert Spectrophotometer (Oxford Instruments Analytical GmbH, Germany), they being (wt. %), [6, 10]:

- DPS-A: Fe, 0.087 C, 0.511 Mn, 0.091 Si, 0.0036 P, 0.0039 S, 0.029 Cr, 0.005 Mo, 0.049 Ni, 0.003 Al, 0.082 Cu, 0.003 V, 0.003 W;
- DPS-B: Fe, 0.101 C, 0.529 Mn, 0.091 Si,

* To whom all correspondence should be sent:
severin.traian@usm.ro

0.0032 P, 0.0037 S, 0.036 Cr, 0.005 Mo, 0.015 Ni, 0.003 Al, 0.015 Cu, 0.011 Pb, 0.003 V, 0.003 W.

The initial structures of these alloys were composed of 85.30% ferrite and 14.70% pearlite for DPS-A steel, respectively 83.90% ferrite and 16.10% pearlite for DPS-B steel, [13, 17].

In intercritical quenching applied to hypoeutectoid steels, knowing the critical points Ac_1 and Ac_3 is particularly important, the success of these heat treatments depending on the accuracy of this data. In the case of the studied alloys, the critical points in solid-state phase transformation (Ac_1 and Ac_3) required to establish heating temperatures at the intercritical quenching, were determined by dilatometric analyses performed with a DIL 402 Expedis-SUPREME Dilatometer (NETZSCH Gerätebau GmbH, Germany), the values obtained being: $Ac_1 = 724.00$ °C and $Ac_3 = 899.40$ °C for DPS-A steel, $Ac_1 = 725.10$ °C and $Ac_3 = 898.90$ °C for DPS-B steel, [13, 17-19].

In order to obtain ferrite-martensite structure characteristic to dual-phase steels, samples of the two alloys were subjected to intercritical quenching at which the heating temperatures (T_Q) had the following values, (established according to position of the critical points in the solid-state phase transformation): 760, 780, 800 and 820 °C. The heating was conducted in an electric laboratory furnace Nabertherm LT 40/11/P330 (Nabertherm GmbH, Germany), at constant values of the T_Q temperature, for 30 minutes. The cooling was performed in water with the temperature of 20 °C (without mechanical agitation), in an LBS 2 bath (Falc Instruments S.R.L., Italy), [13, 17].

After quenching, the samples were subjected to metallographic analyses in order to determine the volume fraction of martensite (V_M) in the structures, the morphology, and distribution of this phase; the analyses were performed with a LEXT OLS4100 Laser Microscope, (Olympus Corporation, Japan) and OLYMPUS Stream MOTION Image Analysis Software. The ferrite-martensite structures were highlighted by the following metallographic etchant: picric acid 4 % solution in alcohol (etching time - 60 seconds) and then nital 2% (etching time - 5 seconds); after the metallographic etchant, on micrographics, the martensite appeared as "dark" regions and the ferrite beads as the "white" regions, [20]. These analyses were completed by measuring the ferrite microhardness, determinations that were made with a MicroHardness Tester DuraScan 70 (Emco Prüfmaschinen-Test GmbH, Austria), the test load of the Vickers indenter being 0.098 N (0.01 kgf).

Five micrographs and five microhardness measurements were performed on each metallographic sample.

In order to determine the influence of heating temperatures (T_Q) from the intercritical quenching on mechanical properties, specimens with ferrite-martensite structures obtained by applying the heat treatments described above were subjected to tensile testing, which determined the ultimate tensile strength (R_m) and the total elongation (A_5). These tests have been carried out on a QUASAR 600 universal testing machine (Cesare GALDABINI SpA, Italy). Cylindrical specimens with a diameter of 5 mm and an initial length between markers (in the calibrated portion) of 25 mm were used (ten samples for each heating temperature).

RESULTS AND DISCUSSIONS

In a dual-phase steel, the mechanical characteristics are influenced by both the volume fraction of martensite, and the properties of the ferrite, [2-5]; therefore, in order to analyse the influence of the intercritical heating temperature on the mechanical properties of the DPS-A and DPS-B steels, on samples intercritical quenched, the volume fraction of martensite (V_M) and the ferrite microhardness (HV0.01), were determined, the results being presented in Tab.1, Figs. 1 and 2.

Raising the heating temperature (T_Q) has led to an increase in the volume fraction of martensite (V_M) in structures (Tab.1 and Fig.1), because raising the T_Q temperature in the intercritical range (Ac_1 - Ac_3) has determined an increase in the volume fraction of austenite, phase which, by quenching has turned into martensite; thus, in the DPS-A steel samples, the volume fraction of martensite (V_M) increased with 16.79 percent, from 20.19% ($T_Q = 760$ °C) to 36.98% ($T_Q = 820$ °C), whereas in the samples of DPS-B steel it increased with 16.03 percent, from 22.10% ($T_Q = 760$ °C) to 38.13% ($T_Q = 820$ °C).

In the structures obtained by quenching from $T_Q = 760$ °C (Fig.3) the martensite was in the form of small islands, situated mainly at the boundaries of the ferrite grains. Most of these martensite islands were located in regions where, in initial structure, has been perlite; by heating (over Ac_1) the pearlite was dissolved into austenite, which, through quenching was transformed into martensite. Through this mechanism has formed a volume fraction of martensite (V_M) of approx. 14.70% in the case of DPS-A steel, respectively 16.10% in the case of DPS-A steel, i.e. the equivalent of the volume fraction of pearlite from the original structures.

Table 1. Volume fraction of martensite and ferrite microhardness (average values)

T_Q, °C	760		780		800		820	
Steel	DPS-A	DPS-B	DPS-A	DPS-B	DPS-A	DPS-B	DPS-A	DPS-B
V_M, %	20.19	22.10	23.83	25.51	29.41	30.40	36.98	38.13
HV0.01	170.43	184.77	182.37	194.63	188.54	199.28	192.11	202.53
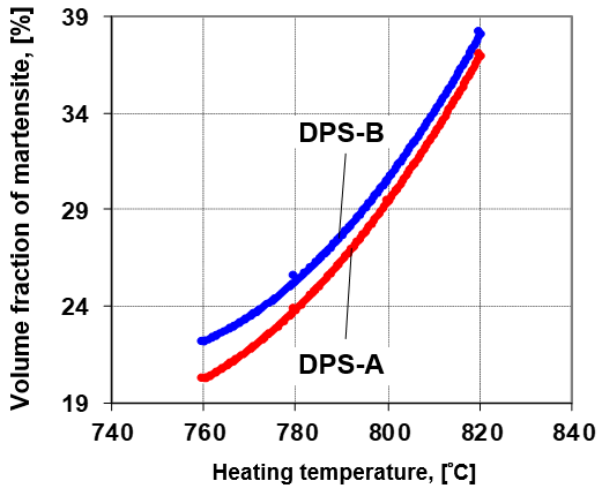
Fig.1. Influence of the heating temperature on the volume fraction of martensite.
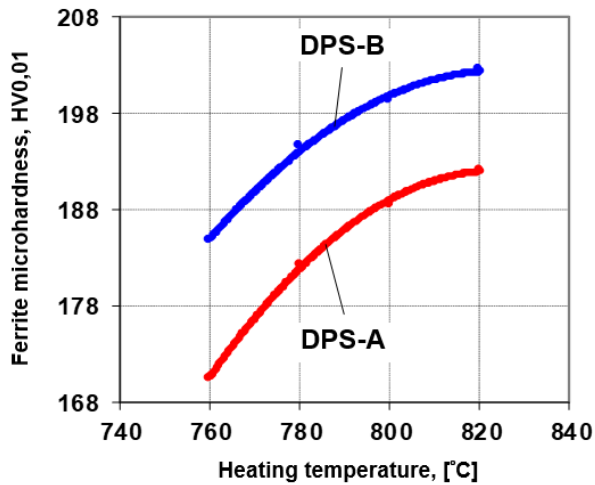
Fig.2. Influence of the heating temperature on the ferrite microhardness.

Other martensite islands (the difference up to 20.19% for DPS-A steel, respectively 22.10% for DPS-B steel, Tab.1) have been formed from the austenite obtained by the allotropic transformation of the ferrite. Raising the heating temperature (T_Q), from 760 °C at 780, 800 and 820 °C determined an increase in the volume fraction of austenite that was formed by the allotropic transformation of the ferrite, which generated an increasing volume fraction of martensite that resulted by quenching. In the same time with the rising of the volume fraction
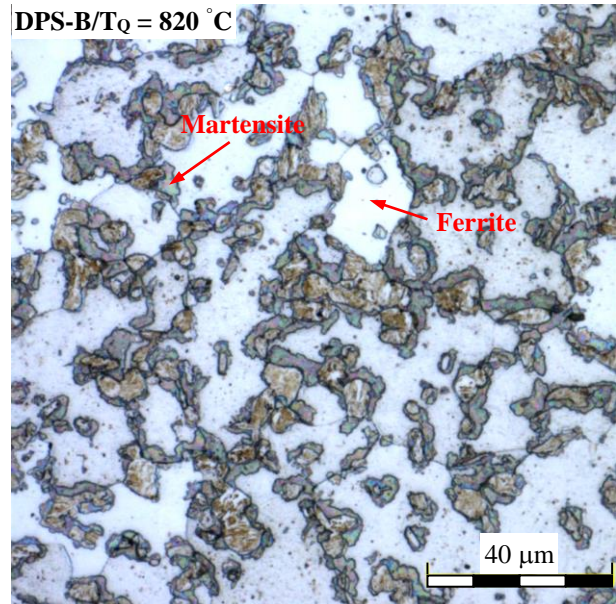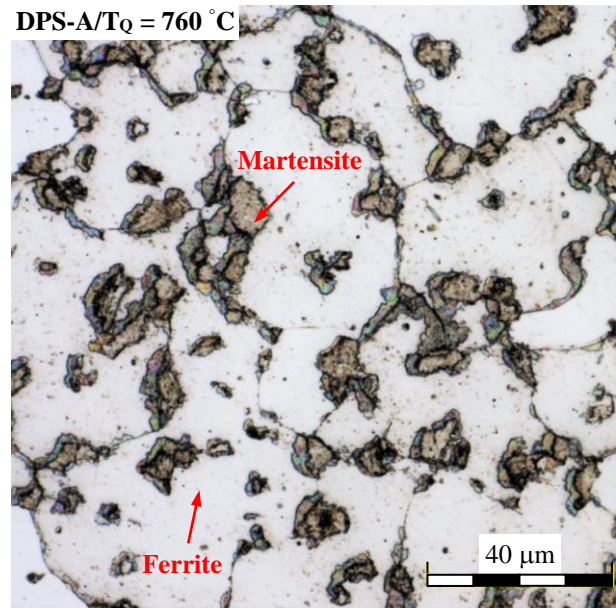
Fig.3. Structures of the dual-phase steels.

of martensite in structures (and decreasing the volume fraction of ferrite), an increase in the size of the martensite islands is observed (Fig.3), as well as a tendency of their connection and the formation of a network around the ferrite grains.

The raising of the heating temperature (T_Q) also determined an increase of ferrite microhardness (Tab.1 and Fig.2). The increasing ferrite microhardness was caused, most probably, by an

increase in the amount of interstitial atoms (C, N) and density of dislocations in the crystal lattice ofthis phase, [5, 13, 17, 21].

The results obtained from the tensile testing applied to the intercritical quenched specimens are presented in Tab.2 and Figs.4 - 7.

Table 2. Ultimate tensile strength and total elongation (average values)

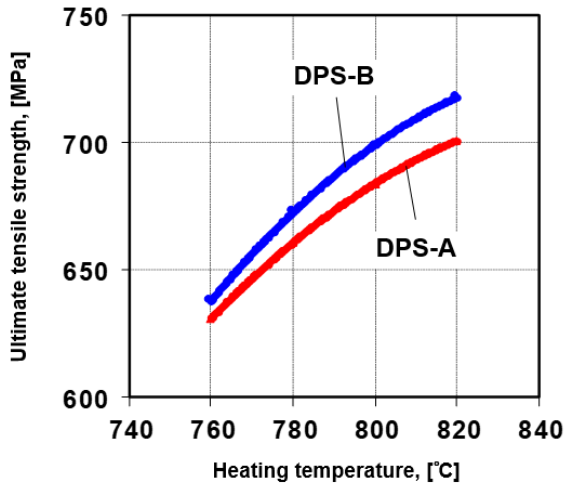| T_Q, °C	760		780		800		820	
Steel	DPS-A	DPS-B	DPS-A	DPS-B	DPS-A	DPS-B	DPS-A	DPS-B
R_m, MPa	631	638	661	673	684	699	701	718
A_5, %	24.46	23.29	22.01	20.95	20.08	19.29	19.04	18,59

Fig.4. Influence of the heating temperature on the ultimate tensile strength.
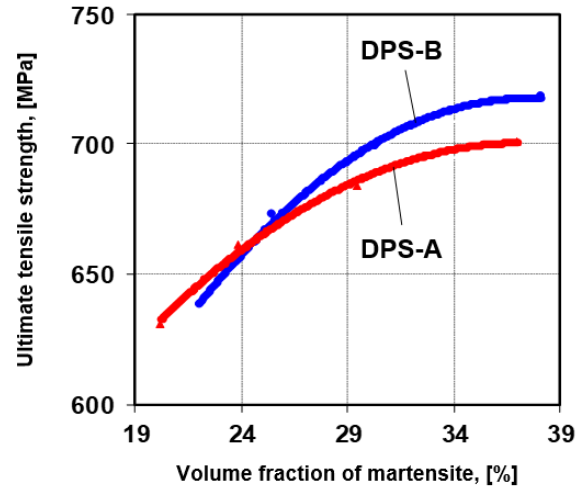
Fig.6. Influence of the volume fraction of martensite on the ultimate tensile strength.
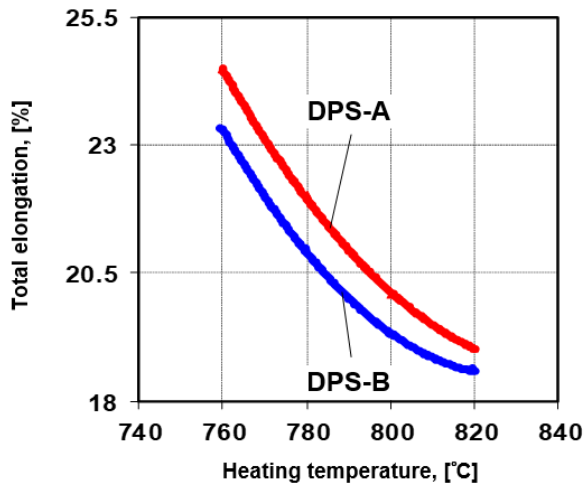
Fig.5. Influence of the heating temperature on the total elongation.
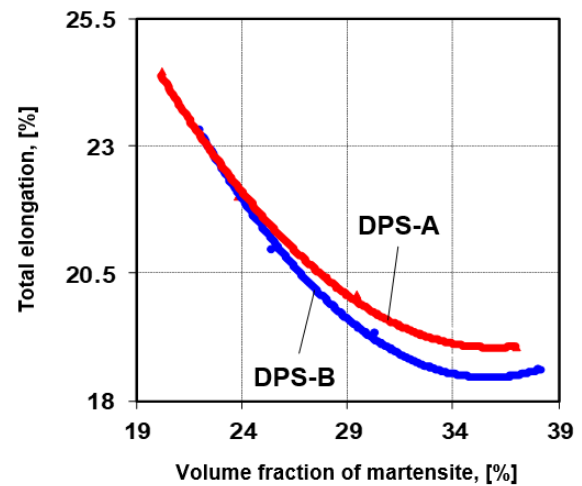
Fig.7. Influence of the volume fraction of martensite on the total elongation.

Raising the heating temperature (T_Q), so the increase in the volume fraction of martensite (V_M) and ferrite microhardness (HV0.01), has led to increasing of the strength characteristics (R_m) and the decrease of deformability (A_5). Thus, the ultimate tensile strength (R_m), determined for the specimens made of the DPS-A steel, increased with 70 MPa, from 631 MPa ($T_Q = 760$ °C) to 701 MPa ($T_Q = 820$ °C), and the total elongation (A_5)

decreased with 5.42 percent, from 24.46% ($T_Q = 760$ °C) to 19.04% ($T_Q = 820$ °C); in the case of DPS-B steel specimens, the ultimate tensile strength (R_m) increased with 80 MPa, from 638 MPa ($T_Q = 760$ °C) to 718 MPa ($T_Q = 820$ °C), and the total elongation (A_5) decreased with 4.70 percent, from 23.29% ($T_Q = 760$ °C) to 18.59% ($T_Q = 820$ °C).

8

The slightly higher carbon and manganese content of DPS-B steel (compared to DPS-A steel) determined the obtaining of slightly higher values of the volume fraction of martensite in the structure, with effect on the ultimate tensile strength and total elongation; for example, for $T_Q = 760$ °C the ultimate tensile strength was 638 MPa compared to 631 MPa and the total elongation was 23.29% compared to 24.46%, and for $T_Q = 520$ °C the ultimate tensile strength was 718 MPa compared to 701 MPa and the total elongation of 18.59% compared to 19.04%.

The results obtained for the two dual-phase steels with low manganese content (DPS-A and DPS-B) were compared with those determined from previous research (Tab.3, [14, 15]), performed on dual-phase steel with 1.90% Mn (0.09% C, 1.90% Mn, 0.06% Si, 0.10% Cr, 0.09% Ni, 0.03% Mo, 0.012% Al, 0.15% Cu, 0.019% P, 0.011% S), alloy noted DPS$_{1.90Mn}$ in this article. The higher manganese content determined a lower position of the critical points A_{c1} and A_{c3} ($A_{c1} = 703$ °C, $A_{c3} = 839$ °C) compared to the DPS-A and DPS-B alloys and for this reason, the intercritical quenching of DPS$_{1.9Mn}$ steel was performed from temperatures between 740 and 820 °C (compared to 760 – 820 °C for DPS-A and DPS-B alloys).

Table 3. The volume fraction of martensite and mechanical properties for the DPS$_{1.90Mn}$ (average values).

T_Q, °C	V_M, %	R_m, MPa	A_5, %
740	25.10	883	16.68
760	42.51	957	15.18
780	57.10	1018	14.04
800	68.32	1086	12.99
820	78.10	1135	12.06

There are important differences between the two data sets (Tabs.1 – 3, Figs.8 and 9), differences determined by the very different manganese content of the two categories of steels. In DPS$_{1.9Mn}$ steel, the position of the critical points A_{c1} and A_{c3} led to the obtaining, by intercritical heating, of a higher amount of austenite, which determined the formation, on quenching, of a higher the volume fraction of martensite; thus, for the temperature range 760 – 820 °C, the volume fraction of martensite in the structure was higher by percentages between 22.32 and 41.12%. Because of this, the values of ultimate tensile strength and total elongation at DPS-A and DPS-B steels were much different from those of DPS$_{1.90Mn}$ steel; the total elongation was higher with percentages between 9.28 and 6.98% and the ultimate tensile strength was lower with values between 326 and 434 MPa.
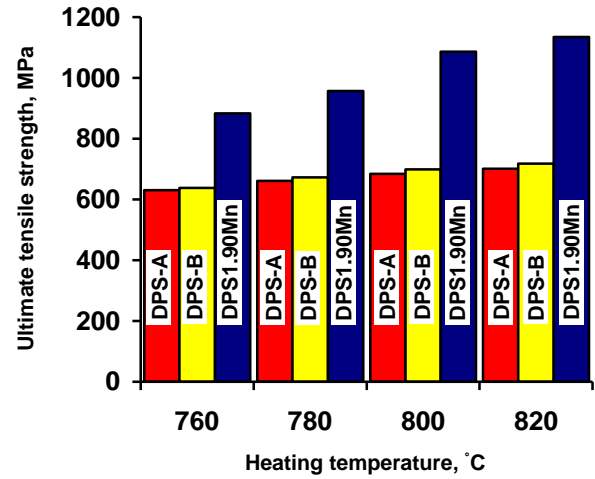
Fig.8. Influence of the heating temperature on the ultimate tensile strength of the dual-phase steels (DPS-A, DPS-B, and DPS$_{1.9Mn}$).

Fig.9. Influence of the heating temperature on the total elongation of the dual-phase steels (DPS-A, DPS-B, and DPS$_{1.9Mn}$).

CONCLUSIONS

The increase of the heating temperature in the intercritical range (A_{c1} - A_{c3}), between 760 °C and 820 °C, led to the increase of the volume fraction of martensite and the ferrite microhardness in the structures resulting from intercritical quenching; this fact has increased the mechanical strength and reduced the deformability of the dual-phase steels.
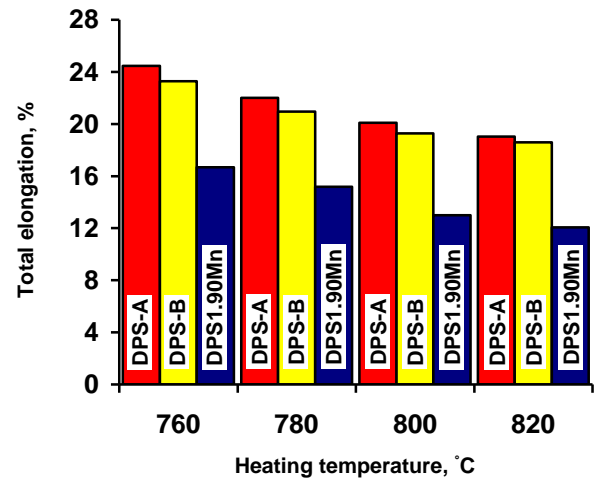
The slightly higher carbon and manganese content of DPS-B steel (compared to DPS-A steel) determined the obtaining of slightly higher values of the volume fraction of martensite in the structure, with effect on the ultimate tensile strength and total elongation; the ultimate tensile strength was higher by 7 to 17 MPa, and the total elongation was lower by percentages between 1.17 and 0.45%.

Compared to the mechanical properties of a dual-phase steel with 1.90% Mn (a "classic" dual-phase steel), low manganese steels (0.511% Mn and 0.529% Mn) had much different values of the ultimate tensile strength and total elongation; the ultimate tensile strength was lower by 326 to 434 MPa, and the total elongation was higher by percentages between 9.28 and 6.98%.

ACKNOWLEDGEMENTS

NOMENCLATURE

Ac_1 - critical point, $°C$;

Ac_3 - critical point, $°C$;

T_Q - heating temperatures from the intercritical quenching, $°C$;

V_M - the volume fraction of martensite, %;

$HV0.01$ - ferrite microhardness;

R_m - ultimate tensile strength, MPa;

A_5 - total elongation, %;

$DPS-A$ - dual-phase steel with 0.511% Mn;

$DPS-B$ - dual-phase steel with 0.529% Mn;

$DPS_{1.90Mn}$ - dual-phase steel with 1.90% Mn.

REFERENCES

1. S. Keeler, M. Kimchi, P.J. Mooney, Advanced High-Strength Steels. Application Guidelines Version 6.0. http://www.worldautosteel.org/ downloadfiles/ AHSS%20Guidelines%20V6/00 AHSSGuidelines_V6_20170430.pdf .

2. D.K. Matlock, J.G. Speer, E. De Moor, P.J. Gibbs, Recent Developments Advanced High Strength Steels for Automotive Applications: An Overview, *Engineering Science and Technology, an International Journal* **15** (1), 1-12 (2012).

3. C.C. Tasan, M. Diehl, D. Yan, M. Bechtold, F. Roters, L. Schemmann, C. Zheng, N. Peranio, D. Ponge, M. Koyama, K. Tsuzaki, D. Raabe, An Overview of Dual-Phase Steels: Advances in Microstructure-Oriented Processing and Micromechanically Guided Design, *Annual Review Materials Research* **45**, 391-431 (2015).

4. D. Chatterjee, Behind the Development of Advanced High Strength Steel (AHSS) Including Stainless Steel for Automotive and Structural Applications – An Overview, *Materials Science and Metallurgical Engineering* **4** (1), 1-15 (2017).

5. S.A. Golovanenko, N.M. Fonshteyn, Dual-phase alloyed steels, Metallurghia, 1986.

6. M.S. Rashid, Dual-Phase Steels, *Annual Review of Materials Science* **11**, 245-266 (1981).

7. R.G. Davies, C.L. Magee, Physical Metallurgy of Automotive High Strength Steels, *Structure and Properties of Dual-Phase Steels*, Ed. TMS-AIME, 1-19 (1981).

8. G.R. Speich, Physical Metallurgy of Dual-Phase Steels, *Fundamentals of Dual-Phase Steels*, Ed. TMS-AIME, 3-46 (1981).

9. R. Nadlene, H. Esah, S. Norliana, M.A. Mohd Irwan, Study on the Effect of Volume Fraction of Dual Phase Steel to Corrosion Behaviour and Hardness, *World Academy Science, Engineering and Technology* **5** (2), 564-567 (2011).

10. M. Pouranvari, Tensile Strength and Ductility of Ferrite-Martensite Dual Phase Steels, *Metallurgical and Materials Engineering* **16** (3), 187-194 (2010).

11. E.N. Birgani, M. Pouranvari, Effect of martensite volume fraction on the work hardening behavior of dual-phase steels, http://konsys-t.tanger.cz/ files/proceedings/metal_09/Lists/Papers /107.pdf.

12. C. Dulucheanu, T. Severin, T.L. Irimescu, D.A. Cerlinca, Influence of the cycles of heat treatments on the structure and mechanical properties of a dual-phase steel with low manganese content, *International Multidisciplinary Scientific GeoConference Surveying Geology and Mining Ecology Management, SGEM* **20**, 6.2, 11-18 (2020).

13. C. Dulucheanu, T. Severin, A. Potorac, L. Irimescu, Influence of intercritical quenching on the structure and mechanical properties of a dual-phase steel with low manganese content, *Materials Today: Proceedings* **19**, 3, 941-948 (2019).

14. C. Dulucheanu, N. Bancescu, T.L. Severin, The Influence of Quenching Medium on the Structure and Mechanical Properties of the Dual-Phase Steel with 0,09% C, 1,90% Mn, *Metalurgia International* **XVI**, 5, 25-28 (2011).

15. C. Dulucheanu, N. Bancescu, T. Severin, Technological Characteristics of a Dual-Phase Steel with 0,09% C and 1,90% Mn Obtained by Intercritical Quenching, *Advanced Materials Research* **814**, 60-67 (2013).

16. C. Dulucheanu, N. Bancescu, M., Baesu, The Corrosion Behavior in 3,5% NaCl Solution of a Dual-Phase Steel with 0.094% C and 0.53% Mn, *International Multidisciplinary Scientific GeoConference Surveying Geology and Mining Ecology Management, SGEM* **2**, 6, 327-334 (2015).

17. C. Dulucheanu, T. Severin, The Influence of Ultrasounds on the Structure of some Low Carbon and Manganase Dual-Phase Steels,

International Multidisciplinary Scientific GeoConference Surveying Geology and Mining Ecology Management, SGEM **17**, 63, 85-92 (2017).

18. C. Dulucheanu, T. Severin, A. Potorac, L. Irimescu, Critical points in solid-state phase transformation of a steel with 0.087% C and 0.511% Mn, determined through dilatometric analyses, *Bulgarian Chemical Communications* **50**, Special Issue G, 158-164 (2018).

19. C. Dulucheanu, T. Severin, A. Potorac, L. Irimescu, J. Javorova, Influence of initial structure on the critical points in solid-state phase transformation of some hypoeutectoid steels, *Bulgarian Chemical Communications* **51**, Special Issue F, 26-33 (2019).

20. K. Burikova, G. Rosenberg, http://metal2013. tanger.cz/files/proceedings/metal_09/Lists/Papers /032_e.pdf.

21. S.S. Hansen, R.R. Pradhan, Structure/Property Relationships and Continuous Yielding Behavior in Dual-Phase Steels, *Fundamentals of Dual-Phase Steels*, Ed. TMS-AIME, 113-144 (1981).

Recycling rejected silicon wafers and dies for high grade PV cells

G. Golan[1], M. Azoulay[1], G. Orr[2*]

[1]Electrical and Electronics Dept., Ariel University, Ariel 40700, Israel

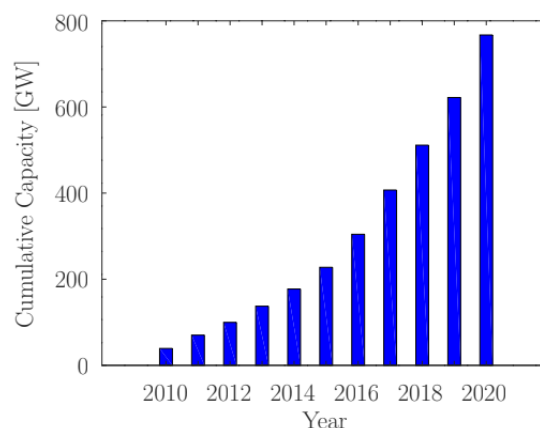*[2]Physics Dept., Ariel University, Ariel 40700, Israel*

Exponential growth in solar panel production and energy storage solutions has resulted in pressure on the supply of solar cell materials. Another environmental challenge stems from the fact that panels installed in the 90s and the beginning of the 2000s have reached their end of life and are being discarded in landfills. Hence, in this work, we focus on recycling silicon wafers and dies by stripping previous structures from the die using potent acids, after which its base material is characterized and binned. We demonstrate the process for silicon p-type substrates where n-type doping is attained by using a simple solution of phosphoric acid, which is diffused into the substrate using a furnace, thus creating a PN junction. If the substrate is n-type, it could be replaced by boric acid. This is followed by deposition of a conductive antireflective coating, bus bars, and rear wafer metal coating. The initial demonstrated laboratory results indicate the feasibility of recycling wafers using simple, low-cost standard industrial methods.

Keywords: PV, Silicon Recycling, solar cell recycling

INTRODUCTION

Renewable energy sources for electrical energy generation have become an increasing concern in most countries due to the environmental impact associated with the use of fossil fuels. In addition, reducing a country's dependence on fossil fuel further increases its self-reliance and improves a nations balance of trade, thus boosting its economy. Some countries have initiated programs increasing economic incentives to companies and individual households for developing, improving efficiencies, or increasing the capacity of renewal energy sources. In a recent report [1] the International Renewable Energy Agency estimates the current cost of PV electrical generation at optimal locations, has reached prices that are comparable to the lower end of fossil fuel costs. The various steps of manufacturing solar panels from raw materials are energy-intensive and include the use of large amounts of water and toxic chemicals. Therefore, expecting the rapid growth of silicon used for solar energy generation since the late 90s of the previous century, research was conducted for initiating environmentally benign solar cell manufacturing [2]. The predicted increase in solar panel production and installations [1] and the 25-year life expectancy of a solar panel have initiated various End of Life (EOL) management programs [3-6].

Fig.1. Cumulative capacity exponential growth between 2010 and 2020, based on [7]

The exponential growth of solar energy generation (Fig.1.) having a capacity of 39.2 GW in 2010, rapidly increasing to 767.2 GW in 2020, and expected to rise to 4,500GW by 2050 [6] will lead to an increase in PV panel waste. The move to a carbon-free and more sustainable energy production is being championed by PV-based solar panels. As production has been increasing exponentially in the past two decades, recycling the raw materials from the fabs and end-of-life panels is of prime importance. Understanding the negative impact of the PV waste and trying to limit it, the EU has decided to include PV panels in the waste of electrical and electronic equipment directive (WEEE). The US is expected to follow soon (Some states have adopted the European WEEE). As a result PV manufacturers and distributors are legally required to collect and recycle end-of-life PV

* To whom all correspondence should be sent:
gadygo@ariel.ac.il, gilad.orr@ariel.ac.il

products. Most silicon solar cells are based on single-crystal silicon (monocrystals) grown by the Czochralski technique and polycrystalline silicon casting. While there are more efficient materials for photovoltaic energy generation than single-crystal silicon, they are not commercially viable for large area applications. In 2015, crystalline silicon had approximately 93% of the market share of solar modules, with 24% going to the monocrystals and 69% going to the polycrystalline solar cells [8]. The larger market share of the polycrystalline solar cells is due to the significantly lower production costs, but this comes at a price of lower efficiency compared to the single crystal silicon. For most uses, where space or weight is not a concern the polycrystalline solar cells are appropriate. In places where space and weight are restricted, single crystal silicon, due to its higher efficiency is better suited. When dealing with monocrystal-based photovoltaic cells, higher-quality crystals result in higher conversion efficiency, but it comes at an economical price. Integrated circuit grade silicon is probably the most efficient base material for fabricating silicon solar panels due to its low defect density, but the lengths and costs for obtaining it are prohibitive for its wide application in terrestrial energy generation, where the capital investment per Watt is the key driving force. To reduce costs solar grade silicon monocrystals with a much higher level of defects and impurities are being introduced [9]. Another concern that needs to be addressed is the recycling of the panels when they reach their end of life (EOL). In this respect, rare metals and silicon cells retain their value and should be salvaged using various techniques [4,5]. One untapped resource of high quality near defect-free silicon is rejected dies and wafers. With an estimated 90% yield during full production [10] we are left with 10% rejected dies. Currently, state-of-the-art fabs are producing integrated circuits with wafer diameters of 300 mm (12") while the next standard size for such fabs, is projected to be 450 mm (18"). This provides an abundant supply of silicon for producing high-quality solar panels. In this article, we will present a relatively environmentally friendly method for recycling silicon from the rejected wafers.

MATERIALS PREPARATION

This work based on experiments conducted by our groups, suggests a method for recovering rejected silicon dies, wafers and residual silicon which resides on the rims of the processed wafers. In order to keep the text clear, we shall generally refer to all the recovered silicon as dies. The process results in PN photovoltaic structures composed of In_2O_5Sn / n-Si / p-Si (ITO, n-type silicon, p-type silicon).

Stripping

The dies were etched in after which the conductivity and type were measured. This assists us with defining the type of base material to deposit prior to diffusion (Phosphorous/Arsenic or Boron/Gallium). Similar die types are binned together. In this article we shall describe the process for a p-type substrate. Standard cleaning recipe was applied to the dies with an optional oxide strip using between the first step (SC-1) and the second step (SC-2). When using those steps, the rare metals can be recovered using the processes described in [4].

Donor/Acceptor diffusion

The samples were spin coated using a solution of 1:1 ratio of phosphoric acid and ethanol (H_3PO_4:C_2H_5OH). If the substrate is n-type one can replace the phosphoric acid with boric acid (H_3BO_3). The samples were place in a furnace with an ambient atmosphere pre-baking them at a temperature of 150°C for 10 minutes drying the newly applied coating. The temperature was raised to a temperature of 900°C for 6 hours slowly cooling it to a level of 600°C, this procedure allows for propper diffusion while reducing destructive glass phases. Dopant concentration was evaluated using ICP-OES [11] which can trace down to approximately $N_d{\sim}10^{14}$ [cm^{-3}].

Transparent Conductive Oxide coating

Although much work was conducted in the past 20 years, on the topic of environmentally sustainable, indium free Transparent Conducting Oxides (TCOs), for example [12,13] , in this work we used ITO with the standard application methods. Transparent conductive films of In_2O_5Sn were deposited by RF sputtering using an ITO ceramic (90 wt% In_2O_3, 10 wt% SnO_2). Substrates were cleaned using ultra pure deionized water isopropyl alcohol and acetone in an ultrasonic cleaner bath for 20 minutes. This was followed by drying using a flow of nitrogen gas. The RF sputtering chamber was purged with Ar and a working pressure of 100 mTorr was maintained. Surface oxidation was removed in the pre-

sputtering stage. A film of approximately 250nm was deposited on the surface of the materials with the procedure tested using microscope slides prior to the actual deposition. The deposited film was annealed in a tube furnace in an oxygen saturated environment supported by a 0.5 sccm gas flow at a temperature of 400°C. Optical transparency of the In_2O_5Sn films was measured in the UV/VIS using a Jasco V-730. Additionally, it was used in reflective mode to measure the film thickness [14] using the SLM-907 specular reflectance accessory. Fig.2. illustrates the transmission of the glass substrate and the ITO deposition on the glass substrate.
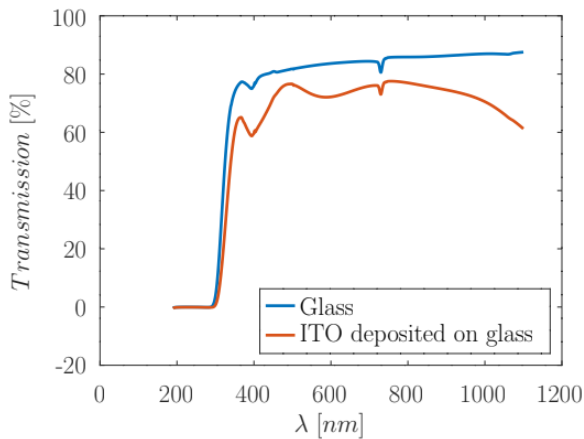
Fig.2. Optical transmission of the ITO on a glass substrate compared to the transmission of the glass substrate

The optical transmission of the ITO excluding the glass substrate in the 420-1100nm range is given in Fig.3.
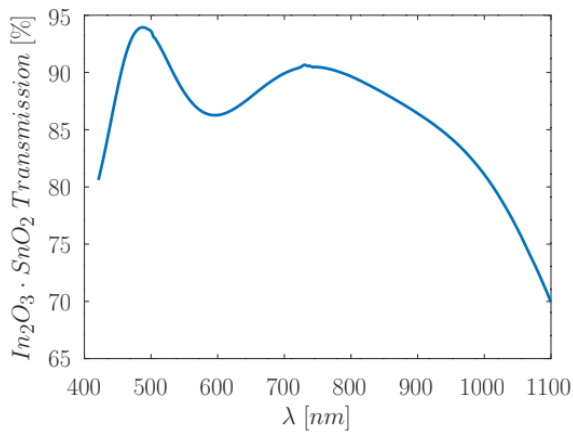
Fig.3. Optical transmission of the ITO excluding the glass substrate

As can be seen in Fig.3, the optical transmission at 500nm is 93.6% which compares favorably with published data [15,16]. Inkjet printing of the collector bus bar and finger aluminum electrodes

were tested with inconclusive results. As a result we opted for the traditional method of applying aluminum electrodes by thermal evaporation deposition.

A four-point measurement of the In_2O_5Sn deposited layer resistance was conducted before and after the diffusion validating the resistivity of the layer. Fig.4. illustrates the resistivity obtained using three different samples from three different batches.
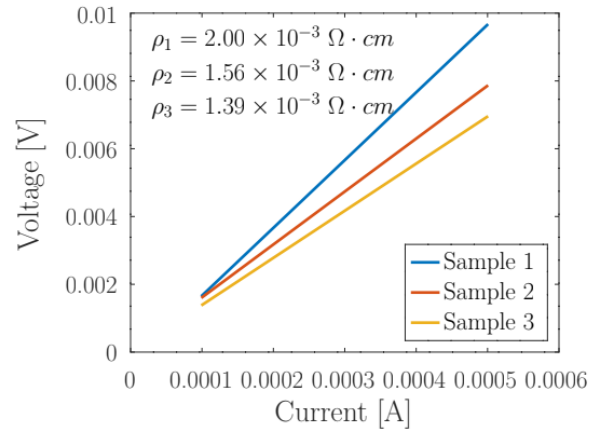
Fig.4. Resistivity of the ITO deposited layer of three different batches as extracted from a four point measurement

The resistivity results correspond with published data [16]. A hot probe experiment identified the type of semiconductor layer after the diffusion process a detailed account of the measurement can be found in [17]. During the various processes the surface structure was studied and documented using a metallurgical microscope.

EXPERIMENTAL RESULTS

A standard photovoltaic structure with a thin emitter fabricated at the top surface using a p-type substrate is demonstrated in Fig.5.
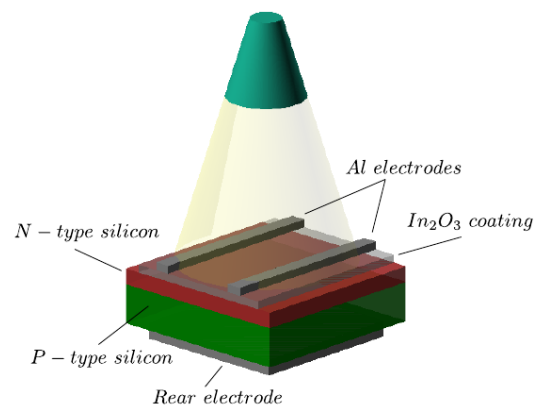
Fig.5. Photovoltaic cell structure

The wavelength dependent short circuit current is approximated by

$$J_{sc}(\lambda) = \frac{q\,(\lambda)(1-R_f)\alpha L_p}{\alpha^2 L_p^2 - 1}\Phi_e \qquad (1)$$

With Φ_e presenting an emitter factor which depends on doping levels and depth of doping:

$$\Phi_e = \frac{\frac{S_p L_p}{D_p} + \alpha L_p - e^{-\alpha H_e}\left(\frac{S_p L_p}{D_p}\cdot\cosh(h_e/L_p) + \sinh(h_e/L_p)\right)}{\frac{S_p L_p}{D_p}\sinh(h_e/L_p) + \cosh(h_e/L_p)}$$

$$- \alpha L_p e^{-\alpha H_e}\} \qquad (2)$$

Where:

$\phi(\lambda)$ — photon flux $[\#photons/sec\cdot m^2]$

R_f — reflectance of the active surface of the cell

α — absorption coefficient of the semiconducting material $[cm^{-1}]$

L_p — diffusion length of the minor charge carriers in the emitter $L_p = \sqrt{D_p\cdot\tau_p}\,[cm]$

S_p — surface recombination velocity for minor charge carriers $[cm/s]$

h_e — depth of the emitter $[cm]$

D_p — diffusion coefficient of minor charge carriers in the emitter $[cm^2/s]$

$J_{ph} = q\cdot(\lambda)$ the photon flux current is referred to as the photon flux which is the current given that every photon generates an electron hole pair. In order to get a grasp of the behavior of the short circuit current Eq. (1) one has to observe that the emitter factor Eq. (2) has the form

$$\Phi_e \approx C - Be^{-t} \underset{t\to\infty}{\to} C \qquad (3)$$

In which C is a constant depending on the minor charge carrier attributes (L_p, D_p) which are donor density dependent, the depth h_e and the surface recombination velocity S_p. The surface recombination velocity depends on both the surface defects and doping levels. For a passivated surface the doping level is $N_s \approx 10^{18} - 10^{19}$. The surface recombination velocity is given by [18, 19]

$$S_p = 10^{-16} N_s \qquad (4)$$

Fig.6 shows the calculated short circuit current as a function of the depth of the emitter.

For the above parameters it can be seen that the optimal depth of the emitter is approximately 3μm. The current is wavelength dependent on three accounts. Two external ones which are the photon flux, and the reflection R_f and an internal one being the absorption coefficient α.
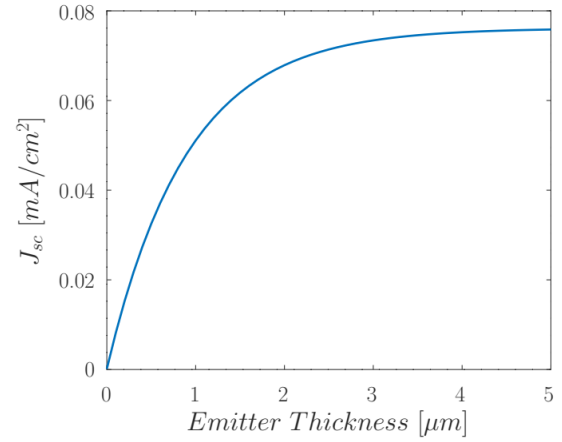
Fig.6. Short circuit current as a function of the depth of the emitter for: $\lambda = 500nm$; $R_f(\lambda) = 0.05$ $\alpha(\lambda) = 1.11 \times 10^4$; $S_p = 200\,[cm/s]$; $D_p = 13\,[cm^2/s]$; $\tau_p = 10\mu s$; $J_{ph}(\lambda) = 0.08\,[mA/cm^2]$

Reflectance

R_f is a significant parameter as it has a considerable influence on the efficiency of the PV cell as is seen in Eq. (1). On bare silicon $R_f > 30\%$ reducing the efficiency considerably. In order to decrease the reflection loss in the visible and NIR range an anti-reflective coating is applied. The applied coating needs to shift the phase of the reflected light by half a wavelength, thus canceling each other out. This happens when the surface of the silicon and the applied coating are at a distance of $\lambda/4$, or

$$n_c d = \lambda/4 \qquad (5)$$

A further improvement (minimization of reflection losses) is obtained when the coating is the mean of the refractive indices i.e.

$$n_c(\lambda) = \sqrt{n_{air}\cdot n_{Si}} \qquad (6)$$

$$n_c(500nm) \approx 2.11$$

One such material that is both transparent and which provides an appropriate solution over most of the visible range is ITO. Fig.7 displays the refractive index and the square root of the refractive index of the silicon compared to the refractive index of ITO.

Our peak wavelength is about 500nm and according to the graph $n_{ITO}(500) \approx 2$ thus a deposition thickness of 125nm is appropriate for our purpose. As was seen in Fig.3, the low

resistivity of the ITO film on our samples accommodates the conduction of charge to the fingers and bus bars.
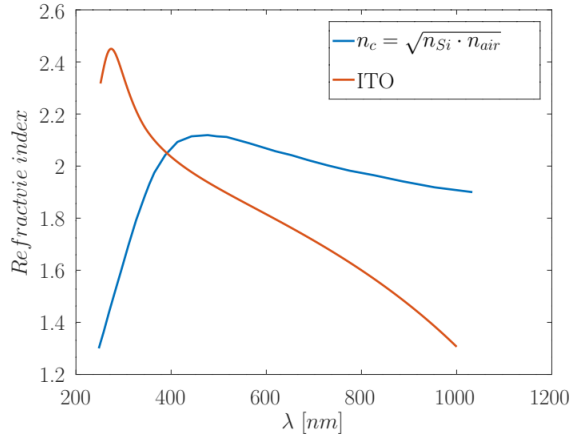
Fig.7. Comparison between the index of refraction of ITO and the square root of n_{Si} and n_{air}
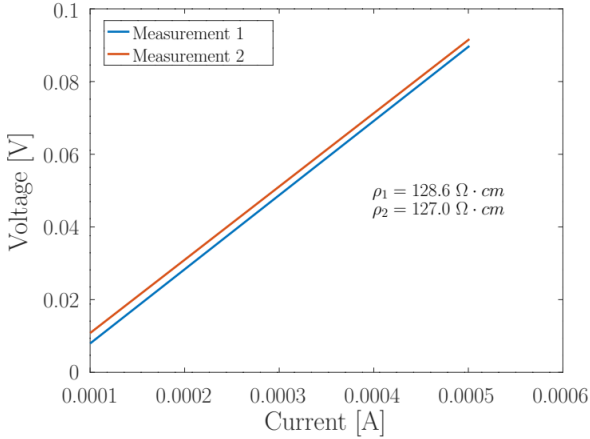
Fig.8. A four point measurement of the doped (emitter) layer

Post diffusion

The describe process's weakness is that, to date, it is not a completely controlled process. While during the classic method the flow of the dopant gas is controlled, some of the spin coated material evaporates and we need to resort to ICP-OES measurements in order to estimate dopant concentration. The resistivity of the doped layer was measured using a four point measurement as shown in Fig.8.

The resistivity result of ~$127\Omega \cdot$ cm corresponds with a dopant density of 4×10^{14} cm^{-3} [20] which was confirmed by the ICP-OES measurement which is approximately 5×10^{14} cm^{-3} (close to the detection limit of the phosphorus). Following the resistivity characterization the I-V characteristic was measured at different temperatures. Fig.9

indicates that the material displays a regular PN junction behaviour.
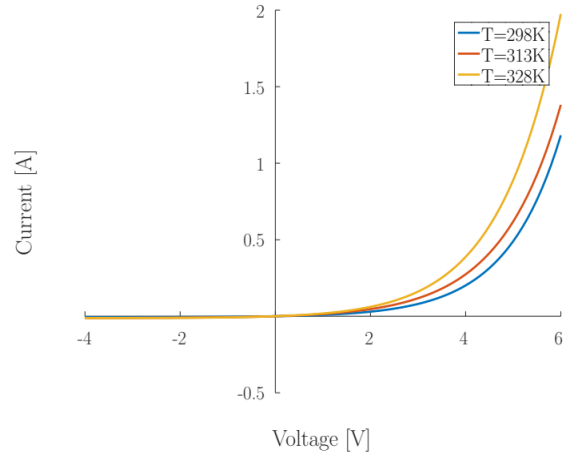
Fig.9. Device I-V characteristic at several temperatures

The calculated potential of the junction is 0.5 V while the actual open circuit voltage was found to be lower than 0.1 V. This is due to the high losses in this device which is in its preliminary research stages.
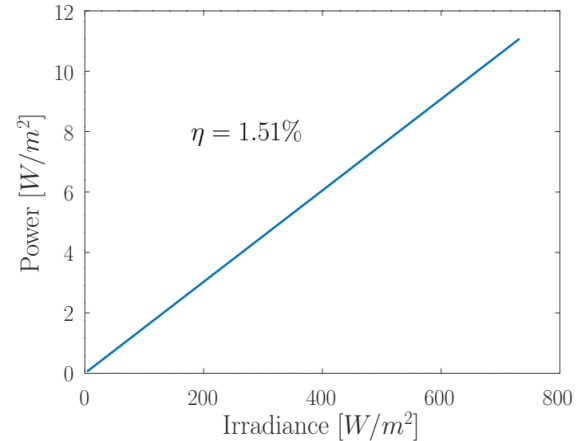
Fig.10. Device output power as a function of the irradiance

After depositing a 150nm ITO coating and adding the bus bar, fingers and back electrode, the photo-current was measured under various intensities which were controlled using a UNI-T UT383BT luxmeter. The measured illuminance was converted to irradiance based on a recent guide which tries to sort out the various conversion factors [21]. Based on their recommendation we used a 116 [lux/W/m²]. Fig.10 displays the devices output power as a function of the irradiance.

The slope of the graph shows the efficiency of the device, which is 1.51% in the above measurement.

DISCUSSION

A recent study [22] estimates the EOL cost of a PV panel at 6.72 USD/m^2, while the cost of the actual recycling including 0.25 USD/m^2. Most of the cost consists of panel transport and processing of PV waste. We have focused on recycling single crystal wafers which are repurposed. As such, in this work we have used the standard stripping methods which are applied in microelectronics, though better, cheaper and environmentally benign methods do exist as discussed in [4]. Stripping methods are discussed extensively in literature, our work was focused on demonstrating preliminary work consisting of a simple method for doping stripped single crystalline silicon creating a PN junction. The presented efficiencies are considered low, but we have demonstrated it is a viable method, which still needs to be perfected.

CONCLUSIONS

This work presents a viable method for recycling and re-purposing used silicon wafers for PV use. The preliminary work shows that standard stripping methods followed by a newly suggested method for diffusing dopants does provide a working PV cell. Both optical and electrical properties of the resulting device were presented. The output power density's dependence on the incident irradiance resulted in a 1.51 % efficiency, which is an order of magnitude lower than expected. As this work was intended as a feasibility study, the result shows promise. Following this work we intend to improve the efficiency of a single crystal wafer cell and present a method for assembling an efficient solar panel from the salvaged wafers. In the future we will extend this work to recycling polycrystalline wafers which are abundant in the ever increasing retired solar panels.

REFERENCES

1. IRENA, Renewable Power Generation Costs in 2020, Int., Renewable Energy Agency, 2021.
2. YS Tsuo, JM Gee, P Menna, DS Strebkov, A Pinov, and V Zadde. Environmentally benign silicon solar cell manufacturing. In *Report, 2nd World Conference and Exhibition on Photovoltaic Solar Energy Conversion, National Renewable Energy Laboratory, Golden, CO*, 1998.
3. Fabiana Corcelli, Maddalena Ripa, Enrica Leccisi, Viviana Cigolotti, Valeria Fiandra, Giorgio Graditi, Lucio Sannino, Marco Tammaro, and Sergio Ulgiati. *Sustainable urban electricity supply chain–indicators of material recovery and energy savings from crystalline silicon photovoltaic panels end-of-life*. Ecological indicators, 94:37–51, 2018.
4. Flavia CSM Padoan, Pietro Altimari, and Francesca Pagnanelli. Recycling of end of life photovoltaic panels: *A chemical prospective on process development.* Solar Energy, 177:746–761, 2019.ingsmill Bond, et al. A new world: The geopolitics of the energy transformation, 2019.
5. Jeongeun Shin, Jongsung Park, and Nochang Park. A method to recycle silicon wafer from end-of-life photovoltaic module and solar panels by using recycled silicon wafers. Solar Energy Materials and Solar Cells, 162:1–6, 2017.
6. Stephanie Weckend, Andreas Wade, and Garvin Heath. End-of-life management: Solar photovoltaic panels. Technical report, National Renewable Energy Lab.(NREL), Golden, CO (United States), 2016. [1] Thijs Van de Graaf, Kingsmill Bond, et al. A new world: The geopolitics of the energy transformation, 2019.
7. G. Masson and I. Kaizuka. Trends in Photovoltaic Applications. IEA-PVPS, 2021.
8. E Płaczek-Popko. Top pv market solar cells 2016. Opto-Electronics Review, 25(2):55–64, 2017.
9. Yves Delannoy. Purification of silicon for photovoltaic applications. Journal of Crystal Growth, 360:61–67, 2012.
10. Peter Van Zant and P Chapman. Microchip fabrication: a practical guide to semiconductor processing, volume 5. McGraw Hill New York, 2000.
11. A. Rietig and J. Acker. Development and validation of a new method for the precise and accurate determination of trace elements in silicon by icp-oes in high silicon matrices. J. Anal. At. Spectrom., 32:322–333, 2017.
12. C. Guillén and J. Herrero. Tco/metal/tco structures for energy and flexible electronics. Thin Solid Films, 520:1–17, 2011.
13. E. Fortunato, D. Ginley, H. Hosono, and D. Paine. Transparent conducting oxides for photovoltaics. Mrs Bulletin, 32:242–247, 2007.
14. D. P. Arndt, R. M. A. Azzam, J. M. Bennett, J. P. Borgogno, C. K. Carniglia, W. E. Case, J. A. Dobrowolski, U. J. Gibson, T. Tuttle Hart, F. C. Ho, V. A. Hodgkin, W. P. Klapp, H. A. Macleod, E. Pelletier, M. K. Purvis, D. M. Quinn, D. H. Strome, R. Swenson, P. A. Temple, and T. F. Thonn. Multiple determination of the optical constants of thin-film coating materials. Appl. Opt., 23(20):3571–3596, Oct 1984.
15. Fang, Xu et. al, Pulsed laser deposited indium tin oxides as alternatives to noble metals in the near-infrared region, Journal of Physics: Condensted Matter, 28(22) 2016.

16. Sang Mo Kim, Hyung-Wook Choi, Kyung-Hwan Kim, Sang-Joon Park, and Hyon-Hee Yoon. Preparation of ITO and IZO thin films by using the facing targets sputtering (FTS) method. J. Korean Phys. Soc, 55(5):1996–2001, 2009.

17. Bart Van Zeghbroeck. Principles of semiconductor devices. Colarado University, 34,2004.

18. Arturo Morales-Acevedo. Theoretical study of thin and thick emitter silicon solar cells. Journal of applied physics, 70(6):3345–3347, 1991.

19. N Stem and M Cid. Studies of phosphorus gaussian profile emitter silicon solar cells. Materials Research, 4:143–148, 2001.

20. WR Thurber, RL Mattis, YM Liu, and JJ Filliben. Resistivity- dopant density relationship for phosphorus-doped silicon. Journal of the Electrochemical Society, 127(8):1807, 1980.

21. Peter R Michael, Danvers E Johnston, and Wilfrido Moreno. A conversion guide: solar irradiance and lux illuminance. Journal of Measurements in Engineering, 8(4):153–166, 2020.

22. E. Markert, I. Celik and D. Apul. Private and externality costs and benefits of recycling crystalline silicon photovoltaic panels. Energies, Vol. 13 Num. 14, 2020.

Crystalline quality in aluminum single crystals, characterized by X-Ray diffraction and Rocking-Curve analysis

G. Orr[1*], G. Golan[2]

[1]Department of Physics, Ariel University, Ariel 40700, Israel
[2]Department of Electrical Engineering, Ariel University, Ariel 40700, Israel

Aluminum single crystals are tested using X-Ray Bragg diffraction, which may have applications in microscopy and electronics fabrication industry. Yet, their efficiency for x-ray beam diffraction depends on the accurate crystal orientation, the microstructure and imperfections. Moreover, the final sample that is formed from the as-grown crystal by cutting, grinding, polishing and chemical etching, introduces various surface defects that penetrate deep into the crystal affecting its natural structure. Defect penetration is attributed to the fact that ultra-pure aluminum single crystals are soft and ductile with a hardness in the range of 2~2.5 mho. This leads to lattice deformation, resulting in a deviation from the crystallographic orientation of the final device, affecting the diffraction intensity and an apparent shift in the Bragg angle. In this work we investigate the influence of processing aluminum single crystals by mechanical and chemical means using XRD and Rocking-Curve broadening as a quantitative indication concerning the depth of the damage. This is a preliminary step in supporting future work on the study of electrical conduction in aluminum single crystals. Supplementing electrical conductivity measurements of aluminum, quality assessment of defects in front cell aluminum conductors can assist in designing novel low resistance aluminum conductors replacing the currently widely used and relatively rare silver.

Keywords: Aluminum single crystals, X-Ray diffraction, crystal orientation, imperfections, PV cells

INTRODUCTION

The Conduction in elemental metallic crystals is still intensively investigated [1] and is of great technological importance in modern microelectronics and photovoltaics. Of the FCC metallic crystal family, aluminum is widely used in modern microelectronic fabrication as it is a relatively abundant, acceptable conductor which to some extent is superior to copper for it does not diffused into silicon at operating temperatures (< 450ºC). That said, with all the complications copper adds to device manufacturing aluminum's conductivity is only 63% compared to the conductivity of copper (0.0172 Ω·mm^2/m vs. 0.0282 Ω·mm^2/m). Thus increasing aluminum's conductivity has its merits. Current photovoltaic cell bus bar and finger technology consists of silver screen printing thus relying on a relatively rare and expensive metal. Replacing the silver with an abundant metal may reduce the production costs considerably, therefore given the considerations above aluminum is a good candidate. Depositing the aluminum on the silicon substrate does not require a conductive seed layer or a Ni barrier layer (as required for Cu), as it not a deep level impurity, further simplifying the process and reducing its cost. One veteran method which has re-emerged is

metal plating, with recent work demonstrating its viability [2]. Checking on Dimensions [3] shows that since the time of peak interest during 2012 there are on average 600 annual publications concerning using aluminum for front metallization of solar cells. As we have seen Al is inferior to Ag and Cu concerning its resistivity adding to a significant power efficiency loss due to series resistance resulting from the bus bars and fingers on the front side of the cell. Therefore further study is required in order to reduce the resistance of the Al front conductors. Lapovok et al. [1] demonstrated a 3.7% improvement (reduction) in resistivity from ρ = 2.96μΩ·cm to ρ = 2.85μΩ·cm following annealing at 600ºC for 48h. Following a similar treatment in a boron rich environment resulted in the resistivity dropping to ρ = 2.62 μΩ·cm i.e. a 11.5% in resistivity which is a significant improvement. This increase was attributed to reduced scattering centers due to a gettering effect and reduced defects due to the additional annealing. Increasing the layers height resulting in an increase of the conductors cross section may assist in reducing the series resistance though the geometry may need some redesigning to avoid shadowing. Thus understanding mechanisms of electrical conduction in single crystals can lead to methods for reducing the electrical resistance of the front solar cell conductors. Ultra-high-purity aluminum single crystals are a good starting point

---

* To whom all correspondence should be sent:
gilad.orr@ariel.ac.il, gadygo@ariel.ac.il

for such experimental work, and high resolution X-ray diffraction, a measurement technique for assessing crystal quality and defects. However, it is yet a significant challenge to determine the degree of crystalline perfection that will provide the optimal conditions for a significant improvement compared to the current accepted values. Every stage of the fabrication process has to be considered for its contribution to defect formation and elimination. Growing Aluminum single crystals was mostly investigated during several decades at the mid of the 20th century [4] by the well-known Bridgman method [5] or by using the grain growth technique (Fig.1).

Fig.1. Bridgman based growth furnace with a quartz compartment for growing the crystals in an inert environment

Recently, some new methods have been applied for growing single crystal foils of several metals [6] that can be used at an industrial scale. Yet, the deformation in the crystals was mostly studied by intentional stressing of the crystal in order to perform the deformation, as well as studying the effects of heat treatment and annealing processes and characterize the resulting microstructure by means of X-ray diffraction methods and high-resolution microscopy [7]. The crystal orientation is

precisely determined and oriented to the required direction, mostly to the {1,1,1}, {1,1,0} or {1,0,0} by the X-ray Laue method. This is followed by further XRD analysis for both final precise crystallographic orientations, as well as an initial assessment of the crystalline quality and microstructure. X-Ray Rocking Curve technique is applied in case of high crystalline quality assessment. Imaging methods such as optical microscopy, SEM and STEM, are carried out as well, for determining the physical microstructure that plays a significant role at the final X-Ray analysis. XRD peak shift, peak broadening and peak asymmetry are indicative of deformation, growth fault, twin fault and several additional crystalline disorders in the FCC metal element crystal (Aluminum single crystal in the current study). Detailed theoretical calculations and experimental results are described in [8]. The FCC structure is a closed packed structure in which the atoms are arrange in a three layer sequence resulting in a dense geometric packing. Fig.2 illustrates a 3D arrangement of three such layers.

$$(a) \qquad (b)$$
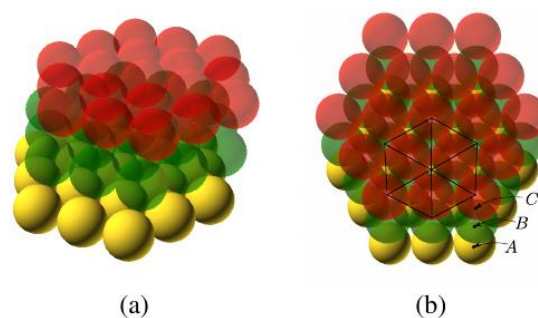
Fig.2. Representation of layers forming the FCC structure. (a) The recurring layer placement required for the FCC structure. (b) The actual location of the atoms missing the apex atom which is part of a top A layer (not shown)

The figure illustrates the layers of the atoms and the relative placement of each layer providing for the most compact filling. In Fig.2b the orientation of the FCC cell within the 3 layer framework is shown. As the image is missing a top A layer the apex atom is missing. The cell structure is a bit obscure and one has to imagine the structure from the vertices. Fig.3 elucidates the FCC cell within the layers.

The vertices atoms are illustrated by the violet spheres while the face centered atoms by the yellow spheres. As may be seen the apex atom and the bottom atom belong to the A layer placing them

one over the other. Following the perpendicular unit cell axis one can observe the {1,1,1} orientation in Fig.3b. The red bordered atoms highlight the vertex and face atoms at the lower layer, while the green bordered atoms highlight the ones of the layer above it. The vertices atoms of each layer form a large triangle bordering a smaller triangle created by the face atoms of that specific layer, with the smaller triangle being at a 180∘ angle to the one formed by the vertices. The triangles formed by the atoms in each layer are a mirror image of the other. Given we had a perfect crystal, processing it mechanically will introduce defects. Point defects having less long range influence on the crystals structure. On the other hand, layer movement along the slip planes due to stress, with the primary ones being along the {1,1,1} direction have much more influence for e.g. the line defects, the edge and screw dislocations.

(a)   (b)
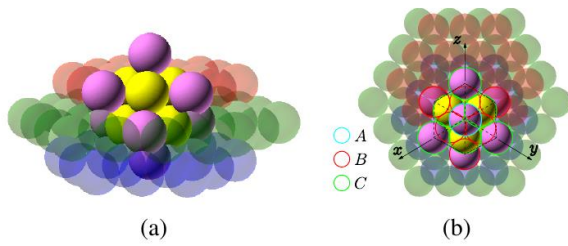
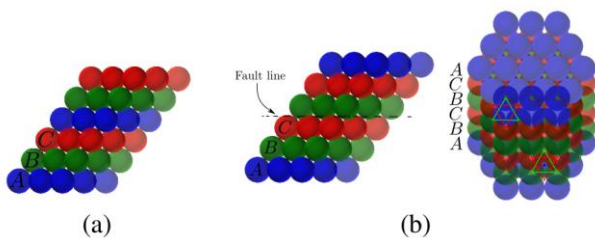**Fig.3.** SA FCC unit cell within the layers. (a) Side view of the FCC cell, (b) View of the cell from the {1,1,1} direction

More subtle, but of significant influence on the diffraction patterns, are the stacking faults resulting in fault lines Fig.4 and twins Fig.5.

(a)   (b)

Fig.4. Layer stacking with a missing layer. (a) Regular 3 layer compact stacking resulting in the FCC strucure. (b) Missing A layer (for example), resulting in the FCC cells missing the top or bottom atom creating a fault line

Stacking faults in which one layer is missing, results in an alternating sequence of two layered stacks which result in a hexagonal closed packed structure along that layer. It could also be viewed as the top and bottom FCC cells missing one apex or

base atom. Another stacking fault is when two adjacent layer switch positions as in Fig.5.
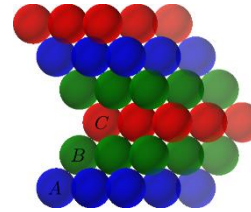
Fig.5. Layer stacking fault where two adjacent layers switch positions. This results in a bifurcation where the layers above the fault are a mirror image of the layers below it

Such an occurrence leads to a bifurcation with the layers on both sides of the fault proceed as mirror images of one another prompting the growth of two crystals with a common layer in two different directions. Such a fault may have a considerable effect on the peak broadening. As we are dealing with single crystals we do not expect to observe grain boundaries, but low angle tilt boundaries resulting from dislocations and faults are present and its correlation with the rocking curve peak broadening in a manner not yet fully understood. They are observed using STEM imaging as can be seen in Fig.6.
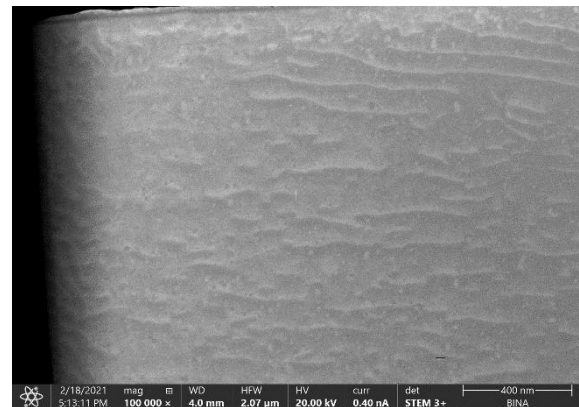
Fig.6. A ×100, 000 STEM image of low angle tilt boundaries, creating what is referred to as mosaic structures in aluminum

Those boundaries differ from grain boundaries as from their very essence the bulk has a growth orientation and only locally differ from this orientation due to a periodic array of dislocations and stacking faults. The degree of this misorientation may be observed by the rocking curve method and in future published work will be correlated with the electrical conductivity in aluminum.

EXPERIMENTAL RESULTS

Following the Bridgman crystal Growth of Aluminum single crystals, samples were prepared for the purpose of crystallographic orientation, XRD analysis, X-Ray Rocking Curve analysis and crystalline quality evaluation by STEM imaging. As the material is very soft and ductile initial fabrication was conducted using electro-erosion. Fig.7 illustrates the result of an aluminum sample after it was cut. The STEM image displays the highly damaged top surface as observed in Fig.7, which reduces the X-Ray intensity and increases the peak broadening.
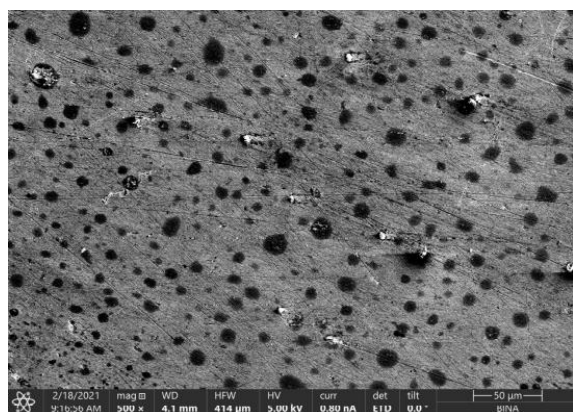
Fig.7. SEM image of the aluminum surface after cutting. The high pitting density, with the pit sizes reaching 20nm

ICP-AES measurements indicated that trace elements of brass exist in the samples. Tab.1. illustrates the trace elements within a sample compared to the trace elements found within the starting material and reference.

Table 1. ICP-AES results of several samples (PPM)

	Ag	Ca	Cu	Fe	Zn	Cr	S
Starting material	3.914	-	-	6.06	-	-	128.2
Reference	3.98	-	-	6.45	-	0.12	87.59
Al EDM cut	-	132.49	495.06	141.41	170.64	0.66	-

Post EDM cutting displays obvious incorporation of brass elements into the crystal material. Following this SEM imaging, a STEM sample was prepared using a FIB process with the cut perpendicular to the observed surface in Fig.7.

A magnified higher resolution STEM image (Fig.9), displays column structure ("membrane like") cavities with diameters corresponding to the previous pits observed in Fig.8.
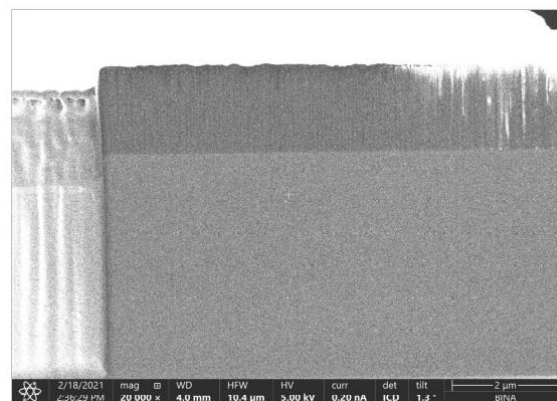
Fig.8. A low resolution STEM cross section image of the sample close to its surface. The damage to the machined layer can be clearly see, having the approximate thickness of 1.8μm
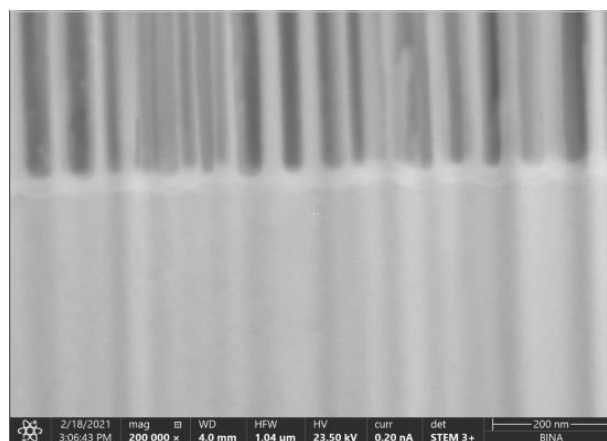
Fig.9. High resolution STEM image of the lamella prepared using the FIB technique

The image illustrates how the surface damage extends deep into the material altering its structure. This damage was found to propagate to a depth of approximately 2 mm with similar results reported in the past by Gorman et. al. [9]. Such damage results in reduced XRD intensity and considerable peak broadening. Those defects within the aluminum and on its external surfaces scatter conducting electrons and contribute to the resistivity. As the dimensions of the conductors are reduced, which is the case in the solar cell, the electrons interacting with the defects increase considerably resulting in a rise in resistivity. Fig.10 below, illustrates an example of the XRD data that was acquired from a crystal with relatively poor quality. As may be observed, the

diffraction pattern shows low peak intensity and mixed crystallographic orientation data.
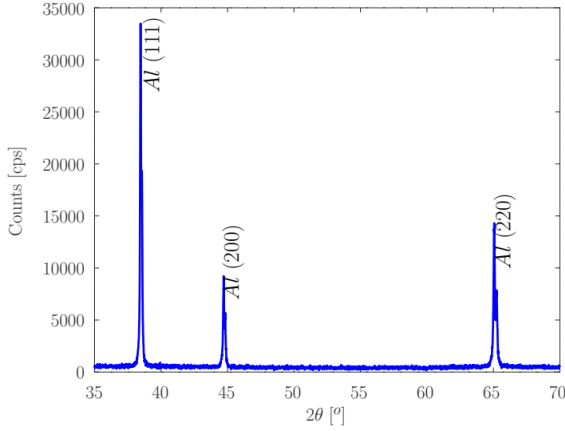
Fig.10. An example of {1,1,1} oriented Aluminum Crystal. Minor diffraction at the {2,0,0} and {2,2,0} orientations are also visible

Fig.11 below, shows an example of the XRD data that was acquired from a crystal of high quality and lattice perfection. A very high peak intensity at the range of 9e7 (20 millions counts), with a single distinguished peak (disregarding K_β) diffraction in the {1,1,1} crystallographic orientation.
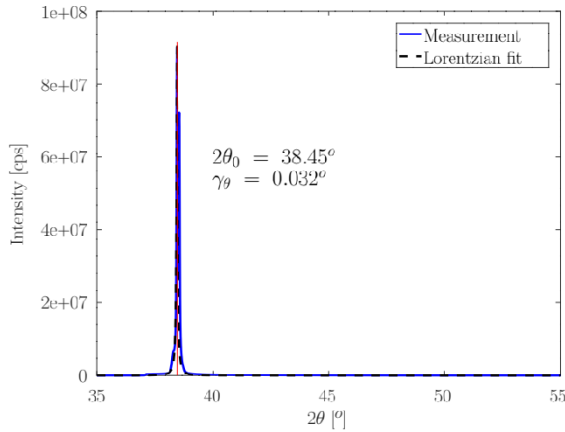
Fig.11. An example of an XRD chart for a precisely oriented Aluminum Crystals in the {1, 1, 1} direction

Next, Fig.12 shows the Rocking Curve peak, with a FWHM of about 0.36 degrees, yet, it should be noted that the RC shape exhibits a minor asymmetry, indicating on some crystalline in-homogeneity. As can be seen in the figure, there is an axial divergence at the lower angles of the peak, causing asymmetry. This asymmetry is an indication of an anisotropic strain.
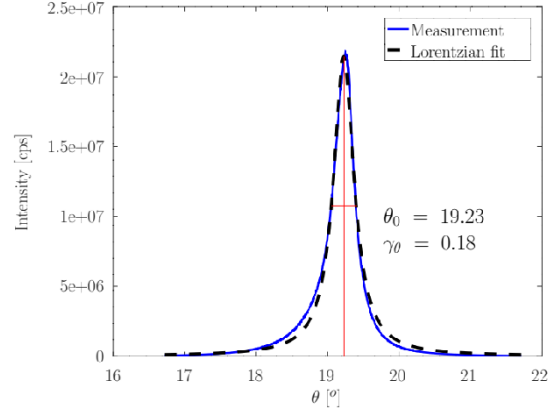
Fig.12. An example of an X-Ray Rocking Curve chart, with a FWHM of about 0.36 degrees and very high peak intensity at the range of 2e7, a slight asymmetry is evident as well

The results were fit using a Lorentz (Cauchy) PDF (probability distribution function), that was found to better fit the results. If we take the Lorentzian's FWHM as a measure of orientation spread of the mosaic structure tilt, we can estimate that it is approximately 0.18°. Following the FWHM angle spread of the tilt angles we can calculate the upper limit of the dislocation density [10].

$$D = \frac{\left(FWHM/2\right)^2}{9b^2} = \frac{\gamma_\theta^2}{9b^2} \qquad (1)$$

where γ_0 is the tilt spread, and b is the Burgers vector. For the aluminum with an FCC structure in the (1,1,1) direction, the Burgers vector is given by

$$b = \frac{a}{2} \cdot \sqrt{\left(h^2 + k^2 + l^2\right)}$$
$$b = \frac{a\sqrt{3}}{2} \qquad (2)$$

where a is the side length of the unit cell. As it is 4.046×10^{-10} m, b = 3.504×10^{-10} m. Thus the upper limit estimate of the dislocation density is

$$D = 8.93 \times 10^{-8} \left[cm^{-2}\right] \qquad (3)$$

which is considered very high usually obtained under stress [11]. Considering the stress within the crystal, we could expect that the stress is non uniform. This was evident by rocking curve mapping resulting in different tilt spreads as can be seen in Fig.13.
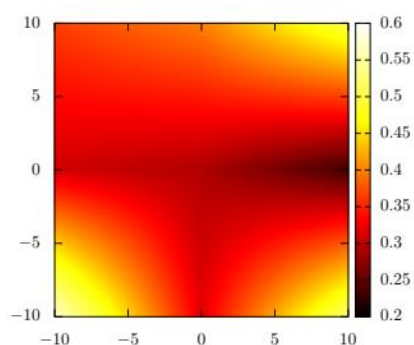
Fig.13. Rocking curve mapping of the tilt spread on a 2x2 cm area from a crystal cross section

As the tilt spread is correlated to the dislocation density which is further correlated to the stress, it shows the non uniform stress within the sample. This must reflect on the peak intensity (counts) as shown in Fig.14.
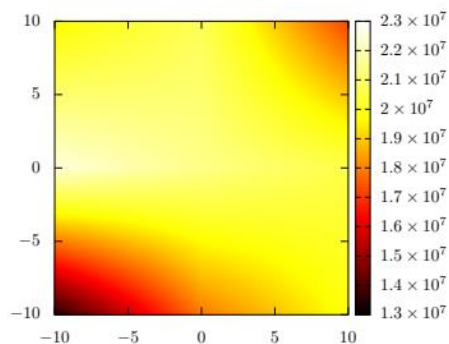
Fig.14. Rocking curve mapping of peak intensity on a 2x2 cm area from a crystal cross section

While the XRD rocking curve angle spread is an average of many low tilt angle subgrains, being macroscopic in nature, the fine structure can be observed using STEM imaging. Fig.15a and 15b, illustrate the STEM results displaying the dislocation defects in a crystal that exhibits sub grain boundaries (low angle) within grains, and tilt boundaries that may significantly differ from each other.
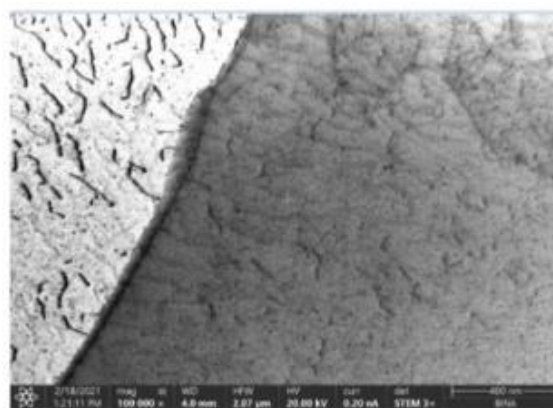
(a)
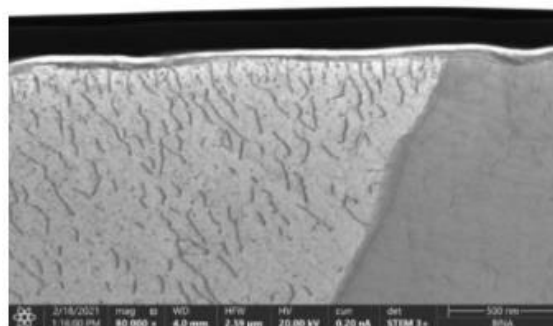
(b)

Fig.15. (a) is a STEM image of an Aluminum crystal with high defect density, reflected at the observed sub grains and dislocation defects. (b) Shows displays the native oxide layer of the surface of the crystal

CONCLUSIONS

X-ray diffraction methods and Rocking-curve analysis, supported by SEM and STEM imaging, were shown to display, in an effective manner the three dimensional crystalline quality of aluminum single crystals. This is demonstrated with both poor and high quality aluminum single crystals grown using the veteran Bridgman method. Growth and fabrication of the crystals were still found to be short of the strived state of the art. It was further demonstrated that sample fabrication by rough electro-erosion cutting, exhibited a membrane like, porous deformed structure at the aluminum as cut surface. Supplementing electrical conductivity measurements of aluminum, quality assessment of defects in front cell aluminum conductors can assist in designing novel low resistance aluminum conductors replacing the currently widely used and relatively rare silver.

REFERENCES

1. Rimma Lapovok, Yaron Amouyal, Yuanshen Qi, Alex Berner, Anna Kosinova, Eugene Lakin, Dmitri A. Molodov, and Emil Zolotoyabko. Enhancement of electrical conductivity in aluminum single crystals by boron treatment in solid state. Journal of Materials Science, 55(6):2564—2577, 2020.

2. Lewis Ricci, Mao-Feng Tseng, Meng Tao, Yunyu Liu, Fangdan Jiang, and Guoqiang Xing. Light-induced Al plating on Si for fabrication of an Ag-free all-Al solar cell. ECS Journal of Solid State Science and Technology, 10(2):025004, 2021.

3. Dimensions solar cells front aluminum metallization, 2021. Accessed: 2021-07-11 https://app.dimensions.ai/discover/publication?search_mode=content&search_text=solar%20cells%20front%20aluminum%20metallization&search_type=kws&search_field=full_search.

4. SK Mohanlal and D. Pathinettam Padiyan. Crystal growth of aluminium by two simple methods. Journal of Physics D: Appplied Physics, 15(2):L11, 1982.

5. S. Zerbib, G. Orr, and G. Golan. Open top seeding crystal growth control system. BULGARIAN CHEMICAL COMMUNICATIONS, page 85, 2020.

6. Sunghwan Jin, Ming Huang, Youngwoo Kwon, Leining Zhang, Bao-Wen Li, Sangjun Oh, Jichen Dong, Da Luo, Mandakini Biswal, Benjamin V Cunning, et al. Colossal grain growth yields single-crystal metal foils by contact-free annealing. Science, 362(6418):1021—1025, 2018.

7. DML Bartholomew and A Hellawell. Changes of growth conditions in the vertical bridgman-stockbarger method for the solidification of aluminum. Journal of Crystal Growth, 50(2):453—460, 1980.

8. Bertram Eugene Warren. X-ray Diffraction. Courier Corporation, 1990.

9. JA Gorman, DS Wood, and T. Vreeland Jr. Mobility of dislocations in aluminum. Journal of Applied Physics, 40(2):833—841, 1969.

10. PBKA Gay, PB Hirsch, and A Kelly. The estimation of dislocation densities in metals from x-ray data. Acta metallurgica, 1(3):315—319, 1953.

11. Hailiang Yu, A Kiet Tieu, Cheng Lu, and Charlie Kong. Abnormally high residual dislocation density in pure aluminum after al/ti/al laminate annealing for seven days. Philosophical magazine letters, 94(11):732—740, 2014.

Modeling the thermal operation of a petroleum coke-calcining unit

H. I. Beloev [1], A. S. Nikiforov[2], I. K. Iliev[1], E. V. Prihodko[2], M. S. Kucherbayev[2]

[1] "Angel Kanchev" University of Ruse, Department of Thermotechnics, hydraulics and Environmental Engineering
[2] Non-profit limited company «Toraighyrov University», Department of Heat Power Engineering, 64 Lomov Str, 140000 Pavlodar, Kazakhstan

The article describes the development of a mathematical model of thermal state of the unit lining for calcining petroleum coke. Determination of the temperature fields of the lining will allow you to control the quality and volume of the resulting technological product, assess heat losses from the surface of the unit to the environment, and observe thermal conditions during start-up operations and shutdowns. To check adequacy of the model, calculations of temperature on the inner surface of lining of the coke calcination furnace were carried out during the heating process. The analysis of the given graphs shows that the developed mathematical model is adequate. On average, difference between thermocouple readings and calculated values does not exceed 5%. Further use of the developed mathematical model will be to create a computational complex for evaluating temperature fields along the entire length of rotary kilns for calcining petroleum coke.

Keywords: Lining, temperature stresses, mathematical model

INTRODUCTION

Improving the thermal performance of the linings of high-temperature units is a very wide range of measures aimed at increasing their energy efficiency. It, in turn, can be broken down into three components:
- rationalization of the lining design;
- the use of new refractory materials;
- improvement of thermal modes of lining operation.

Rationalization of the lining design may imply: a change in the profile of the inner surface of refractories, the thickness of the lining layers, the geometry of the refractory itself, etc.

The change in the profile of the inner surface of the lining is made based on operational data, which analyzes the parts of the lining that are subject to the greatest wear. This can be caused by various reasons - the effect of chemically aggressive slags, metal jets during its discharge, etc. Selection of refractory thicknesses corresponding to their actual operation in a given place of the lining, according to [1], can increase the lining durability by 10-15%.

A change in the thickness of the lining layers, calculated for specific conditions, can lead to a decrease in heat losses by 10-15%. So, in [2], to reduce heat losses, a combined lining was created, consisting of chamotte and additional fibrous heat-insulating material (mullite-silica wool). At the same time, a cell filled with heat-insulating material is formed between the refractory and the furnace body.

Replacing the lining material with another can also be attributed to the rationalization of the design [3-6]. In such cases, the non-load bearing lining layer (usually made of molded refractories) is replaced with an insulating layer of fibrous materials. The use of fibrous materials for the lining of furnaces allows, in comparison with brick lining, to reduce heat losses through the lining by 20-30%, to reduce several times the heating time of the furnace and the duration of installation of the lining, to save energy resources up to 45% with periodic stoppages of the furnaces [7]. Heat treatment of refractory raw materials also has a significant effect [8].

The use of geometrically rational refractories also affects the life of the lining. Classic shapes of molded refractories - straight and wedge bricks are not optimal in terms of uniformity of stress. In this respect, the hexagonal shape of products is more preferable, therefore, products in the form of hexagonal prisms should find application in ferrous metallurgy units [9].

Improving the thermal operation of the lining is undoubtedly the most cost-effective way to improve the thermal operation of the linings. In this case, there is no need to purchase new refractories or to change the design of the unit itself. Initially, each high-temperature unit has thermal schedules for heating up and operating the unit. These charts are "factory" and are usually designed to ensure that the rate of temperature change does not exceed the rates recommended by the manufacturer for lining materials. Naturally, these graphs are general and do not reflect the specifics of the operation of a

---

* To whom all correspondence should be sent:
aleke4599@mail.ru

particular unit. Thus, this does not take into account the thickness and number of lining layers, the presence of cooling, wear of the lining during start-ups from repairs with partial replacement of the lining, etc. , but also to an increase in the working campaign of the units (by reducing the heating time and downtime).

The first stage in improving the thermal operation of the lining will be the creation of a model of the thermal operation of the lining [10, 11].

Modeling the thermal operation of a petroleum coke-calcining unit is reduced to calculating the temperature field inside the furnace during the unit heating up. The problem of determining the temperature fields in the construction of a unit with flat walls and one layer of refractory lining material is widely presented in the literature [12, 13]. Meanwhile, there is a wide range of high-temperature installations for which these developments are not applicable. These are tubular rotary kilns and, in particular, for refinery coke calcination.

From the standpoint of determining the thermal state, these furnaces can be attributed to one group according to the following parameters. They have a considerable length (from 60 to 100 meters) with a diameter of 3 to 5 meters. The inner part of the metal cylindrical body is covered with a layer of refractory material, usually made of refractory bricks. The furnace is installed at an angle of 3 to 5° to the horizon and is capable of rotating at a speed of up to four revolutions per minute. Due to the tilt, the rotation of the furnace facilitates the movement of technology material from the feed end to the discharge end. Rotary kilns work on the principle of counterflow - raw material is fed from one side, and fuel is burned from the opposite. As a result, the gases formed during fuel-burning move towards the flow of material, directly carrying out the heat exchange process.

PROBLEM FORMULATION

As a rule, tubular rotary kilns have an internal surface temperature control sensor - this is a thermocouple installed in the most important (technologically) zone. But the installed thermocouple makes it possible to control only a part of the unit (only one zone) and does not allow controlling the temperature condition of the process material along the entire length of the unit. It is technically difficult to install temperature sensors in each zone.

Determining of temperature fields in the furnace during its operation allows you to have information for solving a number of problems. Firstly, it is the quality of the resulting technological product. Based on the main thermophysical properties of the product (humidity, volatile-matter content, etc.), it is necessary to maintain the calculated thermal condition, which can be controlled by the temperature of lining [14, 15, 16]. Secondly, it is volume of the technological product. When maintaining the optimal thermal condition, the furnace will have not only maximum productivity, but also minimum energy consumption per unit of production [17]. Thirdly, control of temperature state of lining allows not only to estimate temperature losses from surface of unit to the environment, but also to reduce them at the design stage when considering various options for refractory materials for their use in the lining [18, 19]. Fourth, compliance to thermal conditions during operation and shutdowns allows to extend the life of the lining, which leads to significant savings [20, 21, 22]. As a result, control and compliance with thermal conditions during the operation of ring rotary kilns is an important step in the policy of energy saving.

Modern technical means make it possible to conduct a continuous process of monitoring the thermal state of the lining using thermal imaging. This allows to solve a number of the above-mentioned problems: control of the thermal regime and losses from the surface of the high-temperature unit [23]. To solve other problems, a mathematical apparatus is needed that allows calculating temperature fields not only over the thickness of the lining (which is important for stationary processes), but also in time (for non-stationary processes). Installation of a number of temperature sensors for measuring the temperatures of the inner surface of the lining (by zones) is technologically difficult and significantly reduces the reliability of the rotary kiln. As the result, the task is to develop a mathematical apparatus that makes it possible to calculate the temperature fields of the masonry in a stationary and non-stationary mode using the initial temperature data: the temperature of the process material and the outer surface of the lining.

The mathematical treatment of this process is generally represents a system of partial differential equations. What is more, the integration of this system is a difficult task, the solution of which requires special mathematical support and high power of computer facilities.

Consider the thermal state of ring lining of the coke calcination furnace, presented as a long hollow cylinder. The cross section of the furnace (Fig.1) is a double-layer ring. Let us introduce the following assumptions:

- Thermophysical and mechanical properties of each lining layer are different and constant within each layer;

- Temperature of inner surface is taken equal to the temperature of technological material;

- At the boundary between layers - equality of heat current;

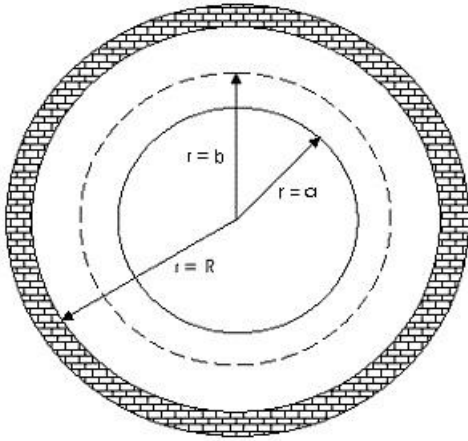- The heat transfer law is set on the outer surface of the furnace body.

Fig.1. Calculation scheme of the furnace lining

METHODOLOGY OF THE RESEARCH PRACTICE

Mathematically, taking into account the accepted assumptions, the problem is formulated in a certain way. Let us write the equation of heat conduction in a cylindrical coordinate system with a radial temperature distribution:

$$\text{for the 1 layer } \frac{\partial T_1}{\partial t} = a_1 \cdot \left(\frac{\partial^2 T_1}{\partial r^2} + \frac{1}{r} \cdot \frac{\partial T_1}{\partial r} \right), \quad (1)$$

$$\text{for the 2 layer } \frac{\partial T_2}{\partial t} = a_2 \cdot \left(\frac{\partial^2 T_2}{\partial r^2} + \frac{1}{r} \cdot \frac{\partial T_2}{\partial r} \right), \quad (2)$$

where

$\dfrac{\partial T}{\partial t}$ – temperature change over time, °C;

$\dfrac{\partial T_2}{\partial r}$ – temperature change along the radius of the furnace, °C.

with initial

$$T(r,t)\big|_{t-0} = T_0 = const \quad (3)$$

and boundary conditions:

provided $r = a$; $\quad t > 0 \quad T_P = T_R \quad (4)$

$$r = b; k_1 \cdot \frac{\partial T_1}{\partial r} = k_2 \cdot \frac{\partial T_2}{\partial r} \quad (5)$$

$$r = R; k \cdot \frac{\partial T}{\partial r} - h \cdot \left(T_{amb} - T \right) = 0 \quad (6)$$

where:

T_P – temperature of the medium in the furnace, °C

T_R – temperature of the inner surface of the furnace, °C

r – furnace lining radius, m;

$r = a$ – inner surface of the lining, m;

$r = b$ – border of lining layers, m;

$r = R$ – outer surface of the lining, m;

k – thermal conductivity of the refractory material, W / (m · K);

h – heat transfer coefficient, W / (m² · K);

T_{amb} – ambient temperature, °C

It is of interest is an algorithm for calculating the temperature field of the lining, involving the use an implicit difference scheme [24, 25, 26], based on the application of the sweep method under boundary conditions on the outer surface of the furnace. This method has several advantages. Firstly, when calculating, the count starts from the outer boundary and, therefore, the computational process can be completed when the temperature at the outer boundary satisfies some condition. As the conditions for using the temperature of the furnace body, obtained by measurements. Secondly, the implicit difference scheme is stable at any time and space steps.

The initial equation for the implicit difference scheme will be:

$$\frac{T_n^{k+1} - T_n^k}{\Delta t} = \frac{a \left(T_{n-1}^{k+1} - 2T_n^{k+1} + T_{n+1}^{k+1} \right)}{(\Delta x)^2} \quad (7)$$

where:

Δx – coordinate step, m;

Δt – time step, s;

a_t – temperature conductivity coefficient, m²/s;

T_n^{k+1} – lining temperature at a point along coordinate n at time k+1, °C.

Transform this equation as follows:

$$-h^2 \cdot T_i^k = a\Delta t T_{i-1}^{k+1} - (2a\Delta t + h^2) \cdot T_i^{k+1} + a\Delta t T_i^{k+1},$$
(8)

$$-T_i^k = \frac{a\Delta t}{h^2} \cdot T_{i-1}^{k+1} - \left(\frac{2a\Delta t}{h^2} + 1\right) \cdot T_i^{k+1} + \frac{a\Delta t}{h^2} \cdot T_{i+1}^{k+1}$$

Set $A = B = \dfrac{a\Delta t}{h^2}$ and C=1+2A, then the equation (16) will be

$$-T_1^k = AT_{i-1}^{k+1} - CT_i^{k+1} + BT_{i+1}^{k+1}$$
(9)

The sweep formulas, in this case, will be represented by the ratios:

$$T_i^{k+1} = \gamma_{i+1} \cdot T_{i+1}^{k+1} + \beta_{i+1}$$
(10)

$$\gamma_{i+1} = \frac{A}{C - \gamma_1 A}$$
(11)

$$\beta_{i+1} = \frac{A\beta_i + T_i^k}{C - \gamma_i A}$$
(12)

$$\gamma_1 = 0, \ \beta_1 = T_n$$
(13)

The temperature value T_{i+1}^{k+1} is found from the boundary conditions at the outer boundary.

EXPERIMENT ANALYSIS

To check the adequacy of the model, the temperature was calculated on the inner surface of the coke calcining furnace during the heating process.

Calcining petroleum coke is the process of heating crude petroleum coke to 1250÷1350°C. At the same time, in the entire mass of coke, processes of structural change occur with the removal of hydrogen, which is released in the form of methane and other hydrocarbon compounds and burns in calcining and afterburning furnaces. The main goal of the calcining process is to improve the physical and chemical properties of coke, such as electrical resistance, true density, oxidizability and reactivity, as a result, the product acquires the necessary qualities.

Coke is calcined in a rotary kiln 65 m long and 3.47 m in diameter, which is installed at an angle of 4° to the horizon and is capable of rotating at a speed of up to two revolutions per minute. Combustion of volatile substances and fuel (fuel oil) during the calcination of petroleum coke produces a large amount of high-temperature flue gases that contain volatiles and a small proportion of fine coke particles. 50-60% of volatiles are burned in the calcining furnace, the rest enter the afterburner together with flue gases. After water evaporation and removal of volatile components, the coke is heated to 1350 °C. Moreover, its molecular structure takes on a more organized form with a clear crystal lattice. In response to the physical and chemical processes occurring with the raw material, the consumer properties of coke are improved. The time of the complete coke calcination cycle from loading to unloading is at least 45 minutes.

In accordance with the developed mathematical model, the temperature calculated over the lining cross-section during the heating process. Fig.2 shows graphs of heating at characteristic points along the cross-section of the lining during the first 24 hours: on the inner surface, in the middle and on the outer surface of the lining.
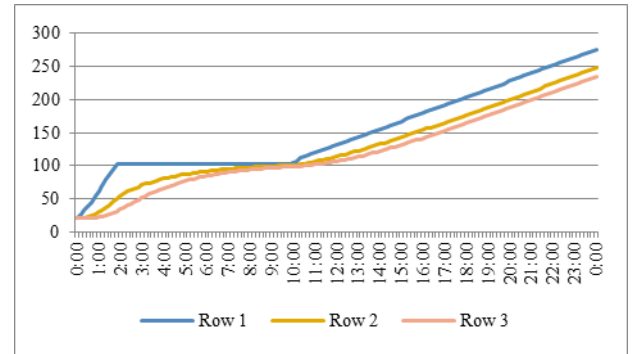
Fig.2. Graphs of heating at characteristic points along the section of the lining in: row 1 - on the inner surface, row 2 - in the middle, row 3 - on the outer surface of the lining

The analysis of the graphs obtained shows that the heating process during the first one hour and forty minutes proceeds at a high speed, which reflects the change in the temperature of the inner surface. High heating rates across the lining thickness begin at fifty minutes (for the middle of the lining) and one hour and forty minutes for the outer surface. Horizontal section of the heating curve, corresponding to a temperature of about 110°C, is necessary to remove moisture from the

lining. At a constant heating rate of the lining by the time 9 h 10 min, we have an almost stationary temperature field.

To check the adequacy of mathematical model and calculations performed, a graph of the dependence of temperature inner surface of the lining on time was built. The obtained values for temperature of the inner surface for comparison with the actual temperature of the surface are shown in Fig.3.

The heating-up schedule of the furnace after major overhaul (heating section up to 500 °C) is shown in Fig.3. Row 1 - a graph based on the readout of a thermocouple installed in the furnace lining, row 2 - a graph based on the results of calculations based on the developed mathematical model.
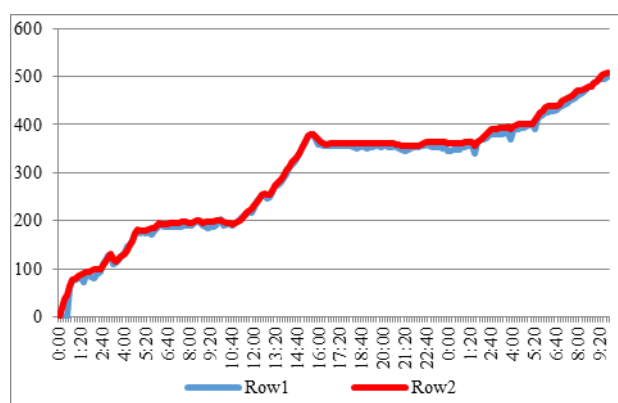
Fig.3. Graphs of heating the furnace after major overhaul

The analysis of the given graphs shows that the developed mathematical model is adequate. On average, the difference between the thermocouple readouts and the calculated values does not exceed 5%. Large values of the difference between the readings of the two graphs, as a rule, to areas of a sharp increase or decrease in temperature. This can be explained by the delayed action of the temperature measurement process.

The developed mathematical model makes it possible to calculate the temperature fields of the masonry in a stationary and non-stationary mode using the temperature of the technological material and the outer surface of the lining. Using the developed technique, it is possible to obtain the temperature distribution over the lining cross section during the heating of any zone of the furnace, while the initial data for the calculation will be the temperatures indicated above. Measuring the temperature of the outer surface of the furnace is not technically difficult - it can be

measured by direct measurement with the installation of a sensor between the steel body and the lining. Also, this temperature can be equated to the temperature of the metal body (taking into account the high thermal conductivity of steel), and the temperature of the body metal can be measured in a non-contact way (pyrometer, thermal imager).

It remains important to determine temperature of the inner surface, or temperature of the technological material in this zone. Technically, not every zone can accommodate a temperature sensor to measure the parameters of the inner surface. The thermocouple port, which runs through the entire lining, is a hazard at high process material temperatures due to possible leakage and material escaping through the sensor port.

Taking temperature of the process material, focusing only on finding it in a specific zone of the furnace, can lead to high calculation errors. This is due to the fact that within one zone of the furnace, the temperature of the process material can change by $300 \div 400$ °C.

To increase the accuracy of calculating temperatures, it is proposed to use a method for determining the thermal state of the lining, which allows, by taking temperature readings from partially buried temperature sensors, to obtain the temperature distribution in the lining section according to the developed mathematical model.

The lining of the high-temperature unit is a wall consisting of a casing 1 and a layer of heat-insulating (or refractory) material 2 (Fig.4). Unit lining contains a temperature sensor 3 at a distance L1 from its inner surface and a temperature sensor 4 at a distance L2 from its inner surface. Inside the heating unit there is a working medium with a temperature T_o. Outside, the ambient temperature is T_{oc}.
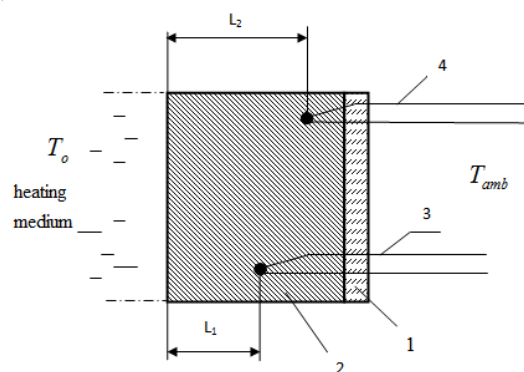
T_o – heating medium temperature, °C; T_{amb} – ambient temperature, °C; 1 – the unit's cover; 2 – refractory material; 3, 4 - thermocouples
Fig.4. Implementation diagram of the method for determining the thermal state of the lining

In the process of laying lining of thermal units, temperature sensors are installed in the lining at specified distances from its inner surface. The number of sensors and the distance from the inner surface are selected based on operational limitations associated with the possibility of emergency situations (leakage, etc.).

From the moment the heating unit starts heating (τ_0), the heating time is counted. For calculations, the step along the Δy coordinate is determined, that is, distance between two nearest points of heating unit lining, at which the temperatures will be determined. Why geometrically divide the wall lining by thickness into such a number of equal sections so that the temperature measurement points by sensors 3 and 4 fall on boundaries of sections between two nearest points of coordinate step.

Then the time step $\Delta\tau$ is determined, that is, the time interval after which the temperatures will be determined over the lining cross section at the selected points.

To determine the temperature fields of the lining of an industrial unit at time τ_1 in the process of non-stationary thermal conductivity, temperature readings are taken by temperature sensors 3 and 4 (T_3 and T_4, respectively).

Further, they are initially set by the temperature of the heating medium T_o. The initial value of this temperature is taken as the lowest possible (under the given heating conditions). Then, the temperature values are calculated over the lining section of thermal unit for the time point τ_1 according to proposed mathematical model.

If at the considered moment of time, calculated temperature at a point at a distance L_1 from the inner surface of lining turns out to be equal to T_3 and the temperature at a point at a distance L_2 from inner surface of lining is equal to T_4, then the calculation is stopped. In this case, the obtained temperature distribution over the lining cross section will be the desired one.

If this condition is not met, set a different temperature T_o and repeat the calculation again.

The more temperature sensors are located along thickness of lining, the smaller error in determining temperature field. The minimum number of temperature sensors is dictated by operational limitations associated with the possibility of emergencies.

As a result, the use of this method will increase the accuracy of calculating the temperature distribution over the lining cross section for developed mathematical model. In this case, only the installation of partially recessed temperature sensors in various zones of the furnace is additionally required.

Approbation of the method for determining the thermal state of the lining on a physical model in laboratory conditions has shown that the mathematical model can be applied in practice. (Fig.5).

The laboratory research facility consists of a muffle furnace without a door in which the investigated refractory material is placed instead of that furnace door. Two thermocouples are placed in the refractory according to the above procedure. A secondary device is used to measure and record the temperatures of the refractory and the environment. Thus, the material heated on one side by the heat space of the furnace and cooled by the environment on the other side is a physical model of the wall of the high-temperature unit.

To increase the accuracy of calculations in the study of refractories from working units, the values of the thermal conductivity coefficient were used, taking into account the impregnation of refractories with a working medium [27].

Fig.5. Approbation of the method for determining the thermal state of the lining on a physical model in laboratory conditions

The studies carried out show that the error in determining the temperature over the cross section of the lining during heating in accordance with the method for determining the thermal state of the lining does not exceed 10% [28], which indicates the possibility of using these developments in industrial conditions.

CONCLUSION

A mathematical model of the thermal state of a high-temperature unit has been developed, which

makes it possible to control the internal temperature of the furnace, both in the heating mode and in the operation mode. Approbation of the technique during the heating of the coke calcination unit allows us to speak about the sufficient reliability of the data obtained.

The use of this mathematical model makes it possible to control technological processes during the processing of the initial raw material in the furnace, avoiding excess energy consumption.

Further use of the developed mathematical model will be to create a computational complex for assessing temperature fields along the entire length of rotary kilns for calcining petroleum coke.

REFERENCES

1. D.V. Koryukov, V.V. Levchuk, A.A. Metelkin, O.Yu Sheshukov, I.V. Nekrasov, L.A., Marshuk, Methods of increasing the durability and reliability of the lining of vacuum chambers in OJSC "NTMK", *Theory and technology of metallurgical production*, pp.48-51 (2010).

2. A.A. Markus, Simulation of thermal processes in tubular rotary sintering furnaces. Abstract of a dissertation for the degree of candidate of technical sciences. National University of Mineral Resources Saint Petersburg (2014).

3. Kuo Lin, Zhongjie Shen, Qinfeng Liang, Jianliang Xu, Haifeng Liu, Modelling study of characteristics of heat transfer and structural optimization of refractory layer in an entrained-flow gasifier, *Applied Thermal Engineering*, Volume **168**, 114830, (2020), https://doi.org/10.1016/j.applthermaleng.2019.114830.

4. Bo Ren, Yawei Li, Mithun Nath, Qinghu Wang, Yibiao Xu, Enhanced alkali vapor attack resistance of bauxite-SiC refractories for the working lining of cement rotary kilns via incorporation of andalusite, *Ceramics International*, Volume **44** (18), pp. 22113-22120, (2018), ,https://doi.org/10.1016/j.ceramint.2018.08.323.doi.org/10.1016/j.ceramint.2018.08.323.

5. Shuang Shi, Pengting Li, Zhilin Sheng, Dachuan Jiang, Yi Tan, Dengke Wang, Shutao Wen, H.M. Noor ul Huda Khan Asghar. Energy efficiency improvement in electron beam purification of silicon by using graphite lining, *Energy*, Volume **185**, pp. 102-110, (2019), https://doi.org/10.1016/j.energy.2019.07.038.

6. Wen Yan, Guiyuan Wu, Sanbao Ma, Stefan Schafföner, Yajie Dai, Zhe Chen, Jiangtao Qi, Nan Li. Energy efficient lightweight periclase-magnesium alumina spinel castables containing porous aggregates for the working lining of steel ladles. J. of the European Ceramic Society. Volume **38**, Issue 12. pp. 4276-4282, (2018), https://doi.org/10.1016/j.jeurceramsoc.2018.05.002.

7. D.V. Mendelev, Application of energy-efficient lining designs to reduce fuel consumption in industrial furnaces / D. V. Mendelev, I. A. Trusova, P. E. Ratnikov // *Casting and metallurgy: scientific and production journal*, № **2** (65), pp. 108 – 112, (2012).

8. Yichong Li, Huizhong Zhao, Yang Yang, Zecheng Feng, Han Zhang, Jun Yu, Yanli Liu, Li Feng. The restructuring-sintering mechanism of calcium alumino-titanate in tundish permanent lining castables. *Ceramics International*. Volume **46**, Issue 18, Part A. pp. 29282-29289, (2020). https://doi.org/10.1016/j.ceramint.2020.08.102.

9. K. K. Strelov, I. D. Kascheev, D.S. Rutman, I.I. Nemets, L.B. Romanovsky, Refractory protection // *Refractories*, №**8**. pp. 48-52 (1983).

10. I. Istadi, Y. Bindar Improved cooler design of electric arc furnace refractory in mining industry using thermal analysis modeling and simulation. *Appl. Thermal Engineering* **73** (1) pp. 1129-1140, (2014), https://doi.org/10.1016/j.applthermaleng.2014.08.070.

11. Huining Zhang, Peiling Zhou, Fei Yuan. Effects of ladle lid or online preheating on heat preservation of ladle linings and temperature drop of molten steel. *Energy*. Vol. **214**. (2021), https://doi.org/10.1016/j.energy.2020.118896.

12. A. S. Afanasiev, A. V. Borodulin, I. Sultanguzin, S. N. Yarunin, & A. Yashin Energy analysis of thermal operation of coke-oven batteries. *Solid Fuel Chemistry*. **37**(1):62 – 69, (2003).

13. M.Emre Ertem, Abdulkadir Özdabak, Energy balance application for Erdemir Coke Plant with thermal camera measurements, *Applied Thermal Engineering*, Vol. **25**(2–3), pp. 423-433. (2005).

14. K. Pourabdollah, MS Zakaria, SMM Najafizadeh. Optimization of operating conditions in desulfurization of petroleum coke using induction heating. Asia-Pac *J Chem Eng*., Vol. 15, (1) (2020); https://doi.org/10.1002/apj.2398.

15. Bin Zheng, Yongqi Liu, Lichen Zou, Ruiyang Li, "Heat Transfer Characteristics of Calcined Petroleum Coke in Waste Heat Recovery Process", *Mathematical Problems in Engineering*, vol. **2016**, Article ID 2649383, (2016). https://doi.org/10.1155/2016/2649383.

16. M. Bernd. et al. "Synthesis of carbon nanostructures by the pyrolysis of wood sawdust in a tubular reactor, *Journal of materials research and technology* **6** pp.171-177 (2017).

17. M. M. Akhmetov. Petroleum coke calcination processes — present and future. *Chem Technol Fuels Oils* **22**, pp. 321–333 (1986). https://doi.org/10.1007/BF00730517.

18. I. I. Lapaev, V. V. Sorokin, S. E. Goloskin et al. Lining of the Rotary Kilns for Petroleum Coke Calcination. *Refract Ind Ceram* **60** (1–5) (2019). https://doi.org/10.1007/s11148-019-00299-w.

19. Fabrice Patisson, Etienne Lebas, François Hanrot, Denis Ablitzer, Jean-Leon Houzelot. Coal pyrolysisin a rotary kiln: Part II. Overall model of the furnace. *Metallurgical and Materials Transactions* B,Springer Verlag, **2**,31, pp. 391-402 (2000),. https://doi: 10.1007/s11663-000-0057-4.

20. E. Brochen, J. Pötschke and C. G. Aneziris, Improved Thermal Stress Resistance Parameters Considering Temperature Gradients for Bricks in Refractory Linings. *Int. J. Appl. Ceram. Technol.*, **11**: pp. 371-383, (2014) https://doi.org/10.1111/ijac.12022.

21. A. K. Akishev, S. M. Fomenko & S. Tolendiuly. Effect of Refractory Thermal Stresses and Parameters on Development of the Internal Temperature Field. *Refract Ind Ceram* **60**, pp. 561–565 (2020). https://doi.org/10.1007/s11148-020-00407-1.

22. V. O. Sinelnikov, D. Kalisz & R. D. Kuzemko. Study of the Phase and Mineralogical Properties of Converter Slag during Splashing to Improve Lining Resistance. *Refract Ind Ceram* **59**, pp. 403–409 (2018). https://doi.org/10.1007/s11148-018-0244-y.

23. Y.V. Sharikov. Control system of the roasting process in tubular rotary kilns using thermal imaging scanning / Y.V. Sharikov, T.O. Koyranen. *Notes of the Mining Institute*. Vol.221, pp.681-687 (2016). https://doi10.18454/ PMI.2016.5.681.

24. A. S. Nikiforov, E. V. Prikhod'ko. Thermal Stresses Generated in the Lining of a Steel Ladle. *Refract Ind Ceram* **46**, pp. 360–363 (2005). https://doi.org/10.1007/s11148-006-0012-2.

25. Bowen Luo, Gongfa Li, Jianyi Kong, Guozhang Jiang, Ying Sun, Ze Liu, Wenjun Chang, Honghai Liu.. Simulation Analysis of Temperature Field and Its Influence Factors of the New Structure Ladle. *Applied Mathematics & Information Sciences*. **11**. pp. 589-599 (2017), DOI: 10.18576/amis/110231.

26. Nikiforov A. S., Prikhod'ko E. V., Kinzhibekova A.K., Kucher E.O., Niconov G.N. Method for determination of thermal state of fettling of heating unit. KZ26932-A4, 15 May (2013), G01K-013/00.

27. Nikiforov A. S., Prikhod'ko E. V., Kinzhibekova A. K., Karmanov A. E. Investigation of the Dependence of Refractory Thermal Conductivity on Impregnation with a Corrosive Medium. Refractories and Industrial Ceramics, Vol. 60, No. 5. Pp. 463- 467. January, 2020; doi:10.1007/s11148-020-00386-3.

28. Prikhodko E. V. Development of a method for monitoring the process of heating the lining of high-temperature units, *J. Sib. Fed. Univ. Eng. & Technol.*, **13**(4), pp. 462-472, (2020), DOI: 10.17516/1999-494X-0233.

Novel flue gases waste heat recovery methodology avoiding wet gas cleaning technologies in thermal power plants

I. K. Iliev[1*], H. I. Beloev[1], A. K. Terziev[2], A. G. Georgiev[3,4]

[1]*University of Ruse, Department of Thermotechnics, Hydraulics and Environmental Engineering, 8 Studentska Str., 7017 Ruse, Bulgaria*

[2] *Technical University of Sofia, Dept. of Power Engineering and Power Machines,8 Kliment Ohridski blvd., 1000 Sofia, Bulgaria*

[3]*Technical University of Sofia, Plovdiv Branch, Dept. of Mechanics,25 Tsanko Diustabanov Str, 4000 Plovdiv, Bulgaria*

[4]*Institute of Chemical Engineering at the Bulgarian Academy of Sciences, Acad. G. Bonchev Str. Bl.103, Sofia 1113, Bulgaria*

Flue gases waste heat recovery of coal-fired power plants is associated with lowering their temperature to values significantly above the dew point, because acid deposition leads to corrosion of the affected heating surfaces. When wet gas cleaning technologies are used, additional heat is lost to heat the purified gases with hot air before they enter the stack. The proposed innovative method provides for a more complete use of thermal energy of exhaust gases and eliminates the need for additional reheating of the wet gases before entering the stack. This can be achieved by directing a portion of the gas stream to a bag filter in which there is slight reduction of the flue gas temperature and then mixing this portion with the main stream passing via the economizer or air preheater in a pre-existing mixing chamber to achieve the desired humidity and temperature of flue gases. A technical and economic assessment of the expediency of utilizing the waste heat from the flue gases by means of an economizer or an air preheater of several different coal-fired steam generators which are using purification technology with battery emulsifiers has been made - the boiler BKZ-160-100F in Almaty CHP-3 has an indisputable advantage.

Keywords: Waste heat recovery, flue gases, feasibility study, battery emulsifier second generation, bag filters

INTRODUCTION

Waste heat recovery leads to a reduction of the total losses of the steam generator and increases its thermodynamic efficiency [1]. Sometimes however, the possibilities for lowering the temperature of the exhaust gases are accomplished by the respective gas purification methods [2]. In some countries of Asia, incl. Russia and Kazakhstan, wet gas purification methods have become very popular [3]. The reason for this is the lack of policy for the recovery of collected ash after electrical precipitators and further sale as a building material [4]. The study reveals that the ash together with suitable hydraulic binders forms building materials with maximum operational temperature up to 1150 °C. The properties of the produced by the coals ash is studied in [5]. The main output from the analysis shows that mechanical strength of the cyclone ash is reduced in comparison with the ash collected with the electrostatic precipitator. The similar study [6] also confirm that the ash from electrostatic precipitator has the necessary strength to produce the construction materials in steel and chemical industry.

In terms of the ensuring the environmental safety of the coal fired TPP different flue gas purifications systems have been examined. In [7] the simulation process of the wet cleaning system is proposed. Focus of the study is by controlling the operational parameters to reduce the environmental impact and improve the energy efficiency. Certain numbers of TPP have been equipped with the electric filter systems for dry-wet purification of the stack gases [8]. The study shows that in about 60% is the efficiency of the system.

In the European Union, where gases are mainly cleaned by electrical precipitators, 80% of the waste ash is sold and this increases the economic feasibility of using this type of gas purification [9]. Different systems related with processing of coal deposits are also available. Within the range of the proposed system the mutual impact on the usage of wet and dry-cleaning technologies, organization of fuel combustion, and using the different types of filters to clean flue gases from impurities could significantly improve the efficiency of the plant. The main idea also from the study is to be utilized the spent TPP lubricants in the power plant cycle.

The use of ashes in construction began in the 30s of the last century in the manufacture of bricks and cinder blocks. Strategically important objects

---

* To whom all correspondence should be sent:
iiliev@enconservices.com

built with the use of ashes include the Tallinn TV Tower and the Sankt Petersburg Nuclear Power Plant. Among the latest sites also constructed using ashes are the cargo port in Helsinki (Finland) and the port of Trondheim (Norway) [10]. Ashes are also applied in a variety of areas: in road construction (in the construction of subgrade, for the construction of fortified foundations and embankments); soil stabilisation measures: strengthening weak soils, as an additive to binders in order to save them when strengthening soils; in asphalt-cement concrete (as a filler and mineral powder in asphalt concrete; for hydrotechnical embankments, etc.).

In recent years, second-generation battery emulsifiers have been widely used in many thermal power plants in Kazakhstan, using mainly Ekibastuz coal [11, 12]. The principle of operation of the second generation battery emulsifiers is a highly efficient heat and mass transfer between the ascending flow of flue gas swirled in the blades and the liquid supplied by the counterflow with the formation of a vortex emulsion layer, in which effective gas cleaning takes place (the so-called phase inversion mode) [13, 16, 17].

Based on the performed literature overview, it is quite clear that scientific studies in this area are limited where a combination of innovative waste heat recovery method, comprising a combination of an additional air preheater and a bag filter, or alternatively an additional economizer and a bag filter should be examined [14, 15].

The present paper proposed innovative waste heat recovery method, comprising a combination of an additional air preheater and a bag filter, or alternatively an additional economizer and a bag filter. Several novelties based on the study done are available:

- opportunity to use the useful temperature drop of the flue gases, whereby part of the hot gases are purified with higher efficiency in a bag filter and then mixed with the wet gases after the existing emulsifier, without the need for hot air from the boiler air preheater;
- a technical and financial analysis showing the feasibility of the implementation of waste heat recovery units (WHRU);
- presentation of several variants of WHRU characterized by an attractive low Payback period (2.77 - 6.78 years);
- high environmental impact presented for example with the reduction of the Ekibaztuz coal, depending on the selected boilers.

Determination of the allowable temperature of the exhaust gases after economizer or air preheater

The technical and economic analysis is made for waste heat recovery from different type of boilers using Ekibastuz coal. There are two alternatives: installing an additional economizer or using an air preheater in front of the existing battery emulsifier. However, which of the two possible options to choose should determine the allowable level of cooling of the exhaust gases in order to avoid low-temperature corrosion on the non-heated surfaces of the heat exchangers [13, 18, 19].

The elemental composition and calorific value of coal are presented in Tab.1. It should also be noted that the price of coal varies from region to region, which affects the payback period for waste heat recovery facilities.

Table 1. The elemental composition and calorific value of Ekibastuz coal [3, 12]

Rank	units	value
Carbon, C^r	%	46.03
Hydrogen, H^r	%	2.85
Nitrogen, N^r	%	0.86
Oxygen, O^r	%	6.56
Sulphur, S^r	%	0.70
Water, W^r	%	5.0
Ash, A^r	%	38.0
HHV	kJ/kg	16 493

With sufficient accuracy for practice, the theoretical dew point temperature can be determined by equation (1) [1]:

$$t_{dp}^t = \Delta t_{dp}^t + t_{dp}^{H_2O}, \ ^0C \qquad (1)$$

where:

$t_{dp}^t, \ ^0C$ – the theoretical temperature difference between the acid dew point of the gases and the condensation temperature of the water vapor;

$t_{dp}^{H_2O}, \ ^0C$ – dew point temperature of pure water vapor [1, 21];

$$\Delta t_{dp}^t = \frac{200 \cdot \sqrt[3]{S_{rel}^r}}{1.25^{a \cdot A_{rel}^r}}, \ ^0C \qquad (2)$$

where

a - share of what was taken away with the ashes, -;

S^r_{rel} and A^r_{rel} - reduced sulfur and ash contents relative to 1000 kJ/kg of fuel oil heat, %.kg/MJ [1, 23].

Following these formulas (1 and 2) for the selected base fuel according to Table 1 the theoretical dew point is obtained: $t^t_{dp} = 84.0, {}^0C$.

Complete exclusion of low-temperature corrosion for air preheaters or economizers is provided if the temperature of the wall of the coldest section is higher than the dew point temperature by not less than 5÷10°C (minimum temperatures refer to minimum loads) [13].

In the present analysis it is accepted that the temperature to which the gases in the utilization facility will be cooled down to is 120÷125°C. At this temperature, the gases will enter the emulsifier.

It should be noted that in emulsifiers, almost complete trapping of sulfuric anhydride occurs. This means that the dew point of sulfuric acid vapors contained in the flue gases t^t_{dp} after entering the emulsifiers approaches the dew point of water vapor itself. Therefore it is not required to determine said temperature before the emulsifier stage [24].

THE ESSENCE OF THE INNOVATIVE METHOD FOR WASTE HEAT UTILIZATION

Baseline (current situation)

Most of the TPPs under analysis are characterized by high exhaust gas temperatures (150÷180 °C), leading to large heat losses with the exhaust gases and respectively low efficiency of the steam generator. A characteristic feature of steam generators is that the purification of gases is carried out by battery emulsifiers of the second generation and they are used in almost all thermal power plants, except for those in which first generation emulsifiers or even scrubbers are still in operation [2]. To prevent corrosion of the gas path, the purified gases at the outlet are heated by adding hot air to them after the boiler air preheater. After heating, the purified gases are sent through the outlet flue to the suction of the flue and then into the stack. The existing gas purification system not only does not allow the utilization of waste heat from the gases, but leads to a further reduction in the efficiency of the steam generator by about 3-4%. In Fig.1 shows a schematic diagram of the gas path after the steam generator with a battery emulsifier.
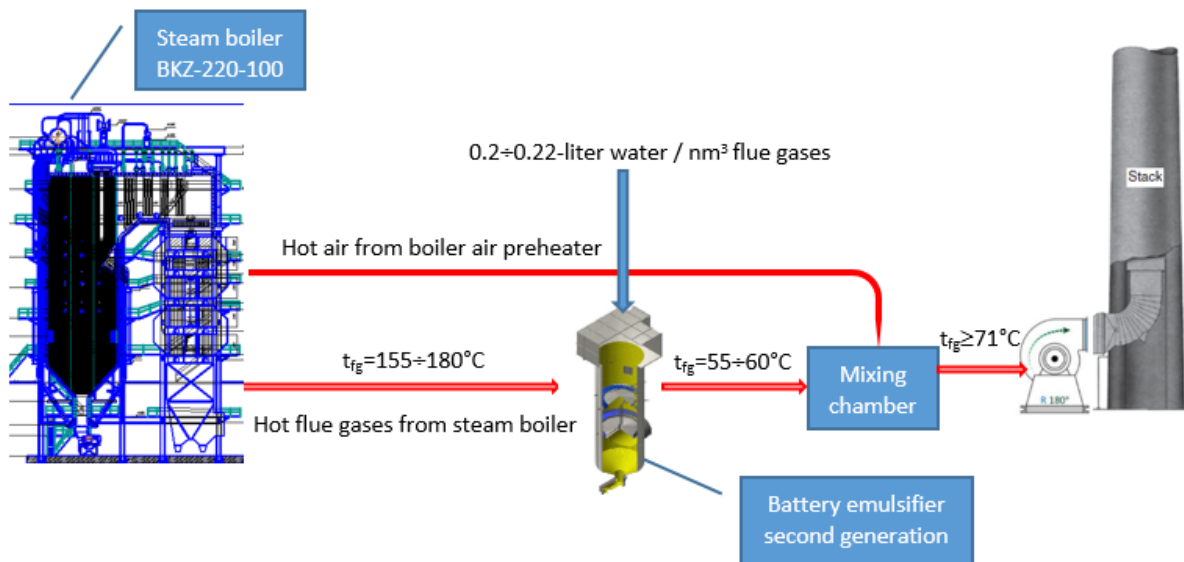
Fig.1. Schematic diagram of the gas path after the steam generator with a battery emulsifier

Description of the proposed method for heat waste recovery

The proposed method to improve energy efficiency provides for a more complete use of thermal energy of flue gases and the elimination of the need for additional heating in front of the stack.

This can be achieved by directing a portion of the gas stream into a bag filter, which does not significantly reduce their temperature, and then mixing this portion with the main stream in the existing mixing chamber to achieve the desired overall temperature. The aerodynamic resistance of the bag filter, which will be connected in parallel

with the emulsifier, (140÷170 mm h.c.) does not differ from the resistance of the battery emulsifier, which will allow using the existing exhauster without changes.

Moreover, such a scheme also allows deeper heat recovery from the main flue gas stream using an additional air preheater or economizer. Accordingly, two options for the implementation of this event are proposed:

1. Installation of a bag filter and an air preheater;

2. Installation of a bag filter and economizer.

Thus, several positive effects are simultaneously achieved:

• energy consumption for heating flue gases with hot air is eliminated;

• part of the heat energy of flue gases is utilized;

• deeper cleaning of gases from ash is carried out;

• emulsifiers are unloaded, the volume of flush water directed to the ash dump is reduced, which reduces the load on the emulsifier and flush water pumps and theoretically makes it possible to reduce their power consumption (for example, by installing a frequency control when it is economically justified by the current prices and tariffs);

• If there is market demand and economically viable transportation opportunities, baghouse ash can be sold for use in construction, agriculture or other industries.

After installing the bag filter, as a result of eliminating the need for heating the exhaust gases

with air and saving significant heat output, the annual coal consumption will decrease. At the same time, the level of cleaning of the total the volume of gases from ash will be increased by about approximately 15%.

We will consider the two possible variants of the method implementation:

Option 1: Bag filter and air preheater installation:

This version of measures to improve energy efficiency provides for the installation of an air preheater simultaneously with the installation of a bag filter. However, only part of the gases (about 85% of the volume) must pass through the air preheater and emulsifier, and the rest will enter the bag filter in parallel flow. The thermal power of the air preheater is calculated at an average load of all analysed boilers. In the air preheater, the exhaust gases will be cooled from 150÷180 to 120÷125 °C depending on the flue gas temperature, and the air entering the air preheater will be heated from ambient temperature to a certain value. The sulfuric acid dew point, calculated according to the standard method, is 83.4°C, while the calculated temperature on the surface of the wall of the air preheater pipe will be 110 °C, which guarantees the absence of corrosion during the operation of the air preheater even in winter modes. In Fig.2 a diagram of the gas path after installation of a bag filter and an air preheater is shown.
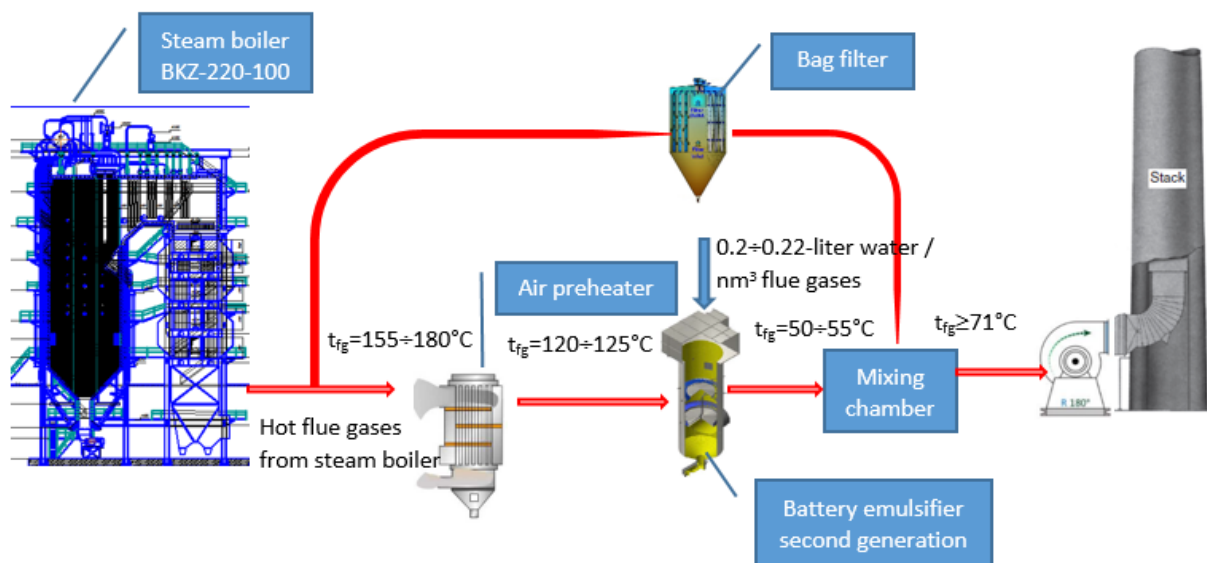

Fig.2. Diagram of the gas path after installation of a bag filter and an air preheater

After cooling the exhaust gases passing through the air preheater, they are purified in the existing emulsifier, in which the temperature of the gases

will decrease even more, and the relative humidity will increase to 100%. The rest of the hot gases (about 15% of the volume, depending of the initial

flue gas temperature), which pass through the bag filters, after deeper cleaning from $35 \div 50$ g / m^3 to $25 \div 35$ mg / m^3 will be mixed with the rest of the gas volume in front of the chimney. Despite the fact that the temperature of the main gas stream after cleaning in the emulsifier decreases to $50 \div 60$ °C, due to the rather high temperature of the gases after the bag filter (about 5 °C temperature drop), the mixed flow will reach the required temperature of $70 \div 72$ °C.

As a result of the installation of the air preheater, the annual coal consumption will decrease significantly. The total fuel savings as a result of the implementation of this energy-saving option will be $2800 \div 7800$ t / year, and the boiler efficiency will increase by $1.5 \div 3.7\%$.

The implementation of this version of energy efficiency measures will lead to an annual reduction in emissions of sulphur dioxide, nitrogen oxides, dust and ash, carbon dioxide, as well as ash and slag waste storage which values have been calculated for considered cases.

Option 2: Back filter and economizer installation.

This option of measures to improve energy efficiency provides for the installation of an additional economizer simultaneously with the installation of a bag filter. Only part of the gas flow (~85%) should pass through the economizer and

emulsifier, and the rest (about 15%) will enter the baghouse filter in parallel flow. A smaller part of the gases passing through the bag filter, after deeper cleaning, will be mixed with the rest of the gas volume. Despite the fact that after cleaning in the emulsifier, the relative humidity of the main gas stream will increase to 100%, and its temperature will drop to 50-60 °C, due to the rather high temperature of the gases after the bag filter, the mixed gases before entering the chimney reach the required 70÷72° C. Fig.3 shows a diagram of the gas path after installation of a bag filter and economizer.

In the economizer in front of the emulsifier, the exhaust gases will be cooled from initial flue gas temperature down to $120 \div 125$°C, and the water flow from the return heating network entering the economizer will be heated from 55°C to a certain value depending on the water flow. The heat output of the economizer is calculated at an average boiler load. As a result of installing an economizer, annual coal consumption will decrease by $1800 \div 2200$ tons. Unlike the previous version with an air preheater, installing an economizer will lead to a slight increase in electricity consumption for water pumps. However, the total fuel savings as a result of energy saving measures will amount to $2,800 \div 7,800$ t / year, and the boiler efficiency will increase by the same $1.5 \div 3.7\%$.
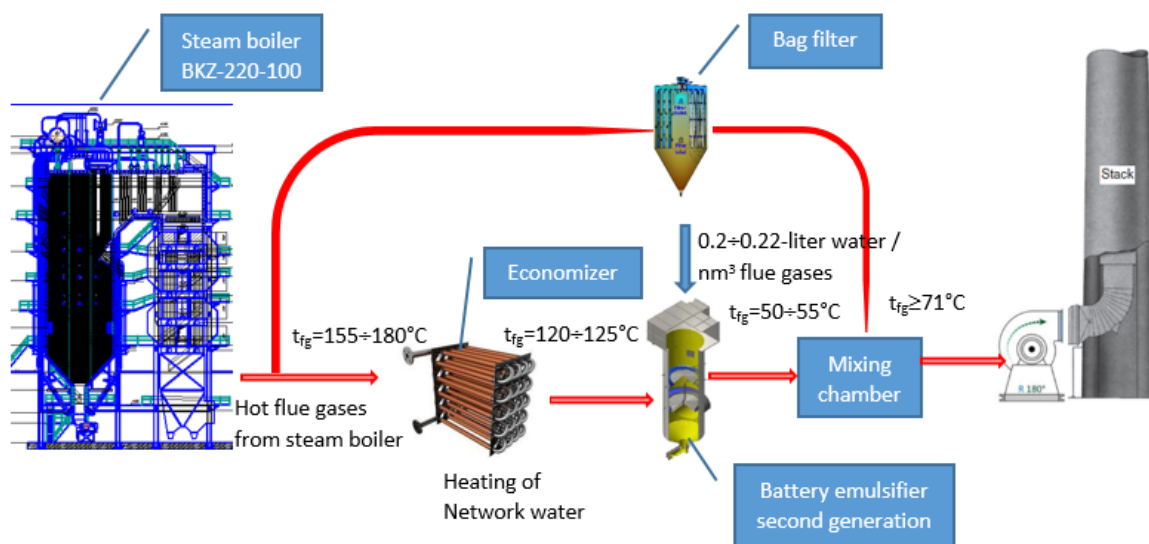

Fig.3. Diagram of the gas path after installation of a bag filter and economizer

The comparative analysis was performed between several variants of waste heat recovery units (air preheater and bag filter) of several different power steam generators (BKZ 420-140; BKZ-220-100 F; BKZ 160-100) operating at

different heat loads, with different temperatures of exhaust gases. The analysis also includes a hot water boiler type KTVK-100, located in Ekibaztuzka TPP. In the present analysis the case with the realization of an economizer and a bag

filter is not considered, but the results are similar to those with air preheaters and bag filters. In addition, the fuel used for boilers has extremely low prices, which implies poor profitability of measures related to reducing fuel consumption. The calculations were performed for several Kazakh TPPs using second-generation emulsifiers for flue gas purification.

Simulation calculations have been made with the software product „Steam boiler", which are based on established methodologies for thermal calculations of steam generators [20].

The technical parameters are determined under real conditions, as the values are accepted as average for all boilers in 2020. As the analysis was made for four different cities (Stepnogorsk, Almaty, Pavlodar, Ekibastuz) with different climatic conditions, the initial temperatures of the heated air are different for the different cities. Coal prices and average operating hours also differ and this will have an impact on financial performance (redemption period, NPV, IRR). All boilers are equipped with a second generation emulsifier system for wet flue gas purification. Normative (or measured) temperatures have been adopted in the evaluation of the heat for heating the gases after the emulsifier.

Full thermal calculations of the waste heat recovery units (WHRU) [18, 19, 22, 23, 24, 25] (air preheater in combination with a bag filter) have been made, and the production, installation and commissioning costs have been estimated at European prices. The ecological payments that can be avoided as a result of the realised savings from coal are also estimated.

Comparative analysis of waste heat recovery devices for different steam boilers and conditions

The benchmarks for selection between GTs and GPE at CHPs include:
- Fuel savings;
- Payback period;
- Net present value;
- Internal Rate of Return;
- Specific savings;

One of the most important criteria for assessing the feasibility of an investment related to energy efficiency is the minimum investment per unit of energy saved (EUR / MWh) min. This criterion is characterized by a high degree of objectivity, especially in countries where the price of fuels is many times lower than those on the world market [26]. Fig.4 shows a graphical dependence on this criterion for all analyzed steam boilers.
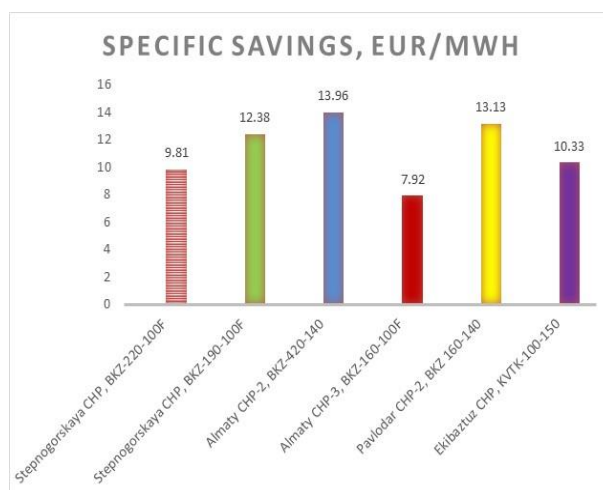

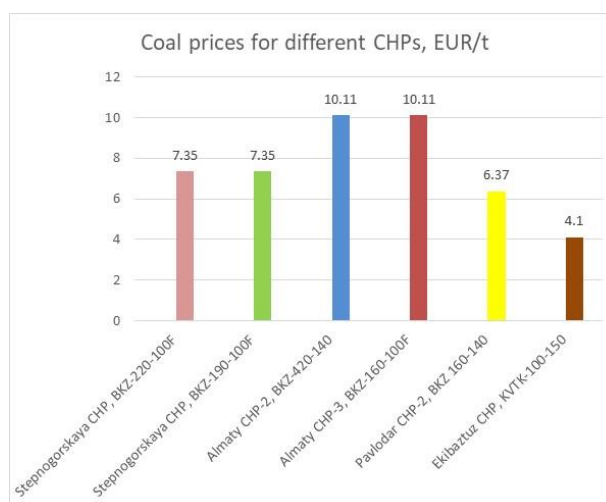**Fig.4.** Specific savings for different boilers

Fig.5. Price of Ekibaztuz coal for the different regions used by all boilers

The analysis shows that the most economically expedient is the investment for boiler BKZ-160-100 F, in TPP-3 Almaty and shows that the investment for 1 MWh of saved energy is 7.92 EUR. This assessment is complex and includes a complex dependence on several criteria: fuel price, operating time of the steam generator, exhaust gas temperature, average boiler load, etc. Undoubtedly, the price of coal has the greatest influence on the economic feasibility of the introduction of energy-saving equipment, because the assessment of savings is based on the most conservative method - the saved heat is estimated through the saved fuel. Because the introduction of a bag filter in the disposal system does not allow the entire gas flow to pass through the emulsifier, but only about 85%, which saves technical water, the price of water will therefore also have an impact on economic efficiency. An important advantage of the method

is that the dry ash mass can be collected through the bag filter and even profits from its sale can be realized. In the present analysis, this advantage is not taken into account due to the lack of investor interest in the sale of ash in Kazakhstan. In Europe and other countries such as the USA, Canada and Japan, the ash trapped by dry filters is used as a building material - mainly for the construction of roads and highways.

Fig.5 shows the price of Ekibaztuz coal for the different regions used by all boilers.

Fig.6 shows the price of technical water used in the operation of emulsifiers in different regions.
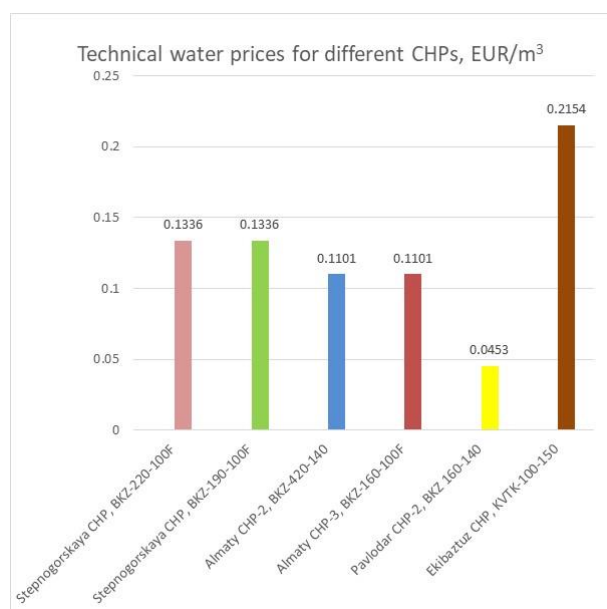
Fig.6. Price of technical water for the different regions used by all emulsifiers

CONCLUSIONS

A new waste heat recovery method is proposed and explained in the article. here are the most important conclusions based on the implemented study:

1. The proposed innovative waste heat recovery method, comprising a combination of an additional air preheater and a bag filter or alternatively an additional economizer and a bag filter, is a topical option for steam generators and boilers using "wet methods" for flue gas purification (scrubbers, emulsifiers first and the second generation). The method makes it possible to use the useful temperature drop of the flue gases, whereby part of the hot gases is purified with higher efficiency in a bag filter and then mixed with the wet gases after the existing emulsifier, without the need for hot air from the boiler air preheater.

2. The technical and financial analysis clearly shows the feasibility of the implementation of WHRU, despite the extremely low price of fuel and technical water, which negatively affect the payback period of the investment. Savings due to harmful emissions reduction (based on the emission charge) are also included in the assessment of the financial indicators. Their impact, however, is insignificant, but should be taken into account. The saved emissions reduce the average payback period of the investment by about 0.5 years.

3. The financial analysis gives an indisputable advantage to WHRU for boiler BKZ-160-100F in Almaty CHP-3. With its highest IRR of 34.7% and Payback period 2.77 years, the project is extremely attractive for implementation. However, it should be noted that all presented variants of WHRU variants are characterized by a low Payback period (2.77-6.78 years) and so are attractive and deserve high investor attention.

4. The realisation of the WHRUs has high environmental impact and is estimated to reduce Ekibaztuz coal use from 2867 to 8034 tons/year, CO_2 emissions from 4153 to 11302 t CO_2/year, SO_2 emissions from 38.8 to 108.1 t SO_2/year and NOx emissions from 18.4 to 51.7 t NOx/year, depending on the selected boilers.

5. The conclusions drawn can be used by experts in the field when making an investment decision regarding the introduction of the relevant technologies in TPP and CHP.

ABBREVIATIONS

CHP - Combined Heat and Power;
IRR - Internal Rate of Return;
NPV - Net Present Value;
NPVQ - Net Present Value coefficient;
PB - simple payback period;
TPP - Thermal Power Plant
WHR - Waste Heat Recovery;
WHRU - Waste Heat Recovery Unit.

REFERENCES

1. Iliev I., Means and methods for waste heat recovery from low-grade gas-steam flows, Monograph, University Publishing Center at the University of Ruse, 150 p. (2013) (In Bulgarian).
2. Haichao Wang, Xiaozhou Wu, Zheyi Liu, Katja Granlund, Risto Lahdelma, Ji Li, Esa Teppo, Li Yu. Lin Duamua, Xiangli Li, Ilkka Haavisto, Waste heat recovery mechanism for coal-fired flue gas in a counter-flow direct contact scrubber, Energy, Volume 237, 15 December 2021, 121531.

3. Askarova A.S., et al.: The use of a new "clean" technology for burning low-grade coal in on boilers of Kazakhstan TPPs, Bulgarian Chemical Communications, Volume 50, Special Issue G (pp. 53 - 60) (2018).

4. Anghelescu, L., Cruceru, M., Diaconu, B.M., Valentim, B., Usage of bottom ash from coal combustion to replace natural aggregate in manufacturing of building materials, (2018) 18 (4.2), pp. 231-238, DOI: 10.5593/sgem2018/4.2/S18.030.

5. Gulbe, L., Setina, J., Juhnevica, I., The use of shale ash in dry mix construction materials, (2017) 251 (1), art. no. 012013, DOI: 10.1088/1757-899X/251/1/012013.

6. Perkov, Y., Perkova, T., Recycling of Prydniprovska Thermal Power Plant fly ash, (2017) 11 (1), pp. 106-112, DOI: 10.15407/mining11.01.106.

7. Samarskaya, N., Lysova, E., Paramonova, O., Yudina, N., Ensuring the Environmental Safety of Coal-fired Power Plants for the Flue Gases Purification, (2020) 459 (2), DOI: 10.1088/1755-1315/459/2/022074.

8. Shmigol, I.N., Sedman, Ch., Marshan, U., Soldatenko, V.F., Simplified dry-wet sulfur purification of the stack gases of thermal power plants, (1996) (8), pp. 65-66, PUBLISHER: Mezhdunarodnaya Kniga, Moscow, Russian Federation.

9. Vatin N.I., D.W. Petrosin, A.I.Kalachev, P.Lahtinen, The use of ash and ash and slag waste in construction, Magazine of Civil engineering, vol.4 (2011).

10. Lahtinen P., Fly ash mixtures as flexible structural materials for low-volume roads: Dissertation for the degree of Doctor of Science in Technology. Helsinki, 102 p., (2001).

11. Zlatov N., Glazyrin S., Zhumagulov M., Aidymbayeva Z., Wastewater Treatment of the Thermal Power Plants for Desulfurization of Flue Gas, J. of Engineering Science and Technology Review, Special Issue 154-157 (2020).

12. Dzhaksybaev S.I., Muravyev I. Ya., Big coal of Ekibastuz. - M.: Nedra, (1990). - 84 p. - ISBN 5-247-00833-2.

13. Hongqiang Ma, et al., Simulation of a novel waste heat recovery system with sulfide-containing flue gas, Appl. Thermal Engineering, Vol. 187, 2021, 116556, ISSN 1359-4311, https://doi.org/10.1016/j.applthermaleng.2021.116556.

14. Pengcheng Xiao, Yanping Zhang, Yuanjing Wang, Jizhou Wang, Analysis of an improved economizer system for active control of the coal-fired boiler flue gas temperature, Energy, Volume 170, 1 March 2019, Pages 185-198.

15. Heng Chen, Yunyun Wu, Zhen Qi, Qiao Chen, Gang Xu, Yongping Yang, Wenyi Liu, Improved combustion air preheating design using multiple heat sources incorporating bypass flue in large-scale coal-fired power unit, Energy, Volume 169, 15 February 2019, Pages 527-541.

16. Bespalov V.I., S.U. Bespalova, M.A. Vagner, Environmental technologies for thermal power plants, Published by Tomsk Polytechnic University, 240 p., (2010) (in Russian).

17. Shtyogolev V. A., Battery Emulsifier Swirler Unit with Replaceable Blade Machines, Patent # RU129017U1, 2013-06-20, (2013).

18. Liu, J.; Gong, X.; Zhang, W.; Sun, F.; Wang, Q. Experimental Study on a Flue Gas Waste Heat Cascade Recovery System under Variable Working Conditions. Energies 2020, 13, 324. https://doi.org/10.3390/en13020324.

19. Iliev I, et al., Energy Efficiency and Energy Management Handbook, Bulgaria Energy Efficiency for Competitive Industry Financing Facility (BEECIFF): Project Preparation, Capacity Building and Implementation Support, ISBN: 978-619-90013-8-7, 2012, 205 p.

20. Thermal calculation of boilers (normative method), Sankt Petersburg, 1998, 259 p.

21. Test procedure for ash recovery plants of thermal power plants and boiler houses, CO 34.27.301-2001 (РД 153-34.1-27.301-2001), Moscow, (2003),https://files.stroyinf.ru/Data2/1/4294812/4294812883.htm#i1401550.

22. Jouhara H, et al., Waste heat recovery technologies and applications, Thermal Science and Engineering Progress, Volume 6, 2018, Pages 268-289, ISSN 2451-9049, https://doi.org/10.1016/j.tsep.2018.04.017.

23. Kazmi S. A. A. and M. Z. Khan, "Selection of waste heat recovery power plant on the basis of life cycle cost for cement industry in Pakistan: A demonstration and analytical study," 2012 International Conference on Emerging Technologies, Islamabad, Pakistan, 2012, pp. 1-6, https://doi: 10.1109/ICET.2012.6375483.

24. Iliev I., et al. Study of integral characteristics and efficiency of a heat exchanger of thermosiphon type with finned tubes.// Thermal Science, 2016, №5, vol.20, pp. 1227-1235.

25. Yiyu Men, Xiaohua Liu, Tao Zhang, A review of boiler waste heat recovery technologies in the medium-low temperature range, Energy, Volume 237, 15 December 2021, 121560.

26. Kostov K., Determination of technical and economic indicators of thermal power stations directly from the turbine regime characteristics, Journal EUREKA: Physics and Engineering, Number 4, (2020) DOI: 10.21303/2461-4262.2020.001358.

Usage of locally produced green hydrogen for peak load coverage in alpine regions and a local community – Simulation based on Austrian communities

M. Kramer[1], L. Eitzinger-Lange[2], M. Leeb[2], G. C. Brunauer[2,3,*]

[1]Pongauer Energy Center, Oberndorferstraße 6, 5541 Altenmarkt, Salzburg, Austria
[2]Salzburg University of Applied Sciences, Dept. R&D Smart Building & Smart Cities, Markt 136a, 5431 Kuchl, Austria
[3]TU Wien, Institute for Energy Systems and Thermodynamics, Getreidemarkt 9/E302, 1060 Vienna, Austria

Hydrogen (H_2) technology offers promising opportunities since hydrogen is a medium for the long-term storage of energy, to address peak loads by reconverting hydrogen to electricity via fuel cells. This approach can also be used for the transport sector and could be applied to fuel-cell-powered commercial vehicles. Furthermore, fuel cells enable the provision of large amounts of energy in a timely manner, relieving local electricity bottlenecks by an energy source without carbon dioxide (CO_2) emissions. This paper shows how hydrogen technology can be used to power three fuel-cell-powered snow groomers to ensure a sufficient supply over the winter season and how the identified peak loads during the annual load analysis can be reduced by 25% and 50% compared to reference value by reconverting locally produced green hydrogen via a fuel cell. According to simulation results based on observed electricity consumption from real data, there is an electricity surplus in the target community (area Salzburg) during summer months. While this surplus does not meet the entire electricity demand on an annual balance sheet, the surplus could produce H_2 of 21,250 kg yearly for the fuel-cell-powered snow groomers. Regarding additional renewable energy generation, the use of wind power and photovoltaic (PV) systems to partially cover peak loads and produce additional green H_2 using the increased electricity surplus proved feasible. The existing peak loads are caused only by ski slope operations, which accounted for up to 19 MW during November compared to the separate peak load of about municipality at 7.7 MW. The simulations concluded that unrealistically oversized fuel cells and hydrogen components would be required. The analysis demonstrates that the full power of the fuel cell would only be needed for two months a year; hence, hydrogen seems to be unsuitable for this purpose. Nevertheless, the local production of green hydrogen has significant potential in terms of achieving a green tourism future in alpine regions. Alternative strategies of using H_2 to prevent higher loads and frequency variations are reasonable and need to be explored with regard to blackout prevention strategies.

Keywords: Power2X, green hydrogen, water electrolysis, sector coupling, heavy-duty vehicles, peak shaving, fuel cell powered snow groomer

INTRODUCTION

The shift to renewable energy sources is particularly important so that climate policy goals can be met [1]. The expansion of renewable energy producers in not only urban but also suburban areas, such as in tourism-intensive alpine regions, is indispensable to achieve a share of at least 32% of renewables in the European Union (EU) according to the [2]. The temporal discrepancy between electricity generation and consumption in a tourism community should be a focus for the further expansion of renewable energy and should at least cover peak loads; ideally, however, the energy production and energy consumption should be balanced over a longer period of time.

The issue of the year-round balance between production and consumption plays an essential role in connection with the volatility of renewable energy production. The value chain for locally produced green hydrogen starts with water electrolysis. Electrolysis is a process that involves splitting water into its components: hydrogen (H_2) and oxygen (O_2).

The hydrogen produced can be used within the electricity and transport sectors. For the electricity sector, the temporarily stored hydrogen is converted back into electricity via the fuel cell and can smooth out peak loads by supporting the local power grid. Among other applications, the hydrogen can be used for the transport sector. The transport sector in this paper includes only the supply of three fuel-cell-powered snow groomers (FC-PSG) over a winter season; this field is possibly to become subject to regulations similar to those that apply to heavy-duty vehicles in the EU, which require a reduction of CO_2 emissions [3].

This paper focuses on the suburban area and includes a tourism intensive community in Salzburg (for reasons of data protection law, the community may not be published) according to [4]. Other papers increasingly examined the use of hydrogen in conjunction with battery storage systems such as Fasihi & Breyer (2020) or Papadopoulos et al. (2020) or power-to-gas applications such as Weidner et al. (2018) [5-7]. Therefore, this is the first paper dealing with the integration of hydrogen in tourism

---

* To whom all correspondence should be sent:
georg.brunauer@fh-salzburg.ac.at

regions and mountain railways with high peak loads in details.

In addition, this paper describes how mountain railways can responsibly invest millions of euros in reducing CO_2 emissions to preserve their livelihood while simultaneously promoting economic efficiency and climate protection. This research is conducted to enable communities and ski resorts to make the leap "into a green energy and tourism future" and secure "Austria's system leadership in the field of ecologically optimized winter tourism" [8].

OBJECTIVES

The Objectives cover the main two sectors. For the transport sector, the supply of the FC-PSG and for the electricity sector the peak load coverage will be investigated. Derived from this, various research questions arise:

- How do the monthly average peak loads behave in the community and the mountain railways?
- To what extent can green hydrogen be used efficiently and effectively in an alpine tourism region to supply three FC-PSG and to reduced identified peak loads by 25% and 50% by means of conversion back into electricity via the fuel cell?
- How are the adequate system components (electrolyzer, storage tank and fuel cell) to be designed for each scenario?

The original goal was a 100% supply of renewable energy and the use of hydrogen for the community and mountain railways. However, the analysis of the electrical data, based on real data in 15-minute timestamps from Salzburg Netz GmbH (local energy supply service provider), showed in Fig. 1 that the peak loads of the mountain railways produced enormous consumption by the snow cannons and therefore a 100% coverage was considered improbable. Since the community did not have such large peak loads, an approximation of 25% and 50% were chosen to smooth the peak loads of the mountain railways.

In Fig.1 the energy consumption reaches hourly peaks of over 19 MW in the months of November and December. In general, the load curve of the mountain railways behaves similarly over the entire underlying data set. Furthermore, the investigation showed that summer tourism and the accompanying use of the cable cars in this community requires significantly less electricity than in winter.

In comparison, the local community has a far less significant peak load of 7.7 MW, however has a vastly higher annual electrical consumption of about

34 GWh compared to the mountain railway's 10.5 GWh. This highlights the importance of handling peak loads for hydrogen energy systems to be viable.
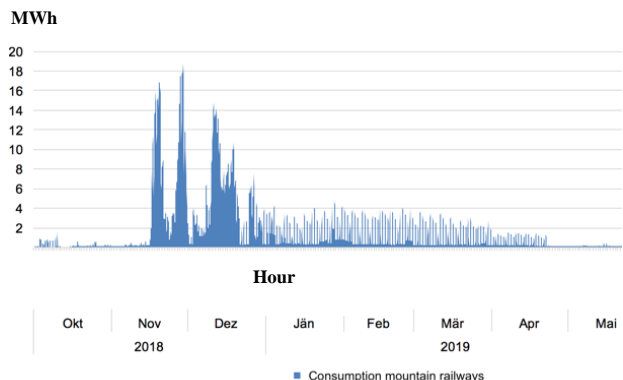

Fig.1. Consumption mountain railways from the season 2018/2019 (own figure)

Based on the whole dataset from community and mountain railways different scenarios are set up in section three. The results are presented in section four. Finally, in section six (discussion and conclusion), the research questions are divided and answered in paragraphs, whereby research question two and three are combined, because the system components of hydrogen electrolysis are connected to cover peak loads.
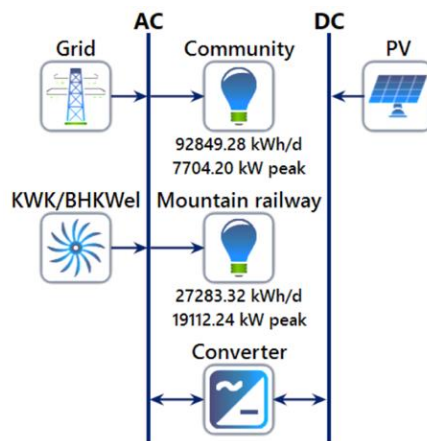

Fig.2. System configuration of base case

METHODOLOGY

Different scenarios are constructed and simulated using HOMER Pro (https://www.homerenergy.com; hereafter, HOMER). The provision of hydrogen for three FC-PSG in regular operation over a winter season is simulated; thereafter, further scenarios are built to meet peak demands with additional renewable sources. The hydrogen supply of the FC-PSG in scenarios 1, 2 and 3 is guaranteed with a maximum priority. In case of a peak load coverage, various combinations were used to attempt to

43

contain the supply of hydrogen to the grid with the return of electricity via the fuel cell, especially at the end of the year. This results in a base case (Fig.2) presenting the current status in the whole area without using hydrogen electrolysis and three additional scenarios (Fig.3, Fig.4 and Fig.5) utilizing hydrogen electrolysis and peak load coverage:

The scenario cases have been adjusted for economically viable configurations of renewable energy production within the constraints of heavily alpine geography.

SCENARIOS SETTINGS

a) Base case: actual situation in the target community without hydrogen electrolysis
b) **Scenario 1**: H_2 production to supply three FC-PSG and max. peak load coverage, without additional renewables
c) **Scenario 2**: H_2 production to supply three FC-PSG and approx. 25% peak load coverage, with additional renewables (1 MWp PV plant and 2x wind turbines of 4.2 MW each)
d) **Scenario 3**: H_2 production to supply three FC-PSG and approx. 50% peak load coverage, with additional renewables (2 MWp PV plant and 4x wind turbines of 4.2 MW each)
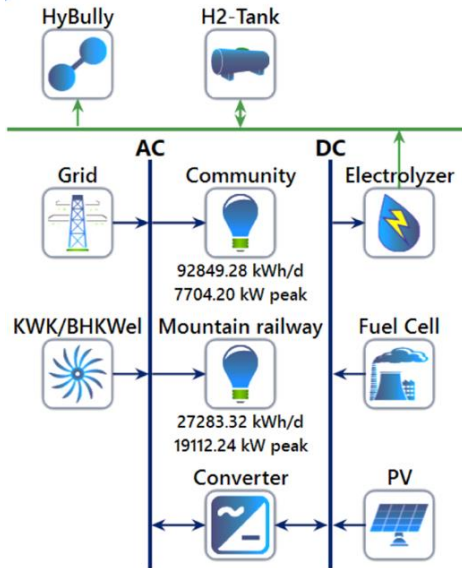
Fig.3. System configuration of Scenario 1

For the simulation of the hydrogen quantity for the three FC-PSGs, a master's thesis which deals with a fuel-cell-powered snow groomer is used [9]. Since there are different applications and requirements for a snow groomer, the required hydrogen quantity varies, so a reference vehicle was assumed in this paper. This representative vehicle

has a service time of 9.3 h, an idle rate of 8.95%, and covers a distance of 69.4 km per day and for this vehicle, the required hydrogen consumption is around 47 kg. This results in the following amount of hydrogen for three FC-PSGs assuming that these vehicles are used for 150 days:

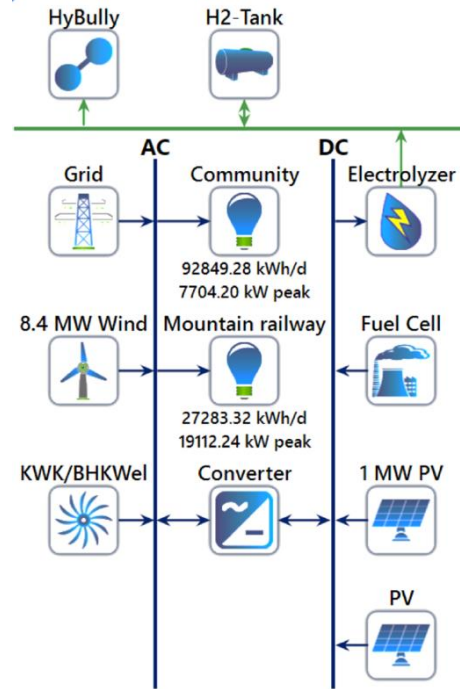$$47kg\ H_2 * 3\ HyBullys * 150\ Operating\ days = 21,150\ kg \tag{1}$$

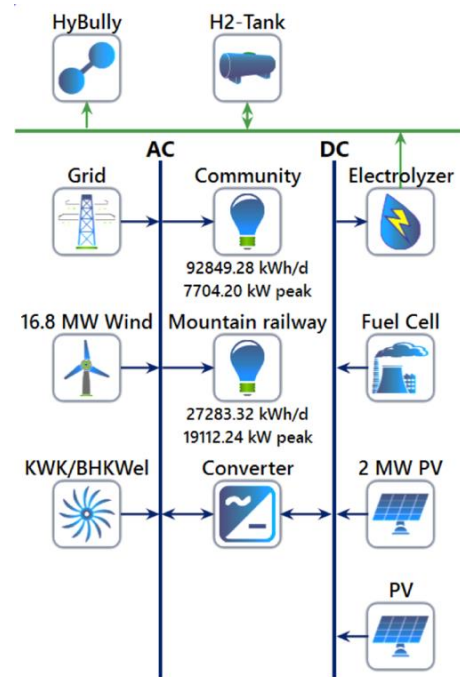
Fig.4. System configuration of Scenario 2

Fig.5. System configuration of Scenario 3

This amount of hydrogen is defined as a fixed parameter for the hydrogen supply of the three FC-PSGs in the ski area. Within HOMER, this quantity must be available by 31st of October to supply the groomers during the winter period.

DATA

The electrical data set refers to the balance area (community and mountain railways) and is implemented separately in HOMER. The values for the year 2018/2019 were chosen with the help of the inventory analysis, which corresponds approximately to the average of the existing data. The analysis results show that 33.97 GWh/a are consumed by the community and 9.95 GWh/a by the mountain railways. The total production in the from installed PV plants in the community amounts to 16.34 GWh/a. For the hydrogen components, the parameters in Tab.1 apply, while, for the additional installed renewable energy sources, the parameters in Tab.2 apply.

Table 1. Implemented hydrogen electrolysis parameters for the simulation

---

Electrolyzer [10-11]

Efficiency	85%
Minimum load ratio	5%
Electrical bus	DC
Size	iterative dimensioning
Schedule	HOMER optimized

Fuel Cell [12-13]

Efficiency	50%
Minimum load ratio	5%
Electrical bus	DC
H_2 characteristics	lower heating value 120 MJ/kg
H_2 characteristics	density 0,090 kg/m^3
Size	iterative dimensioning
Schedule	focused on Nov, Dec due to the identified peak loads, other months HOMER optimized

---

gaseous H_2 Tank

Initial tank level	0 kg
Require year-end tank level	No
Tank Size	iterative dimensioning

Converter AC

Efficiency	98%
Parallel with AC generator	Yes

Converter DC

Efficiency	95%
Relative capacity	100%

In HOMER, the "cycle load strategy" is selected for the simulation. This strategy is a dispatch strategy where all power sources (grid, wind, PV, fuel cell) operate at full output power whenever the power sources must serve the primary load. In this case the community and the mountain railways are the consumers. The simulation software distributes the controllable power sources (grid, wind, PV, fuel cell) in a two-stage process observing a 15-minute time step for the simulation. HOMER selects the optimum combination of power sources (which consists primarily of renewable sources) to serve the electrical load (community and mountain railways).

Table 2. Implemented parameters of additionally installed renewable energy sources

---

Photovoltaics [14]

	Scenario 2	Scenario 3
Power output	1 MWp	2 MWp
Efficiency	19,01%	
Electrical bus	DC	
Operating temp.	+85°C to -40°C	
Derating factor	90%	
Relative capacity	100%	
Solar radiation	3.25 kWh/m^2/day [15]	

Wind turbine [16]

	Scenario 2	Scenario 3
Power output	2 units [8.4 MW]	2 units [16.8 MW]
Hub height	135 m	
Rotor diameter	127 m	
Electrical bus	AC	
Ambient temp.	5.34°C [17]	
Wind speed	6,5 m/s [18]	

RESULTS

The results of the simulation refer to the reference year, 2018/2019. As the primary load or consumer, the community and the mountain railways were initially simulated separately but were subsequently combined as presented in Tab.3, Tab.4 and Tab.5. The total electricity generated from renewables are also subsequently combined. In Tab.4, the peak load coverage refers to the month of November. According to the inventory analysis, considerable peaks occur during November due to the snow-making systems of the mountain railways, which can be partially covered by the production of the fuel cell. The base case and the three scenarios are divided into electrical data, peak load coverage and hydrogen electrolysis.

Table 3. Results of electrical data

Base case	Scenario 1	Scenario 2	Scenario 3
Primary load [kWh/a]			
43,848,399	43,848,399	43,848,399	43,848,399
Renewables [kWh/a]			
16,339,251	16,339,251	46,642,059	76,944,867
Grid purchased [kWh/a]			
28,875,455	28,825,665	8,053,184	615,977
Grid sold [kWh/a]			
1,283,350	135,267	545,185	15,950,372

Table 4. Results of peak load coverage

Base case	Scenario 1	Scenario 2	Scenario 3
Max. peak load Nov. [kW]			
23,105	23,105	17,296	11,293
Peak load coverage [%]			
-	-	25.14	51.12
Fuel cell [kWh/a]			
-	51,467	4,829,761	8,206,272

Table 5. Results of hydrogen electrolysis

Base case	Scenario 1	Scenario 2	Scenario 3
Electrolyzer [kW]			
-	1,200	7,000	10,000
Fuel cell [kW]			
-	300	4,000	10,000
Tank [kg]			
-	75	150,000	200,000
Converter [kW]			
3,136	2,986	6,719	10,228
H_2 for 3x FC-PSG [kg]			
-	21,150	21,152	21,152
H_2 for fuel cell [kg]			
-	3,088	289,786	492,376

Scenario 1 is not suitable for peak sheaving, as only a small peak load coverage is possible due to the fact that the fuel cell size of 300 kW is not sufficient for peak load coverage. In contrast, scenario 2 (see Tab. 4) smooths the peaks by 25.14% in November, there is no need to purchase any electricity from the grid from May to October. Scenario 3 (see Tab. 4) covers peaks of 51% in November and 53% in December.

Scenario 3 covers the burden of the entire balance area from February to October but only half in the winter months of November and December. The results examined according to the inventory analysis related to the short-term peak loads of the mountain railways, occurring within minutes, so the additionally installed capacity of the fluctuating renewables should be able to provide the energy within a few minutes. In contrast, the fuel cell produces about 4.8 GWh of electricity in scenario 2 and about 8.2 GWh/a in scenario 3.

CONCLUSIONS

In terms of the monthly average energy needed, the use of snow-making systems and their

infrastructure causes the peak loads of the mountain railways to increase to 465% (max. ~ 19.1 MW) in November, while simultaneously energy demand in the community increases to 155% (max. ~ 6.1 MW) to their respective reference values. It should be noted, that this is not highest annual demand peak of the community, which takes place outside of November.

According to predefined parameters for hydrogen technology from the literature, the simulation results (scenario 1) suggest that currently, without additional renewable energy sources, a 1.2 MW electrolyzer would be the optimal design to produce the hydrogen supply of 21,150 kg for three FC-PSG. In addition, to ensure the operation of the FC-PSG during a winter season, a surplus of 3,088 kg H_2 can be produced. In this scenario, 90% of the locally produced annual surplus is used for electrolysis. For the months of November and December, an attempt was made to use this surplus hydrogen by converting it back into electricity in a fuel cell, resulting in a design of 300 kW. However, this design can only cover 1.6% of the consumption peaks. In terms of the balance sheet, there is little change in this scenario within the municipal area in relation to the electricity self-supply.

To shave the peak loads at 25% and 50% each (scenarios 2 and 3), the use of additional renewable energy sources is required. Taking realistic local data into account, average wind speed and solar irradiation and their complementarity to local hydropower, a combination of wind power and PV systems proved reasonable. For these scenarios, PV systems with 1 or 2 MWp and two or four wind turbines with a capacity of 4.2 MW in total seems to be a comprehensible approximation. These results were put into the respective simulation models. In both scenarios, the primary load in the balance area (community and mountain railways) would be completely supplied by local power plants. According to the simulation software, however, some peak loads would continue to exist because of the volatile load profiles of the renewables. In principle, a power surplus is used for a 7 or 10 MW electrolyzer. Despite twice the installed capacity of the renewables in scenario 3, a maximum electrolyzer capacity of 10 MW is required because the amount of hydrogen produced is already sufficient for the designed fuel cell to cover 50% of the peak load in November and December. An even larger quantity of H_2 could be produced from the resulting electricity surplus. Subtracting the H_2 quantity for three FC-PSGs according to the predefined parameters of the electrolyzer, this results

in quantities of 289,786 kg H_2 (scenario 2) and 492,376 kg H_2 (scenario 3), respectively, which are available to the fuel cell with an output of 4 MW and 10 MW. Thus, the peak loads in November can be covered by exactly 25.24% and 51.12%, and the electricity from the local grid can be limited.

DISCUSSIONS

The results regarding the optimal design of the fuel cell for H_2-regenerating into electrical power demonstrate that the fuel cell capacity is only fully utilized in November and December; hence, the fuel cell is only in partial load operation during the other months. Among other factors, the volatility of the renewables influences the result, so the peak loads can be covered more effectively by additional renewables. According to the results of the simulation, a fuel cell for peak load coverage is questionable under the predefined conditions, and the hydrogen components would require high power capacities.

The specific use-case of supplying FC-PSGs such as snow groomers with locally produced hydrogen is shown to be viable already with small expenditure. Scenarios 2 and 3 give insights on how hydrogen interacts with heavy peak load management on a local level in an alpine tourism environment. This knowledge can be further expanded by applying it to a more suitable energy community in additional studies.

CONCISE CONCLUSIONS

Specifically, further study by the authors will be concluded in the municipality of Obertrum within the project "*H2 Village*". A less seasonally focussed yet still pronounced peak load profile allows more flexibility with hydrogen usage around the year. Additionally, using hydrogen for a local beverage industry's energy and logistics demands applies further understandings of this paper in a widely replicable manner. Particularly the usage of hydrogen in adapted lorries is expected to decrease emissions significantly.

Since several topics were not considered in this research paper for strategic reasons and due to the system limits of the simulation, further investigations are necessary to establish the use of hydrogen electrolysis in alpine regions (*e.g.* energy communities). For example, in order to analyze the economic efficiency, the costs for the achieved peak load coverage would have to be compared with the current energy price of the mountain railways. Another aspect is the investigation and further use of oxygen, which is a by-product of hydrogen

electrolysis. Its use would have a positive effect on the calculation of the economic efficiency of hydrogen electrolysis. Regarding the extension of the system boundaries, this could include the thermal energy utilization that is generated during the conversion of electricity from the fuel cell - for example, by feeding the resulting thermal energy into a district heating network.

If the system boundaries are extended, electrochemical storage systems can create synergies between the electricity, transport and heating sectors. Thus, from a holistic perspective, both the economic efficiency and the system design as well as the energy balance of the resulting system can be significantly influenced.

REFERENCES

1. DIRECTIVE (EU) 2019/944 OF THE EUROPEAN PARLIAMENT AND OF THE COUNCIL of 5 June 2019 on common rules for the internal market for electricity and amending Directive 2012/27/EU (recast); Retrieved on 13. June 2020, from https://eur-lex.europa.eu/legal-content/EN/TXT/HTML/?uri=CELEX:32019L0944&from=de
2. DIRECTIVE (EU) 2018/2001 OF THE EUROPEAN PARLIAMENT AND OF THE COUNCIL of 11 December 2018 on the promotion of the use of energy from renewable sources (recast), from https://eur-lex.europa.eu/legal-content/DE/TXT/?uri=celex:32018L2001
3. European Union. (2018). CO2 emissions of heavy-duty vehicles: Council adopts monitoring and reporting rules.
Retrieved on 12 April 2020, from https://www.consilium.europa.eu/de/press/press-releases/2018/06/25/co2-emissions-of-heavy-duty-vehicles-council-adopts-monitoring-and-reporting-rules/
4. Krajasits, C., Andel, A., & Wach, I. (2008). *Stellenwert der Gemeinden für den österreichischen Tourismus, Österreichisches Institut für Raumplanung*. Retrieved on 18. September 2019, from https://www.oir.at/files/download/projekte/Raumplanung/Tourismusgemeinden_EB_Sep08.pdf
5. Fasihi, M. & Breyer, C. (2020). Baseload electricity and hydrogen supply based on hybrid PV-wind power plants. *Journal of Cleaner Production*, 243, 118466. https://doi.org/10.1016/j.jclepro.2019.118466

6. Papadopoulos, V., Desmet, J., Knockaert, J. & Develder, C. (2018). Improving the utilization factor of a PEM electrolyzer powered by a 15 MW PV park by combining wind power and battery storage – Feasibility study. *Int. J. of Hydrogen Energy*, 43 (34), 16468–16478. https://doi.org/10.1016/j.ijhydene.2018.07.069

7. Weidner, S., Faltenbacher, M., François, I., Thomas, D., Skùlason, J. B. & Maggi, C. (2018). Feasibility study of large scale hydrogen power-to-gas applications and cost of the systems evolving with scaling up in Germany, Belgium and Iceland. *International Journal of Hydrogen Energy,* 43 (33), 15625–15638. https://doi.org/10.1016/j.ijhydene.2018.06.167

8. Klima- und Energiefonds. (2019). HySnowGroomer, Klima- und Energiefonds. Retrieved on 27. July 2020, from https://www.klimafonds.gv.at/unsere-themen/mobilitaetswende/leuchttuerme-der-elektromobilitaet/hysnowgroomer/

9. Heinzelmann, T. (2018). *Entwurf eines Brennstoffzellenbetriebenen Antriebskonzepts für einen PistenBully.* Masterthesis. Univ. Stuttgart.

10. Habermeyer, F., Kurkela, M., Kurkela, E., & Adelung, S. (2018). *Flexible combined production of power, heat and transport fuels from renewable energy sources. Review of electrolysis technologies and their integration alternatives*. Retrieved on 13. June 2020, from http://www.flexchx.eu/pdf/D2_1_Electorolysis_ReviewFLEXCHX_DLR_03092018_v3.pdf

11. Carmo, M., Fritz, D. L., Mergel, J., & Stolten, D. (2013). A comprehensive review on PEM water electrolysis. *International Journal of Hydrogen Energy,* 38 (12), 4901–4934. https://doi.org/10.1016/j.ijhydene.2013.01.151

12. Santos, M., Zenith, F., & Glielmo, L. (2019). *Energy analysis of the Raggovidda integrated system. Hydrogen-Aeolic Energy with Optimised Electrolysers Upstream of Substation*. Retrieved on 16. May 2020, from http://www.haeolus.eu/wp-content/uploads/2019/01/D5.1.pdf

13. Arshad, A., Ali, H. M., Habib, A., Bashir, M. A., Jabbal, M., & Yan, Y. (2019). Energy and exergy analysis of fuel cells. A review. *Thermal Science and Engineering Progress*, 9, 308–321. https://doi.org/10.1016/j.tsep.2018.12.008

14. Kioto Solar. (2020). *Datenblatt Photovoltaikmodul POWER60 ALPIN.* Retrieved on 15. July 2020, from https://www.kiotosolar.com/de/downloads.html?dokumententyp%5B%5D=datenblatt&file=files/sonnenkraft/KIOTO/Downloadbereich/Datenblaetter/Datenblaetter%202020/KIOTO_SOLAR_DB_POWERALPIN60_DE_2020.pdf

15. Land Salzburg. (2020). Erneuerbare Energie. Photovoltaik. Retrieved on 13. June 2020, https://www.salzburg.gv.at/themen/energie/erneuerbare-energie/pv

16. Enercon. (2020). *Produktübersicht*. Retrieved on 15. April 2020, https://www.enercon.de/fileadmin/Redakteur/Medien-Portal/broschueren/pdf/ENERCON_Produkt_de_042017.pdf

17. ZAMG. (2020). Klimamonitoring. Retrieved on 13. June 2020, from https://www.zamg.ac.at/cms/de/klima/klima-aktuell/klimamonitoring/?station=15712&param=t&period=period-y-2019&ref=3

18. *Windatlas und Windpotentialstudie Österreich.* (2019). Windatlas und Windpotentialstudie Österreich. Retrieved on 16. June 2020, from http://ispacevm11.researchstudio.at/index_v.html

The problem with indoor radon and solution in the use of geothermal water

N. Chobanova[1*], B. Kunovska[1*], D. Djunakova[1], J. Djounova[1], A. Angelova[1], Z. Stojanovska[2], K. Ivanova[1]

[1]National Centre of Radiobiology and Radiation Protection, 3 Georgi Sofyiiski, Str., 1606 Sofia, Bulgaria
[2]Faculty of Medical Sciences, Goce Delcev University of Stip, 10-A Krste Misirkov st., 2000 Stip, Republic of North Macedonia

Bulgaria is rich in geothermal water. The radon level in spas buildings depends on soil underneath, thermal water and the ventilation conditions. The aim of the paper is to analyses influence of ventilation system on indoor radon in air in the spa buildings. Direct measurements of radon in the air were performed in treatment rooms (treatment with thermal water and without) and mineral pools. A statistically significant difference was found between the indoor radon levels in treatment rooms using water and those without water, located in branches with high radon concentration (MW, p = 0.032). The spectra of the rooms for 24 hours were considered for analysing the indoor radon daily variations. The radon arithmetic mean value in rooms with operating ventilation system was 148 Bq /m^3, and in those without - 756 Bq /m^3 and the statistically difference is significant (MW, p <0.0001). Further the radon levels decrease 1.7 to 3.3 times when the ventilation works. To improve air quality in Rehabilitation Centres, the ventilation system must be in good function. The mineral water is also a source of radon and varies according to its degree of use. The effective dose of a visitor who performed thermal procedures was also evaluated.

Keywords: Indoor radon concentration, geothermal water, ventilation system, spas, direct measurement, spectra

INTRODUCTION

Bulgaria is a country that is relatively rich in geothermal water, the temperature of which is in the range 25ºC-100ºC. The mostly (>95%) of natural mineral springs are concentrated in the southern part of Bulgarian territory. Generally, there are more than 170 geothermal fields in Bulgaria and numerous manifestations have been discovered and delineated (~ 1000 natural mineral springs and 2000 boreholes) [1, 2]. According to the Water Act, 102 of all hydrothermal fields in Bulgaria are specified as exclusive state property. The rest are municipal property [3].

Thermal waters can be used for electricity production (at temperatures > 150°C) or at lower temperatures for direct application - heating of buildings and greenhouses, bottling of mineral water, etc. Traditionally, their greatest application is in the field of balneology. Most of them are very popular with the population in the area of prevention, medical therapy and rehabilitation as well as tourism and recreation [1].

The major factors that contribute to the geothermal development in Bulgaria are: long tradition, favourable climate, appropriate thermal water composition and a developed spa system [1].

In spa environment radon and its decay products have been considered as the main ionizing radiation exposure for both users and workers therefore the radon in spas should be monitored [4]. Radon is recognized as a leading cause of lung cancer incidence, excluding tobacco [5, 6]. The risk of radon exposure is mostly associated with high radon concentrations in confined environments and the subsequent inhalation. Radon is formed from radium, dissolve in groundwater, which is contact with soil and rocks containing radium. Its high degree of mobility allows it to be transported to the surface and then diffuse into the atmosphere and buildings. Geothermal spas are one of the common confined places where radon may be present in higher concentrations due to aeration, small ventilation or constructive details [7, 8, 9, 10]. Such places must be subjected to special investigation, taking into account that radon level in spas buildings depends on both two potential factors (soil underneath and thermal water) and the ventilation conditions of various premises.

The European Directive 2013/59/EURATOM defined the reference level for the annual average activity radon concentration in houses, public buildings and workplaces should not be higher than 300 Bq.m^3

* To whom all correspondence should be sent:
b.kunovska@ncrrp.org; n.chobanova@ncrrp.org

[11]. The requirements have been harmonized into Bulgarian national legislation [12].

The aim of the article is to analyse the influence of water as an additional source of radon in the air and daily variation of indoor radon in order to assess the effect of the ventilation system, as a possible solution to reduce the exposure of the population.

MATERIALS AND METHODS

Area of study

To achieve the purpose, the variation of indoor radon concentration in 11 branches of the Specialized Hospitals for Rehabilitation - National Complex (85% of the national branches with thermal spas in Bulgaria), located on the territory of Bulgaria have been studied. These sites use geothermal water for treatment and that's why we agreed to call them spa. 36 treatment premises located in 11 branches were surveyed. The spa buildings are located in 9 districts of Bulgaria - one in Sofia district, one in Plovdiv district and the other 7 are in western part of Bulgaria, in the districts of Blagoevgrad, Kyustendil, Pazardzhik, Stara Zagora, Smolyan, Montana and Veliko Tarnovo, respectively. Fig.1 shows the location of the studied branches.

Fig.1. Location of the studied Bulgarian spas (1-Narechenski Bani, 2-Momin Prohod, 3-Hisarya, 4-Pavel Banya, 5-Varshets, 6-Bankya, 7-Kyustendil, 8-Sandanski, 9-Velingrad, 10- Banite,11- Ovcha Mogila)

The spas are open all year round. Many patients are treated in these spa complexes, which are recommended for respiratory diseases, dermatology, rheumatology, neurological diseases etc. They apply different services and treatment techniques as baths, jets, circular showers, inhalations, sprays, sauna, underwater massage and manual massage. The treatment rooms are supplied with thermal water which contains specific amounts of dissolved substances and together with the high temperature turn out beneficial health effects. Spring water is pumped from its source through a mechanical drainage system located a few meters outside the spa.

The variations of radon in the air of the studied premises have a great variability and can be controlled by many factors (ventilation, number of patients using the equipment, humidity, etc.). The ventilation in the treatment rooms, apart from the naturally is carried out through a built-in ventilation system. Information about the ventilation system in the premises was collected via specially prepared questionnaire and analysis of the influence of the factor was made too. There are working general or partial ventilation systems in 5 branches. In other six buildings there are no ventilation systems. In most branches the ventilation system works 4 hours a day, and in only one of them is less. A total of 36 measurements were performed in treatment rooms (treatment with thermal water and without) and mineral pools. 18 of the measured rooms are located on the ground floor, eight are in the basement, nine - on the first floor and only one on the second floor.

Measurement methods

Radon concentrations in the air of the spa complexes were measured by *Alpha Guard PQ2000* radon monitor (Genitron Instruments, Germany), detector AlphaE (Saphymo GmbH, Germany) and TERA (TSR3D) system (Tesla, Czech Republic). The equipment also registered air temperature (-20°C to +60°C), humidity (10% to 90%) and energy spectrum. Measuring system Alpha Guard PQ2000 uses a principle of the ionization chamber (contaminated background of 40 $Bq.m^3$); radon enters the detection area (through a Rn progeny preventing filter), where it is measured by α-spectrometric technique. The device is not affected by high humidity and vibration. Its range has a linear dependence from 2 $Bq.m^{-3}$ to 2,000,000 $Bq.m^3$. Data analysis, processing, and storage were performed using the DataEXPERT software. With this equipment radon measurement were performed in the spa centres for 24 hours in the period from February to June 2019 (12 measurements).

AlphaE is an active measurement device for detecting and recording the radon concentration. Based on the diffusion principle with silicon detector the radon gas diffuses through the entry holes of the case into the inner of the diffusion chamber. As the holes are entirely covered by a Gore-Tex membrane only the radon gas can enter the chamber while the decay products, are retained by the filter.

With *TERA (TSR3D)* system it is possible to continuously monitor the radon concentration in the range of 20 $Bq.m^3$ to 1 $MBq.m^{-3}$, with possibilities for measuring the instantaneous volume activities of radon: short-term (average hourly) and long-term (daily average). The measurement uncertainty is as follows <13% at 300 $Bq.m^3$ for 1 hour; <3% at 300 $Bq.m^3$ in 24 hours. The 24 hours' radon spectra were measured from October 2019 to February 2020 with newly received equipment, supported by the Bulgarian National Science Fund. Direct measurements and monitoring of the radon concentration over time allow clarification of the possible reasons for the dynamics of radon, as well as the formulation of specific conclusions about its distribution in time and space of the measured premises.

During these measurements, the devices Alpha Guard PQ2000 and AlphaE was operated in the 10 minutes' data sampling cycle while TERA (TSR3D) system for 1 hour. Direct radon measurements were performed in treatment rooms and mineral pools, which are located in ground floor, basement and first floor.

Information from questionnaire

Through a purposive questionnaire we received information about the type of building construction, year of construction, presence of mechanical ventilation systems, presence of elevators, does ventilation system works, done any energy saving measures, the types of windows etc. Such a questionnaire was completed by an employee in each spa branch.

Statistical analysis

To perform statistical analysis was used IBM SPSS Statistics, v. 23. The measurements are grouped as follows: types of premises (with water and without water) and premises with ventilation system (working and no working), to assess the radon variations. Descriptive analysis, parametric and non-parametric tests are applied

for data processing. A parametric test of Kolmogorov-Smirnov was used to check the normality of the distribution of radon concentration in air and a non-parametric Mann-Whitney test was applied to compare two independent groups. Level of significance is $p<0.05$.

RESULTS AND DISCUSSION

The descriptive statistic of direct measurements of radon concentration in 36 spa premises is presented in Table 1. The radon concentrations are not following a log normal distribution ($p<0.05$). The obtained arithmetic mean and standard deviation have been found to be 604 $Bq.m^3$ and 1020 respectively.

**Table 1.** Descriptive statistic of radon concentrations measured in 36 premises

Premises	AM CRn	Min CRn	Max CRn	CV
	$Bq.m^3$	$Bq.m^3$	$Bq.m^3$	%
36	604	16	4455	169

The coefficient of variation is 169%, which shows a large difference between the concentrations of radon in the studied premises. This percentage is so high due to the large range of radon concentration from 16 $Bq.m^{-3}$ to 4455 $Bq.m^{-3}$. The large deviation of radon levels is due to different factors such as: location and construction of the building, the presence of a working ventilation system, the composition of the mineral water in the individual spa buildings.

We analysis two groups of premises: rooms using water and those who do not use water (Fig.2). The indoor radon is higher in rooms with water (AM=634 $Bq.m^3$), than in rooms without water (AM=355 $Bq.m^3$), indicating that the use of geothermal water for treatment increases radon levels in the air.

To explore the hypothesis if the thermal water affected the variations of radon in treatment rooms the measurements in two branches (Narechenski Bani and Momin Prohod) with high levels of radon are considered for detail analysis. A statistical test to confirm the hypothesis that the used mineral water is an additional source of radon in air of the studied premises was performed. The values of indoor radon concentration differ significantly between

the studied premises - with water and without water (MW, p = 0.032). Thermal water is a radon source, which varies according to its degree of use in the treatment rooms. The analysis of the spectra indicates that usually the indoors Rn values vary depending on the work activities during the day. Our results are comparable with the values reported for spas in other regions worldwide [10, 13].
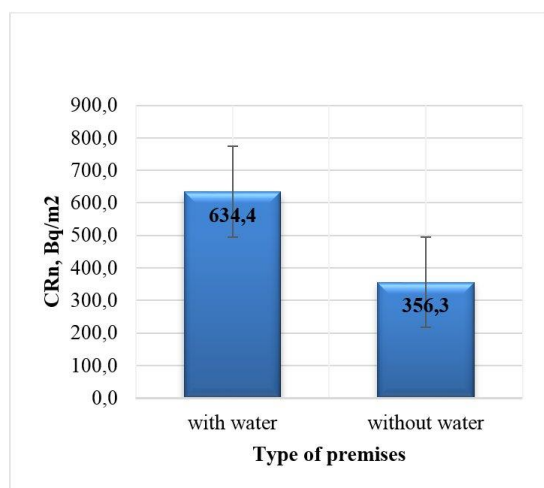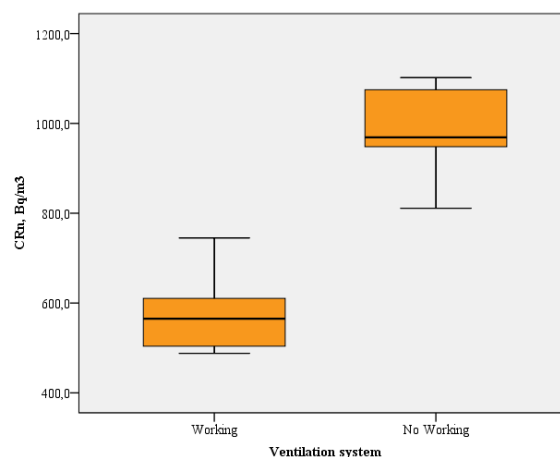

Fig.2. Distribution of radon concentration depending on the use or non-use of water in the treatment premises

In order to evaluate the efficiency of the ventilation system, the results of Narechenski Bani and Ovcha Mogila are analyzed. Both sites have a well-functioning ventilation system operates more than 4 hours a day (it turns off in the evening and turns on in the morning). To be analyzing the indoor radon daily variations in premises the spectra of direct measurements for approximately 24 hours were monitored. In the Narechenski Bani branch, radon levels have been found above the national reference level for both period of measurement. The arithmetic mean of CRn when ventilation system is functioning AM=572 $Bq.m^3$ and when is non-operating AM=984 $Bq.m^3$. At these high levels it is necessary to carry out additional activities to improve ventilation (air exchange rate measurement, radon mitigation systems, and others). The comparison of radon values during running and stopped ventilation shows a statistically significant difference (MW, p<0.0001) (Fig.3).

In Ovcha Mogila are registered low levels of radon. The spa is situated away from the thermal water source and during the transport of water

from the spring to the rooms degassing of radon occurs and this is the possible reason for low radon concentration [14, 15]. When the ventilation system working the AM is 18 $Bq.m^3$ and when it is not functioning AM is 60 $Bq.m^{-3}$. A statistically significant difference was found (MW, p=0.002) (Fig.4). The concentration of radon decreases depending on the functioning of the ventilation system, the size of the room, the meteorological conditions and, etc.

Fig.3. Distribution of the indoor radon depending on the efficient of the ventilation system in Narechenski Bani.

It is interesting to note that radon concentration decreases 3.3 times in Ovcha Mogila while radon levels in Narechenski Bani decrease 1.7 times only.
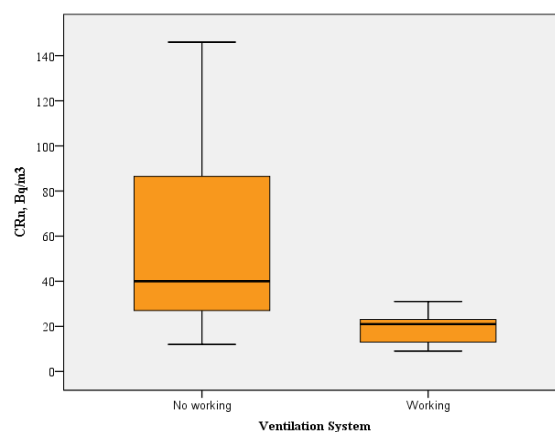
Fig.4. Distribution of the indoor radon depending on the efficient of the ventilation system in Ovcha Mogila

Increasing ventilation rate increases air change rate which decreases radon level. Direct supply of radon rich thermal water to the treatment area and non-efficient ventilation

system have an impact on the radon accumulation in the air of premises. Our results find ventilation play the major role in the cumulating of radon in indoor air of spas.

DOSE ASSESSMENT

To estimate the dose in the lungs that visitors can receive in rooms we used a model of lung deposition of radon progeny and dosimetry. The effective dose of a visitor who performed procedures with thermal water in different spas was evaluated according to ICRP 137 [16]. A reference value dose coefficient of 3 mSv per mJ.h.m^3 corresponds to 6.7×10^6 mSv per Bq.h.m^3 assuming an equilibrium factor, F, of 0.4 were used [16]. Normally each visitor uses the mineral water in the pools and treatment rooms from one to four hours a day. The average radon concentration was analysed from the spectra of direct measurements during the visit. The results of the analysis are presented in Table 2. The values obtained vary from 10.3 to 0.1 μSv per hour. In most of the surveyed branches (9 numbers) the values remain low and are comparable to the values reported for some spas [17, 18, 22].

Table 2. Effective dose for visitors per hour in rooms using water

Spa	AM CRn	EfD	Humidity
	Bq.m^3	μSv	%
Momin Prohod	3852	10.3	152
Narechenski Bani	965	5.0	56
Hisarya	118	0.6	59
Pavel Banja	58	0.3	53
Varshets	61	0.3	45
Bankya	89	0.5	29
Kystendil	126	0.7	76
Sandanski	30	0.2	54
Velingrad	59	0.3	50
Ovcha Mogila	22	0.1	67
Banite	32	0.2	59

The potentially increase of air radon concentration is higher in places with water therapy, such as swimming pools, bathtubs, tangents etc. where there is a high level of steam, and humidity due to the use of more water [19]. The highest humidity is recorded in Momin Prohod, where the radon concentration is the highest and there is no ventilation system (Table 2). The technique of bath filling influenced the contribution of radon in the pool and bath areas of the spa. Other studies have found largest increase in internal radon when the bath is filled with water taps [19, 20, 21]. In our case the measurements indicate higher values during the use of geothermal water for treatment. A more accurate the radon exposure impact assessment of the environment could be done by conducting simultaneously targeted studies in both environments wet (such as spa) and dusty (such as mining).

CONCLUSION

Measurements of ^{222}Rn concentrations in indoor air of spas buildings in Bulgaria were carried out using continuous measuring instruments. The radon concentration varied in the range of 16 - 4455 Bq.m^3.

The visitors' effective lung dose is low (except Momin Prohod and Narechenski Bani) and is comparable with the values reported for other spa studies. The radiation dose varied depending on factors such as type of premises (with geothermal water and without), presence of a ventilation system, ventilation rate and time spent in the treatment premises.

The difference in the concentration of radon in premises with water therapy and others without water has been confirmed, which proves that geothermal water is an additional source of radon in the spa. We have also observed that mineral water as a source of radon increases the concentration of gas in the rooms where water therapy is performed.

The limited number of spas (Momin Prohod and Narechenski Bani) have radon levels in air above the national reference level. For the Narechenski Bani branch, measures must be taken to improve ventilation, while in Momin Prohod a mechanical ventilation system must be built to better protect human health.

The results of the direct radon measurements and spectrum analysis showed that working ventilation system have significant impacts on radon content in a larger number of treatment premises. One of the possible solutions for improving indoor air quality is the well-functioning ventilation system. The effective dose for visitors in different branches varied depending on factors such as the effective ventilation system, and the using of thermal water for therapy. The results of the study could be useful to optimize radon concentration in building with public access as spa centers.

ETHICAL APPROVAL

The authors declare that this manuscript is original, has not been published before and is not currently being considered for publication elsewhere. The results are measured and analysed by authors.

DECLARATION OF INTERESTS

The authors declare that they have no known competing financial interests or personal relationships that could have appeared to influence the work reported in this paper.

ACKNOWLEDGEMENTS

ABREVIATIONS

222Rn – radon;
226Ra – radium;
CRn – radon concentration, Bq.m-³;
GM – geometric mean;
AM – arithmetic mean;
Min – minimum;
Max – maximum;
CV – coefficient variation;
EfD – effective dose;
MW – Mann-Whitney test;
KS – Kolmogorov-Smirnov test.

REFERENCES

1. V. Hristov, N. Stoyanov, S. Valtchev, S. Kolev, A. Benderev. IOP *Conf. Series: Earth and Environmental Science,* **249**, 012035 (2019).
2. V. Hristov, M. Trayanova, S. Kolev. *National Proc. of Conference of Bulgarian Geological Society with international participation* "GEOSCIENCES 2016" (2016).
3. A. Benderev, V. Hristov, K. Bojadgieva, B. Mihaylova, In: Papić, P. (Ed.). Mineral and Thermal Waters of Southeastern Europe. *Switzerland, Springer International Publishing,* 47, (2016).
4. M. Pugliese, M. Quarto, V. Roca, *Indoor and Built Environment,* **23,** 1 (2013).
5. UNSCEAR. Report 2006, Volume II, Annex E, *UN ed., NY*, (ww.unscear.org/unscear/en/publications.html), (2009).
6. WHO. H. Zeeb, F. Shannoun, Eds. *World Health Organization*, (2009).
7. G. Manic, S. Petrovic, M. Vesna, D. Popovic, D. Todorovic, *Environm. Inter.* **32,** 533 (2006).
8. J. Somlai, A. Torma, P. Dombovári, N. Kávási, K. Nagy, T. Kovács, *J Radioanal Nucl Chem*, **272,** 101 (2007).
9. D. Nikolopoulos, E. Vogiannis, E. Petraki, A. Zisos, A. Louizi, *Sci. Tot. Environ,* **408**, 495 (2010).
10. A.S. Silva, M.L. Dinis, Proc. of RAD Conference 2017, *5th int. conf. on radiation and application in various field of research, Budva*, **2**, 141, (2017).
11. European Commission, Council Directive 2013/59/EURATOM laying down basic safety standards for protection against the dangers arising from exposure to ionizing radiation, and repealing, *OJ of EU, L 13/*1. (2013),
12. Regulation on Radiation Protection, adopted by CM Decree № 20/14.02.2018, amended by CM No.455/22.12.2020.
13. E. Vogiannis, D. Nikolopoulos, *Sci. Total Environ,* **405**, 36 (2008).
14. M. Inagaki, T. Koga, H. Morishima, Sh. Kimura, M. Ohta, *J. Journal of Nuclear Science and Technology*, **49,** 531 (2012).
15. M. Adelikhah, A. Shahrokhi, S. Chalupnik, E. Toth-Bodrogi, T. Kovcacs, *Iran. Heliyon,* **6** e04297 (2020).
16. ICRP. Occupational Intakes of Radionuclides: Part 3, *Ann. ICRP 2017*, **46**, (2017).
17. V. Radolic, B. Vukovic, G. Smit, D. Stanic, *J. Environ. Radioact,* **83,** 191 (2005).
18. D. Nikolopoulos, E. Vogiannis, *Sci. Tot. Environ,* **373,** 82 (2007).
19. M. Müllerová, J. Mazur, P. Blahušiak, D. Grzadziel, K. Holý, T. Kovács, K. Kozak, E. Nagy, M. Neznal, M. Neznal, A. Shahrokhi, *Nukleonika,* **61,** 303 (2016).
20. E. Vogiannis, M. Niaounakis, C. P. Halvadakis, *Environ Int,* **30,** 621 (2004).
21. H. Lettner, A. K. Hubmer, R. Rolle F. Steinhäusler, *Environment International,* **22,** 399 (1996).
22. K. Walczak, J. Olszewski, M. Zmyslony, *J. of Occup. Medicine and Environmental Health,* **29,** 161 (2016).

Comparative study of the extracting polysaccharides from Traditional Chinese Medicine *Astragali Radix* in the field of new biological cellulase-assisted enzymes technology

Y. Sun[1], L. Miao[1*], F. Yang, W. Sun, Z. Peng, Y. Li[*]

Shanxi Medical University, School of Pharmacy, 98 Daxue Str, 030600 JinZhong, P. R. China

Traditional Chinese Medicine *Astragali Radix* (AR) that is included in the edible herbal list made by the Ministry of Health of China possesses multiple immunomodulatory effects. This study had shown that *Astragalus* polysaccharide (APS) among ingredients that play the significant role in immune regulation is the most active one. Biological enzymes, as innovative biological technology in the field of new energy, such as cellulase-assisted enzyme, were used in preparing the APS from *Astragali Radix* in this study. The conventional water reflux extraction was employed as the control group. Using the content of total polysaccharides as the evaluation index, anthrone-sulfuric acid method was applied to determine polysaccharide content. With ratio of raw material to water 1:30 g/mL，the polysaccharide content of the traditional process could be up to 4.82% when time was 120 min and temperature was 90°C. Cellulase-assisted enzymatic extraction conditions of polysaccharide was optimized by single factor experiments. The optimal extraction conditions were as follows: dosage of cellulase, enzymolysis temperature 55°C, and pH 5.0. Under the optimal extraction conditions, the content of polysaccharide was 1.56%. Although, the content of cellulase-assisted method used to extract polysaccharide was a litter lower，but the macromolecules in AR were extracted quickly and transformed into small molecules with molecular weight less than 10 kDa on the basis of simulating the temperature and enzyme-like environment, with which cellulase enzymes are more easily to break down plant cell walls and could be absorbed effectively by the digestive tract in the human body. Therefor it provides theoretical reference for further development APSs.

Keywords: *Astragalus* polysaccharides, cellulase-assisted enzymes extraction, water reflux extraction, comparative study

INTRODUCTION

Astragali Radix (AR), also well-known as Huangqi in China, it is derived from the dried root of perennial legume *Astragalus* membranaceus (Fisch.) Bge. var. mongholicus (Bge.) Hsiao and A. membranaceus (Fisch.) Bge. [1]. AR is one of the essential and commonly used Traditional Chinese Medicine (CHM) to tonify Qi，its medicinal history has been recorded for more than 2000 years. Moreover, AR has been included in the list of national drug and food homology in 2018. To date, over 30 polysaccharides had been found in AR. Most of them are heteropolysaccharides. The bioactivities of polysaccharides are related to their structures, glycosidic bonds, monosaccharide compositions, ratio of monosaccharides, molecular weights, and so on. The immunoregulatory effects of *Astragalus* polysaccharide (APS) were mainly related to their structures α-(1 → 4)-D-glucan. Generally, the molecular weights of the heteropolysaccharides are in the range of 8.7 kDa to 4.8×10^3 kDa，the molecular weights range with good water solubility were from 10 to 1.0×10^3 kDa.

The activities were the strongest when the molecular weights were between 10 kDa and 50 kDa [2-3]. Studies have shown that APS has significant immunomodulatory effects on antitumor and antiinfection [4]. APS-Ⅱ are the most immune active parts of *Astragalus* polysaccharides (APSs), and their molecular weights are about 10 kDa. In the monosaccharide compositions of the immune active APSs, Glu is the most abundant, then followed by Ara and Gal. The molecular weights of APSs for injection are mainly concentrated in 10 kDa approximately, indicating that the molecular weights of 10 kDa were the main parts of their efficacy [5]. It was preliminarily speculated that AHPS (*Astragalus* heteropolysaccharides, about 11 kDa) was mainly transported and absorbed by small intestinal cells by everted gut sac method in rats. Preparation processing, especially the methods for herbal extraction, would bring different pharmacological effect. Currently, the most common polysaccharide extraction method is hot-water extraction and alcohol sedimentation. In recent years, various innovative green extraction techniques, such as ultrasonic assisted extraction, semi-bionic extraction [6-7] and enzyme assisted extraction are in practice for isolation of bioactive polysaccharides. Enzyme assisted extraction technology offers many advantages, such as higher

* To whom all correspondence should be sent:
liyunlanrr@163.com. mllmll@126.com

extraction yield, lower energy requirements and suitable for the organism to absorb owing to the imitative biological environment, compared to conventional extraction methods. The effects of biological enzymatic extraction of polysaccharides are also superior to the other methods in terms of biological activities such as antioxidant and anticancer effects. It may enhance the activities of polysaccharides by keeping their relative molecular weights at a suitable low level [8-10].

The conventional water reflux extraction was employed as the control group. Anthrone-sulfuric acid method was applied to determine the content of total polysaccharides (in terms of Glu) [11]. This research aims to describe a comparative study of the extracting polysaccharides from AR between the new biological cellulase-assisted enzymes technology and conventional extraction method. With total polysaccharides content as index, single factor experiments were employed to optimize parameters of the influencing factors such as the enzyme amount, enzyme treated temperature and the range of pH value.

EXPERIMENTS

Plant materials, reagents

AR slices (5 years, wild or imitation wild) were purchased from Datong of Shanxi and certified by professor Y. Bai from Shanxi Medical University as *Astragalus* membranaceus (Fisch) Bge. Var. momgholicus (Bge). Hsiao. Cellulase (activity of 30 units/mg, food grade) was acquired from Zhejiang Yinuo Biotechnology Co., Ltd (Zhejiang, China). D (+)-glucose (080M00143V, >98%) was obtained from Shanghai Yuanye Biotechnology Co., Ltd (Shanghai, China). All the other reagents used were of analytical grade.

Apparatus

A pulverizer (Model LG-200, Ruian Baixin Medicine Machine and Instrument Factory, China) was used to pulverize AR slices. An ultrasonic apparatus (Model KQ3200E, Kunshan Ultrasonic Instrument Co. Ltd, China) was used to degrease AR power. A water bath (Model HH-2, Shanghai Guohua Electric Appliance Co. Ltd, China) was applied to polysaccharides extraction. An electronic balance with 0.0001 g readability (Model TP-213, Beijing Danfu Instrument Co. Ltd., China) was used for weighing AR degreased power. An oven (Model DHG-9035A, Shanghai Qixin Scientific Instrument Co., Ltd, China) was used to dry

polysaccharides from AR. A low-speed centrifuge (Model 800, Shanghai Surgical Instrument Factory, China) was used for separating polysaccharides. An ultraviolet-visible spectrophotometer (Model 1200, Shanghai Meipuda Instrument Co. Ltd, China) was used for quantifying AR polysaccharides.

Pre-treatment of AR slices

The slices were pulverized and passed through a 50-mesh sieve. Then, 100 g powder was ultrasoniced by 500 mL of 60~90% petroleum ether at normal temperature (about 25°C) for 40 min and filtration. The filtrate was discarded, the solvent in the filter residue evaporates to obtain AR degreased powder.

Extraction of APS with cellulase

AR degreased powder (5.0 g) was placed into a flask and added with distilled water obtain a material-to-water ratio of 1:30 (g/mL). The mixture was heated in a water bath for 120 min at designated dosage of enzyme, pH and temperature. After enzymolysis process, the extract was rapidly heated for 10 min in boiling water bath, cooled, filtered. The filtrate was concentrated and precipitated in three times the volumes of 95% ethanol, then let it stand for about 15 h. The polysaccharide precipitate was collected by centrifugation at 3000 r/min for 25 min, washed with anhydrous ethanol. The precipitate was dried in an oven at 60°C to get the crude enzymatic extraction polysaccharide (APS-E).

Optimization of cellulase-assisted enzymatic extraction conditions

A single factor experimental design was used to determine optimal extraction conditions including dosage of cellulase (ranging from 0.5 to 2.0%), pH value (ranging from 4.0 to 7.0, pH was adjusted to the desired value with 1 mol/L HCl and 1 mol/L NaOH), and temperature (ranging from 35 to 65°C) [12-14]. One factor was changed, while other factors kept constant in each experiment. The contents of total polysaccharides as the evaluation index, the optimal extraction conditions were determined.

Extraction of APS with water reflux as the control group

The water reflux extraction was carried out using the same material-to-water ratio 1:30 (g/mL) and the same time of extraction (120 min). AR degreased powder (5.0 g) was added into a flask

with 150 mL of water，the mixture was refluxed for 120 min at 90°C, and then filtered. The filtrate was concentrated and then submitted to the same steps that were taken in the cellulase extraction to get the crude water extraction polysaccharide (APS-W) *as the control group*.

Content determination for total polysaccharides with UV-vis spectrophotometry

Total polysaccharides were quantitatively analyzed by anthrone-sulfuric acid method using glucose as the standard monosaccharide.

1. Drawing of glucose standard curves

12.5 mg of glucose standard monosaccharide was weighed precisely, transferred quantitatively into a 50 mL volumetric flask after dissolution with distilled water to prepare the corresponding standard store solution (250 μg/mL), then stored in a refrigerator at 4°C. When in use, the solutions with mass concentration of 12.5, 15,17.5, 20, 22.5, and 25 μg/mL glucose standard solution were prepared, and the mixed liquor was shaken well, then 5.0 mL of 0.2% anthrone-sulfuric acid solution (100 mL of 80% concentrated sulphuric acid was added to 0.2 g of anthrone, it was prepared when it was needed) was added, respectively. After the mixed liquor was heated for 5 min in a boiling water bath，it cooled down at room temperature．The absorbance values (OD) of these solutions were measured by UV-vis spectrophotometer at the maximum absorption wavelength for making standard curves with corresponding gradient concentration.

2. Methodological verification of the precision

In order to verify the precision of the method, the OD values of the glucose standard solution (15 μg/mL) were measured six times under the maximum absorption wavelength, and the relative standard deviation (RSD) (%) value of these six measured OD were calculated.

3. Methodological verification of the stability and the repeatability

In order to verify the stability of the method, the test sample solution (APS-E, 18 μg/mL) was determined every 10 min and lasted for 50 min under the maximum absorption wavelength, and their OD values were used to calculate the RSD (%) as the stability. Furthermore, the RSD (%) of the other six portions same concentration solution were also tested for the repeatability of the method.

4. Methodological verification of the accuracy

The accuracy of the method was appraised by recovery experiments. The nine samples (APS-E, 18 μg/mL, 1 mL) of known concentrations were divided into three groups, and then each group was added with different amounts of glucose standard (7.5, 15, 23 μg), respectively. Nine portions solutions were diluted with distilled water and the OD values were measured under the maximum absorption wavelength, to calculate the recovery rate according to Eq. (1):

The recovery rate (%) = (the measured quantity after added standard substance – the known quantity of sample) × 100% / the mass of added standard substance $\qquad$ (1)

5. Content determination for total polysaccharides from AR

Polysaccharides of APS-E and APS-W were formulated into a test solution of 18 μg/mL with distilled water, respectively. The OD values of samples were determined at the wavelength of 612 nm to calculate total polysaccharides content (%) according to standard curve. The content was calculated as shown in the Eq. (2):

$$\text{polysaccharide concent (\%)} = (C \times D) \,/\, W \times 100\% \qquad (2)$$

where:

C - glucose concentration in the sample, μg/mL;
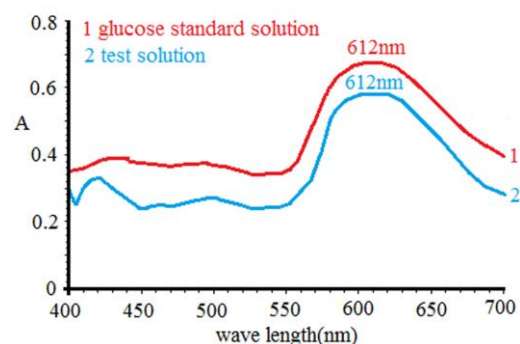
D - the dilution volume, mL;

W - mass of AR, μg.

Fig.1. Results of wavelength scanning for glucose standard solution and test solution

RESULTS AND DISCUSSIONS

The content determination for total polysaccharides

1. Drawing of glucose standard curves

The content of total polysaccharides was determined by UV-vis methods. UV wavelength scanning for standard solution and test solution

were showed in Fig.1. With wavelength scanning from 400 to 700 nm, the maximum absorption of standard sample and test sample at 612 nm. Using UV method, the linear regression equation of glucose was equal to $Y = 0.0289 X - 0.0068$ (Y was OD value, X was glucose concentration), of which $r = 0.9995$, range of linearity was 12.5~25 µg/mL.

2. Results of methodological verification

According to the results of UV method evaluation, the RSD (%) of the precision, stability and repeatability of the experiments is 0.2%, 1.9% and 1.0%, respectively. They were all with in 2%. The results of recovery rate were shown in Tab.1.

Table 1. The results of recovery rates

Mass of sample	Mass of glucose	Measured amount	Recovery rate	Average recovery rate	RSD
µg	µg	µg	%	%	%
15.5	7.8	23.2	98.7		
15.5	7.7	23.3	101.3		
15.5	7.8	23.2	98.7		
15.5	15.5	30.7	98.1		
15.5	15.5	30.7	98.1	99.2	1.3
15.5	15.5	30.6	97.4		
15.5	23.2	38.8	100.4		
15.5	23.1	38.7	100.4		
15.5	23.2	38.7	100.0		

From recovery rates data, the recovery rates of glucose were within the limits (95.0~105.0%). All of these methodological verification could met the requirements of quantitative analysis.
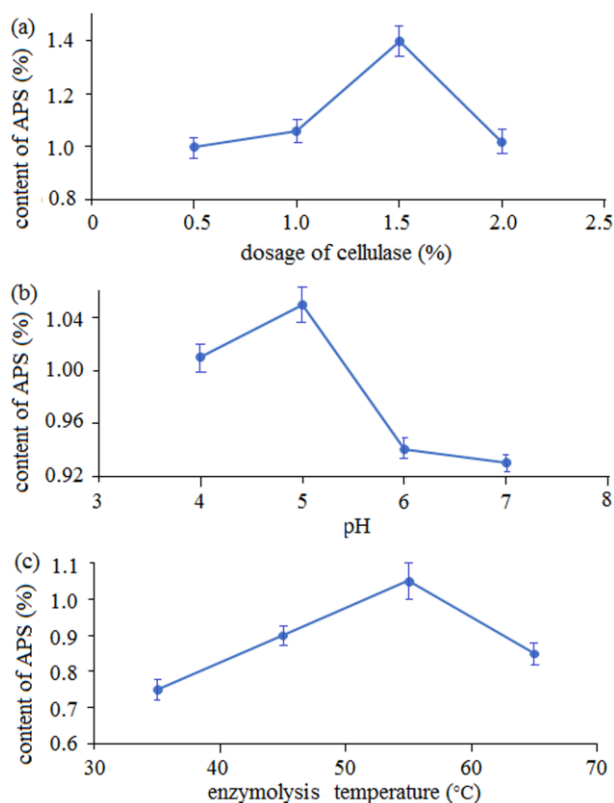
Single factor experiments analysis

The optimal conditions for enzymatic hydrolysis of factors were obtained by single factor test in the preliminary experiments.

1. Effect of dosage of cellulase on content of polysaccharides

In order to study the effect of different dosage of cellulase on the content of APS, the extraction was performed at different dosage of cellulase (0.5%, 1.0%, 1.5% and 2.0%), keeping the pH value, raw material to water ratio, temperatures and time constant at pH 5.0，1:30 g/mL, 120 min, and 55°C, respectively. As shown in the Fig.2a, with the increasing dosage of cellulase, the content of polysaccharides growed to top and decreased afterward. Generally, high dosage of cellulase promotes the diffusion of polysaccharides from the cells. When the amount of enzyme reaches a certain

value, such as 1.5%, the reaction with the substrate will reach a saturated state, and if excessive enzyme is added at this time, the dissolution of polysaccharides will be blocked. Therefore, 1.5% was chosen as the optimum dosage of cellulase.

Fig.2. Results of single factors experiments (a) dosage of cellulase (b) pH value (c) enzymolysis temperature

2. Effect of pH value on content of polysaccharides

As shown in Fig.2b, the effect of pH value on content of polysaccharides was investigated. The pH value was changed from 4.0 to 7.0, while the other extraction conditions were: dosage of cellulase 1.5%, raw material to water ratio 1:30 g/mL, time 120 min, and temperature 55°C. The content increased with pH until it was up to 5.0 and then began to decrease. So, 5.0 was chosen as the optimum pH value.

3. Effect of temperature on content of polysaccharides

Extraction was performed at different temperatures (35, 45, 55, and 65°C). The dosage of cellulase was 1.5%, the raw material to water ratio was 1:30 g/mL, the time was 120 min and the pH was 5.0. Generally, high temperature promotes the diffusion of polysaccharides from the cells, which

indicates that lower temperature might prevent the degradation of polysaccharide and assure its bioactivities. As shown in the Fig.2c, at first the content increased, and when 55°C, it subsequently decreased with increasing temperature. Hence, 55°C was deemed as the optimal temperature.

According to the single factor experiments, the extraction conditions were optimized as follows: dosage of cellulase, 1.5%; temperature, 55°C and pH value, 5.0.

The content determination for total polysaccharides of AR

The total polysaccharides content of AR samples obtained with cellulase-assisted treatment under the optimized extraction conditions (dosage of cellulase, 1.5%; temperature, 55°C and pH value, 5.0) and in control group were 4.82% (n=3) and 1.56% (n=3), respectively. This results suggest that although, the content of cellulase-assisted method used to extract polysaccharide was a litter lower by far，but the macromolecules in AR were extracted quickly and transformed into small molecules with molecular weight less than 10 kDa on the basis of simulating the temperature and enzyme-like environment, with which cellulase enzymes are more easily to break down plant cell walls and could be absorbed effectively by the digestive tract in the human body. Therefor it provides theoretical reference for further development APSs.

CONCLUSIONS

The macromolecules in AR were extracted quickly and transformed into small molecules, because cellulose-assisted method extracted polysaccharides reduce the molecular weight of polysaccharides, break the long-chain structure of the original polysaccharides, thus releasing more active units, and do not destroy the polymerization structure of the active units, so that the relative molecular weight of the polysaccharide is kept at a suitable low level, for example, less than 10 kDa, on the basis of simulating the temperature and enzyme-like environment, which could be absorbed effectively by the digestive tract in the human body [15]. So, the cellulase-assisted method provides reference value for the extraction of bioactive polysaccharides by multiple enzyme extraction or the combination on other extraction technology with enzyme extraction technology, also provides theoretical basis for later pharmacological and pharmacokinetic studies.

ACKNOWLEDGEMENTS

ABBREVIATIONS

AR- Astragali Radix;
CHM - Chinese Medicine;
APS -Astragalus polysaccharide;
AHPS-Astragalus heteropolysaccharides;
APS-E- enzymatic extraction polysaccharide;
APS-W- water extraction polysaccharide;
UV-vis- ultra violet-visible;
OD -absorbance values;
RSD- relative standard deviation;
Da - dalton;
Glu - glucose;
Ara - arabinose;
Gal - galactose.

REFERENCES

1. China Pharmacopoeia Committee. Pharmacopoeia of the People's Republic of China. China Chemical Industry Press, Beijing, 2020.
2. Z. Chen, L. Liu, C. Gao, W. Chen, C. Wong, P. Yao, Y. Yang, X. Li, X. Tang, S. Wang, Y. Wang. Astragali Radix (Huangqi): A promising edible immunomodulatory herbal medicine. *Journal of Ethnopharmacology* **258**, 112895-112912 (2020).
3. Z. Guo, Y. Lou, M. Kong, Q. Luo, Z. Liu, J. Wu. A Systematic Review of phytochemistry, pharmacology and pharmacokinetics on Astragali Radix: implications for Astragali Radix as a personalized medicine. *International Journal of Molecular Sciences* **20**, 1463-1506 (2019).
4. K. Li, Y. Cao, S. Jiao , G. Du, Y. Du, X. Qin. Structural characterization and immune activity screening of polysaccharides with different molecular weights from Astragali Radix.

Frontiers in Pharmacology **11**, 582091-582108 (2020).

5. Y. Cao, K. Li, X. Qin, S. Jiao, Y. Du, S. Li, X. Li. Quality evaluation of different areas of Astragali Radix based on carbohydrate specific chromatograms and immune cell activities. *Acta Pharmaceutic Sinica* **54**, 1277-1287 (2019).

6. Y. Li, C. Zhu, X. Zhai, Y. Zhang, Z. Duan, J. Sun. Study on the kinetic model, thermodynamic and physicochemical properties of Glycyrrhiza polysaccharide by ultrasonic assisted extraction. *Chinese Herbal Medicines* **10**, 416-423 (2018).

7. R. Wang, G. Wu, L. Du, J. Shao, F. Liu, Z. Yang, D. Liu, Y. Wei. Semi-bionic extraction of compound turmeric protects against dextran sulfate sodium-induced acute enteritis in rats. *J. of Ethnopharmacology* **190**, 288-300 (2016).

8. K.L. Nagendra chari, D. Manasa, P. Srinivas, H.B. Sowbhagya. Enzyme-assisted extraction of bioactive compounds from ginger (Zingiber officinale Roscoe). *Food Chemistry* **139**, 509-514 (2013).

9. Y. Dong, H. Lin, S. Miao, X. Lu. Advances in enzymatic extraction of polysaccharides. *Science and Technology of Food Industry* **42**, 351-358 (2021).

10. H. Chen, X. Zhou, J. Zhang. Optimization of enzyme assisted extraction of polysaccharides from Astragalus membranaceus. *Carbohydrate Polymers* **111**, 567-575 (2014).

11. D. Chu，Z. Huang，F. He. Comparison between sulfuric acid-phenol and sulfuric acid-anthrone methods used for determination of polysaccharides in shoots of Aralia elata (Miq．) Seem. *Agricultural Biotechnology* **7**, 170-173 (2018).

12. Y. Li, C. Zhu, X. Zhai, Y. Zhang, Z. Duan, J. Sun. Optimization of enzyme assisted extraction of polysaccharides from pomegranate peel by response surface methodology and their anti-oxidant potential. *Chinese Herbal Medicines* **10**, 416-423 (2018).

13. M. Dong, Y. Jiang, C. Wang, Q. Yang, Xi. Jiang, C. Zhu. Determination of the extraction, physicochemical characterization, and digestibility of sulfated polysaccharides in seaweed—porphyra haitanensis. *Marine Drugs* **18**, 539-559 (2020).

14. Y. Wang, Y. Jing, F. Leng, S. Wang, F. Wang, Y. Zhuang, X. Liu, X. Wang, X. Ma. Establishment and application of a method for rapid determination of total sugar content based on colorimetric microplate. *Sugar Tech* **19**, 424-431 (2017).

15. DING H., Kaize H.E., ZHANG L., Tian F.U. Extraction and Fractional Separation of Polysaccharide from *Astragalus membranaceus* on the Basis of Molecular Weight. *Chin J Appl Environ Biol.*,**16**（5）, 719~723 (2010).

Stronger antioxidant and hepatoprotective components generated from Rubiaceae *Hedyotis diffusa* with biotinidase in the field of new biological energy technology

Y. Sun, Y. Qi, M.J Zhang, Y.L. Li[*]

Shanxi Medical University, School of Pharmacy, 98 Daxue Str, 030600 JinZhong, P. R. China

Biological enzymes, as innovative biological technology in the field of new energy, were used in preparing the total flavonoids of Rubiaceae, *Hedyotis diffusa* in this study. The differences of the flavonoid compositions, contents, antioxidant and hepatoprotective activities on HL-02 cells damaged by H_2O_2 were compared between the new biotinidase energy and traditional technology. What's more, the antioxidant activity screening was investigated by H_2O_2-damaged HL-02 cells. The protection rates of total flavonoids and active components of *Hedyotis diffusa* on H_2O_2-damaged HL-02 cells were determined by MTT method, and the contents of ALT, AST, LDH, and ALP in cell culture medium were measured to investigate the liver protection of total flavonoids of *Hedyotis diffusa*. The results showed that the contents of isoflavones extracted by the new biological enzymatic energy technology were significantly higher than those by traditional reflux extraction, ultrasonic method and ultrasound-assisted enzymatic extraction method ($p<0.05$). The biological enzyme as new biological energy source could obtain new components with stronger antioxidant and hepatoprotective activities in *Hedyotis diffusa*, which was beneficial to the development and utilization of biological technology in the field of new energy.

Keywords: New biotinidase, total flavonoids, *Hedyotis diffusa*, biological energy source technology, antioxidant and hepatoprotective activties

INTRODUCTION

Hedyotis Diffusa is an annual herb, which attributed to the Rubiaceae and mainly distributed in the south of China and some Asian countries, such as Indonesia, Japan, Malaysia, Nepal, Thailand [1] and so on. Flavonoids are one kind of the main components of *Hedyotis diffusa* that exert various pharmacological activities including antioxidant, hepatoprotective and anti-tumor and so on [2-4]. The manufacture technologies of plant flavonoids are mainly divided into traditional preparation technology and modern extraction technology based on the energy pattern used for industrial applicability and environmental protection [5].

In this research, biological enzymes were used in preparing the total flavonoids of Rubiaceae, *Hedyotis diffusa*. The principle of the enzymatic technology in field of biological new energy is using the special biological enzymes to better release and extract biologically active substances by destroying their cell walls. It could also break down impurities such as protein, starch and pectin, and improve the productive rate of target biological activity components. Enzymatic

production was used in combination with solvent extraction for the first time in this study. It has the advantages of low cost, high productive rate, strong specificity and reliability, simple operating equipment and environmental protection, which was suitable for industrial production by using new biological enzymes technology [6]. Compare the total flavonoids and active components of *Hedyotis diffusa* prepared by enzymatic energy with those prepared by the traditional productive technologies (reflux, ultrasonic method and ultrasound-assisted enzymatic extraction), there were differences in contents and pharmacological antioxidant and hepatoprotective activities remain to be further investigated.

Immediately following, 3-(4,5-dimethyl-2-thiazolyl)-2,5- diphenyl-2-H-tetrazolium bromide (MTT) was used to detect cell viability for screening active ingredients with antioxidant and liver-protecting activities [7]. This new biological enzymes energy technology would be instructive for future investigation on stronger antioxidant and hepatoprotective components generated from natural safe and non-toxic plant thereon which natural drugs would be established.

---

* To whom all correspondence should be sent:
 liyunlanrr@163.com

EXPERIMENTS

Materials and Reagents

Hedyotis diffusa was collected from Jiangxi and certified by Professor Tianai Gao from Shanxi Provincial Food and Drug Inspection Institute. Biological cellulase: 30 units/mg (Zhejiang Yinuo Biotechnology Co., Ltd., food grade). Macroporous adsorbent resin AB-8 was purchased from Chengdu Grecia Chemical Technology Co., Ltd. HL-02 cells, RPMI-1640 medium, fetal bovine serum, 0.25% trypsin were purchased from Wuhan Dr. Biotech Co., Ltd. Dimethyl sulfoxide (DMSO), hydrogen peroxide, penicillin and streptomycin, MTT were obtained from Beijing Solibao Technology Co., Ltd. Alanine aminotransferase (ALT), aspartate aminotransferase (AST), alkaline phosphatase (ALP) and lactate dehydrogenase (LDH) assay kits were purchased from Nanjing Jiancheng Biotechnology Research Institute. The experimental water was distilled water, and other reagents used were chromatographically grade.

Apparatus Total Flavonoids Preparetion

The total flavonoids of *Hedyotis diffusa* were extracted by biological enzymatic technology(A), reflux technology (B), ultrasonic technology (C) and ultrasound-assisted technology (D). Before extraction, *Hedyotis diffusa* were dried, grinded and sieved to get the solid powder (60 mesh). The solid powder would be ultrasonically treated with petroleum ether (1g:20mL) for 30minutes for degreasing, and dried and cooled. The extractions were as follow, all the processes were optimized. In enzymatic technology, 0.5% biological cellulase was added to per 1g of degreased sample and extracted at 55℃ for 1.5h in 30mL 50% ethanol solution with pH 5.0. The ultrasound-assisted method was performed in an ultrasonic cleaner according to the above process. Both reflux and ultrasonic processes used 50% ethanol as the extraction solvent, and the material-liquid ratio was 1:30. Then extracted for 1.5h under reflux at 80℃ or ultrasonic conditions, respectively. The four extracting technologies were purified by macroporous adsorption resin AB-8, and finally the total pure flavonoid extracts of *Hedyotis diffusa* were obtained.

Cell Culture

HL-02 cells were cultured in RPMI-1640 added with 10% heat-inactivated FBS, 100 U/mL penicillin and 100 μg/mL streptomycin in a constant temperature incubator with 5% CO_2 at 37℃. According to cell growth, subculture was carried out for 2 days to ensure that all cells used for the experiment were in a logarithmic growth phase. The normal control group cultured with RPMI-1640. The model group cultured with 200 μmol/L H_2O_2. The administration groups treated with 125, 62.5, 31.25 μg/mL total flavonoids prepared by different technologies and compounds including vitexin, isovitexin, naringin, genistein, apigenin and chrysin (16, 8, 4 μmol/L, respectively). Bifendate (12 μmol/L) was given as positive control group. The survival rates of HL-02 cells were determined by MTT method.

Screening for Liver Protective Activity

The model of H_2O_2-induced HL-02 injury was used to investigate the protective effects of total flavonoids on liver damage. H_2O_2 at different concentrations (50, 100, 200, 400, 600, 800 μmol/L) were applied to HL-02 cells for 4h. The absorbance (OD) value was measured by MTT method and the cell survival rates were calculated to determine the appropriate modelling concentration of H_2O_2. The administration groups and the positive control group were treated with the samples as in "3" for 12 h in advance. 125 μmol/L bifendate was used as a positive control. After treatment according to the above method, the OD was measured and the protection rates for HL-02 cells were caculated: Protection rate (%) = ($OD_{\text{administration group}}$-$OD_{\text{model group}}$) / ($OD_{\text{control group}}$-$OD_{\text{model group}}$)× 100%.

Optimization of cellulase-assisted enzymatic extraction conditionsDetermination of ALT, AST, LDH and ALP in Supernatant

The *in vitro* activities of hepatocellular leakage ALT, AST, LDH and ALP were assayed as markers and indices of hepatotoxicity of HL-O2 cells. HL-02 cells in logarithmic growth phase were digested with trypsin and seeded in 12-well plates, cultured for 24h. After collected, the contents of AST, ALT, LDH and ALP in the cell culture media were measured according to the instructions of the kits. The activities were expressed as the percentages of the activities over the corresponding control groups.

Data Analysis

T-test analysis was used to compare the differences between different groups. When $p <$ 0.05, there was a statistical difference. All experiments were repeated at least 3 times in parallel.

RESULTS AND DISCUSSIONS

Concentration Selection of H_2O_2 Modeling

The survival rates of H_2O_2 at concentrations (50~800μmol/L) on HL-02 cells were shown in Fig.1. The results showed that the survival rate of HL-02 cells decreased with the increase of H_2O_2 concentration. When the concentration of H_2O_2 was 200μmol/L, the cell survival rate was about 60%, which was significantly lower than that of the control group ($p < 0.05$). So, the concentration 200μmol/L of H_2O_2 was selected for hepatocyte damage modeling.
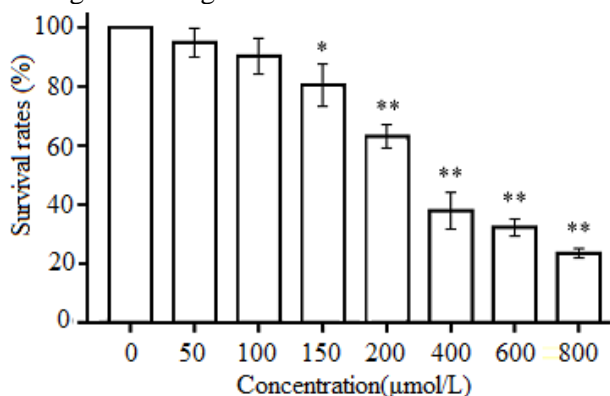
Fig.1. Cell survival rate of HL-02 cells by different concentrations of H_2O_2. * ($p<0.05$), ** ($p<0.01$) indicated that there was a significant difference from the model group; ## ($p<0.01$) indicatesd that there was a significant difference from the control group

Screening for Liver Protecive Activities

Furthermore, as shown in Fig.2, the highest protection rates of biological enzymatic technology (sample A) were obtained among four extraction technologies,respectively. It was up to 59.30 ± 0.81% and even more higher than the positive control bifendate at 125μg/mL. The hepatoprotective activity of total flavonoids prepared by enzymatic technology was also significantly higher than those of total flavonoids prepared by other method at the same concentration ($p<0.05$).

Determination of hepatotoxicity and antioxidant pattern

Once hepatocytes are damaged, ALT, AST, LDH and ALP will be released out of cells into the culture medium. So, they are frequently used as biomarkers of hepatotoxicity. When liver damage occurs, a large amount of those would be released and the contents were significantly increased.

Herein, the activities of ALT, AST, LDH and ALP in cellular supernatant were tested in order to further investigate the protective effects of total flavonoids of *Hedyotis diffusa* prepared by different methods on HL-02 cell injury induced by H_2O_2. They were significantly elevated in model groups compared with the control groups ($p< 0.01$) (shown in Fig.3-6).
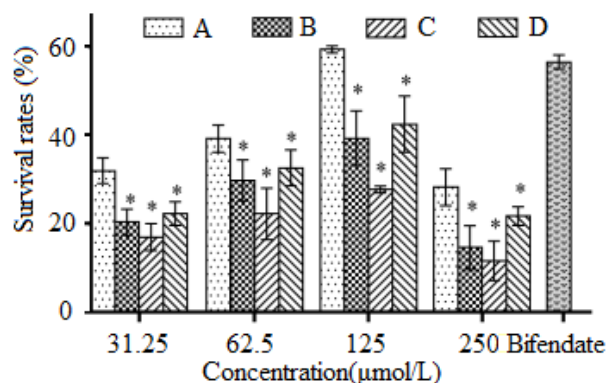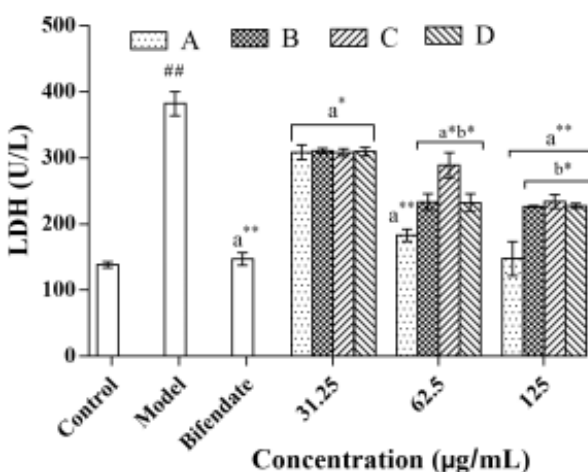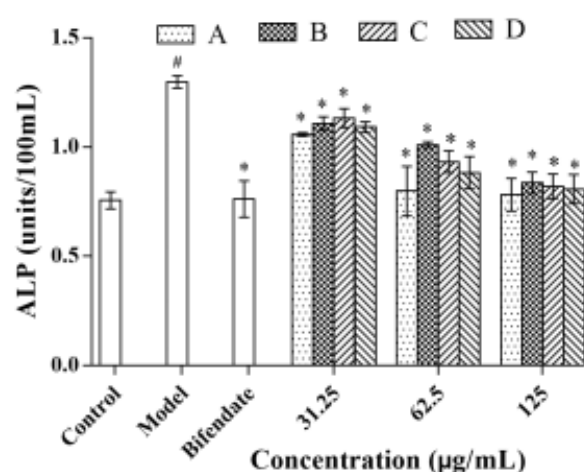

Fig.2. Protective activities of total flavonoids prepared by four different technologies. A, biological enzymatic technology; B, reflux technology; C, ultrasonic technology; D, ultrasound-assisted technology. * ($p<0.05$), ** ($p<0.01$) indicated that there was a significant difference from the model group; ## ($p<0.01$) indicatesd that there was a significant difference from the control group.
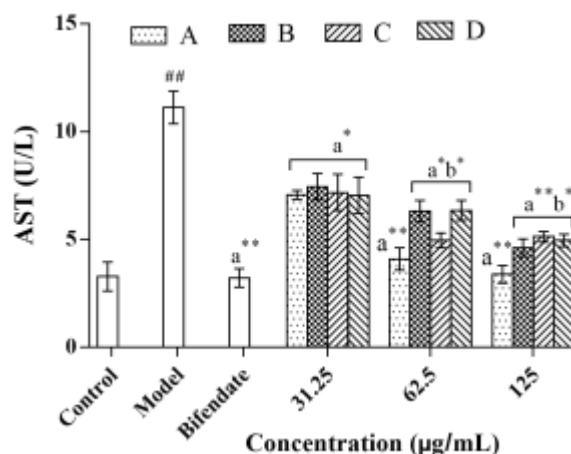
Fig.3. Detections of AST for hepatotoxicity and antioxidant pattern in H_2O_2-induced hepatotoxic HL-O2 cells for 24h. Bifendate (5mg/mL) was as positive control. A, biological enzymatic technology; B, reflux technology; C, ultrasonic technology; D, ultrasound-assisted technology. ##($p<0.01$) indicated there was a significant difference compared with control group; a* ($p<0.05$), a** ($p<0.01$) indicated that there was a significant difference compared with model group; b* ($p<0.05$) indicated there was a significant difference compared with sample A (biological enzymatic technology)
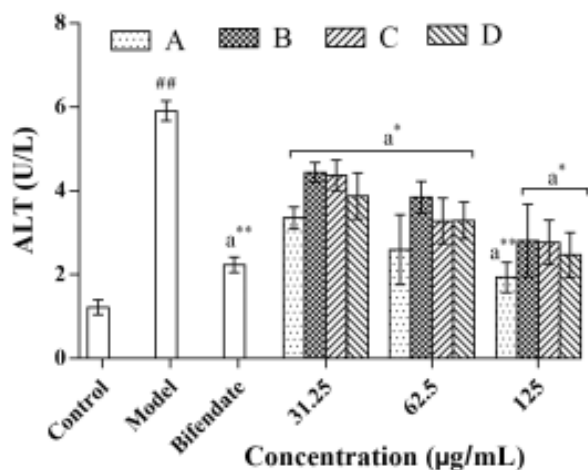
Fig.4. Detections of ALT for hepatotoxicity and antioxidant pattern in H_2O_2-induced hepatotoxic HL-O2 cells for 24h. Bifendate (5mg/mL) was as positive control. A, biological enzymatic technology; B, reflux technology; C, ultrasonic technology; D, ultrasound-assisted technology. $^{##}$($p<0.01$) indicated there was a significant difference compared with control group; a* ($p<0.05$), a** ($p<0.01$) indicated that there was a significant difference compared with model group; b* ($p<0.05$) indicated there was a significant difference compared with sample A (biological enzymatic technology)

Fig.5. Detections of LDH for hepatotoxicity and antioxidant pattern in H_2O_2-induced hepatotoxic HL-O2 cells for 24 h. Bifendate (5mg/mL) was as positive control. A, biological enzymatic technology; B, reflux technology; C, ultrasonic technology; D, ultrasound-assisted technology. $^{##}$($p<0.01$) indicated there was a significant difference compared with control group; a* ($p<0.05$), a** ($p<0.01$) indicated that there was a significant difference compared with model group; b* ($p<0.05$) indicated there was a significant difference compared with sample A (biological enzymatic technology)

Fig.6. Detections of ALP for hepatotoxicity and antioxidant pattern in H_2O_2-induced hepatotoxic HL-O2 cells for 24h. Bifendate (5mg/mL) was as positive control. A, biological enzymatic technology; B, reflux technology; C, ultrasonic technology; D, ultrasound-assisted technology. $^{##}$($p<0.01$) indicated there was a significant difference compared with control group; a* ($p<0.05$), a** ($p<0.01$) indicated that there was a significant difference compared with model group; b* ($p<0.05$) indicated there was a significant difference compared with sample A (biological enzymatic technology)

While, treatment of total flavonoids in cell supernatant at 31.25, 62.5, 125 µg/mL significantly reduced ALT, AST, LDH and ALP contents, which revealed a remarkable improvement in a dose-dependent manner compared with the model groups and positive control bifendate (125 µg/mL), as shown in Fig.3-6. At 62.5, 125 µg/mL, the effect of total flavonoids prepared by biological enzymatic technology (sample A) on reduce the content of AST and LDH were significantly higher than those of other three method at same concentrations ($p<0.05$).

CONCLUSIONS

Biological enzymes, as innovative biological technology in the field of new energy, had been widely used in various fields, including food raw material development, wastewater treatment and plant extraction applications. What's more, the effects of total flavonoids prepared by enzymatic method on reducing the contents of AST and LDH and protecting the H_2O_2-induced liver damage were significantly higher than those of other three method ($p<0.05$). In conclusion, the innovative biological enzymatic technology could improve the contents of active ingredients (about 3.5 times or more) with hepatoprotective effect. The total

flavonoids prepared by biological enzymatic technology had more effective on antioxidant and hepatoprotective activities. The biological enzymes as new biological energy source could obtain new components with stronger antioxidant and hepatoprotective activities in *Hedyotis diffusa*, which was beneficial to the development and utilization of biological technology in the field of new energy.

ACKNOWLEDGEMENTS

ABBREVIATIONS

MTT - 3-(4,5-dimethyl-2-thiazolyl)-2,5-diphenyl-2-H-tetrazolium bromide

ALT - alanine aminotransferase
AST - aspartate aminotransferase
LDH - lactate dehydrogenase
ALP – alkaline phosphatase
DMSO - Dimethyl sulfoxide
OD - absorbance

REFERENCES

1. Ye JH, Liu MH, Zhang XL. Chemical profiles and protective effect of hedyotis diffusa Willd in lipopolysaccharide-induced renal inflammation mice. International Journal of Molecular Sciences, 2015, 16(11):27252-27269.
2. Jiang YN. Research progress on active ingredients and pharmacological effects ofHedyotis diffusa. Renowned Doctor, 2019(03):235.
3. Wei YH. Research progress of Hedyotis diffusa. Shanxi Journal of Traditional Chinese Medicine, 2018, 34(12):53-56.
4. Hou SL. Research progress on the chemical constituents and pharmacological activity of TCM medicine. Chinese Journal of Clinical Research, 2018,10(06),140-141.
5. Wang LL, Bian XY, Gao WN, Li BL, Guo CJ.Advances in extration and purification techniques for flavonoids in plants. Acta Nutrimenta Sinica, 2019,41(06):606-610.
6. Song LX, Shao JJ. Research progress on extraction methods of flavonoids. Cereals&Oils, 2020, 33(01):21-22.
7. Gao X, Li C, Tang YL, Zhang, H. Effect of Hedyotis diffusa water extract on protecting human hepatocyte cells (L02) from H2O2-induced cytotoxicity. Pharmaceutical Biology, 2015:1-8.

BULGARIAN CHEMICAL COMMUNICATIONS

Instructions about Preparation of Manuscripts

General remarks: Manuscripts are submitted in English by e-mail or by mail (in duplicate). The text must be typed double-spaced, on A4 format paper using Times New Roman font size 12, normal character spacing. The manuscript should not exceed 15 pages (about 3500 words), including photographs, tables, drawings, formulae, etc. Authors are requested to use margins of 3 cm on all sides. For mail submission hard copies, made by a clearly legible duplication process, are requested. Manuscripts should be subdivided into labelled sections, e.g. **Introduction, Experimental, Results and Discussion**, *etc*.

The title page comprises headline, author's names and affiliations, abstract and key words.

Attention is drawn to the following:

a) **The title** of the manuscript should reflect concisely the purpose and findings of the work. Abbreviations, symbols, chemical formulas, references and footnotes should be avoided. If indispensable, abbreviations and formulas should be given in parentheses immediately after the respective full form.

b) **The author**'s first and middle name initials, and family name in full should be given, followed by the address (or addresses) of the contributing laboratory (laboratories). **The affiliation** of the author(s) should be listed in detail (no abbreviations!). The author to whom correspondence and/or inquiries should be sent should be indicated by asterisk (*).

The abstract should be self-explanatory and intelligible without any references to the text and containing not more than 250 words. It should be followed by key words (not more than six).

References should be numbered sequentially in the order, in which they are cited in the text. The numbers in the text should be enclosed in brackets [2], [5, 6], [9–12], etc., set on the text line. References, typed with double spacing, are to be listed in numerical order on a separate sheet. All references are to be given in Latin letters. The names of the authors are given without inversion. Titles of journals must be abbreviated according to Chemical Abstracts and given in italics, the volume is typed in bold, the initial page is given and the year in parentheses. Attention is drawn to the following conventions:

a) The names of all authors of a certain publications should be given. The use of "*et al.*" in the list of references is not acceptable.

b) Only the initials of the first and middle names should be given.

In the manuscripts, the reference to author(s) of cited works should be made without giving initials, e.g. "Bush and Smith [7] pioneered...". If the reference carries the names of three or more authors it should be quoted as "Bush *et al*. [7]", if Bush is the first author, or as "Bush and co-workers [7]", if Bush is the senior author.

Footnotes should be reduced to a minimum. Each footnote should be typed double-spaced at the bottom of the page, on which its subject is first mentioned.

Tables are numbered with Arabic numerals on the left-hand top. Each table should be referred to in the text. Column headings should be as short as possible but they must define units unambiguously. The units are to be separated from the preceding symbols by a comma or brackets.

Note: The following format should be used when figures, equations, *etc*. are referred to the text (followed by the respective numbers): Fig., Eqns., Table, Scheme.

Schemes and figures. Each manuscript (hard copy) should contain or be accompanied by the respective illustrative material as well as by the respective figure captions in a separate file (sheet). As far as presentation of units is concerned, SI units are to be used. However, some non-SI units are also acceptable, such as °C, ml, l, etc.

The author(s) name(s), the title of the manuscript, the number of drawings, photographs, diagrams, etc., should be written in black pencil on the back of the illustrative material (hard copies) in accordance with the list enclosed. Avoid using more than 6 (12 for reviews, respectively) figures in the manuscript. Since most of the illustrative materials are to be presented as 8-cm wide pictures, attention should be paid that all axis titles, numerals, legend(s) and texts are legible.

The authors are asked to submit **the final text** (after the manuscript has been accepted for publication) in electronic form either by e-mail or mail on a CD using a PC Word-processor. The main text, list of references, tables and figure captions should be saved in separate files (as *.rtf or *.doc) with clearly identifiable file names. It is essential that the name and version of the word-processing program and the format of the text files is clearly

indicated. It is recommended that the pictures are presented in *.tif, *.jpg, *.cdr or *.bmp format, the equations are written using "Equation Editor" and chemical reaction schemes are written using ISIS Draw or ChemDraw programme.

The authors are required to submit the final text with a list of three individuals and their e-mail addresses that can be considered by the Editors as potential reviewers. Please, note that the reviewers should be outside the authors' own institution or organization. The Editorial Board of the journal is not obliged to accept these proposals.

EXAMPLES FOR PRESENTATION OF REFERENCES

REFERENCES

1. D. S. Newsome, *Catal. Rev.–Sci. Eng.*, **21**, 275 (1980).
2. C.-H. Lin, C.-Y. Hsu, *J. Chem. Soc. Chem. Commun.*, 1479 (1992).
3. R. G. Parr, W. Yang, Density Functional Theory of Atoms and Molecules, Oxford Univ. Press, New York, 1989.
4. V. Ponec, G. C. Bond, Catalysis by Metals and Alloys (Stud. Surf. Sci. Catal., vol. 95), Elsevier, Amsterdam, 1995.
5. G. Kadinov, S. Todorova, A. Palazov, in: New Frontiers in Catalysis (Proc. 10th Int. Congr. Catal., Budapest, 1992), L. Guczi, F. Solymosi, P. Tetenyi (eds.), Akademiai Kiado, Budapest, 1993, Part C, p. 2817.
6. G. L. C. Maire, F. Garin, in: Catalysis. Science and Technology, J. R. Anderson, M. Boudart (eds), vol. 6, Springer-Verlag, Berlin, 1984, p. 161.
7. D. Pocknell, *GB Patent* 2 207 355 (1949).
8. G. Angelov, PhD Thesis, UCTM, Sofia, 2001.
9. JCPDS International Center for Diffraction Data, Power Diffraction File, Swarthmore, PA, 1991.
10. CA **127**, 184 762q (1998).
11. P. Hou, H. Wise, *J. Catal.*, in press.
12. M. Sinev, private communication.
13. http://www.chemweb.com/alchem/articles/1051611477211.html.

CONTENTS